IN-26

013322

NASA Contractor Report 202318

Experimental Characterization and Micromechanical Modeling of Woven Carbon/Copper Composites

Brett A. Bednarcyk, Christopher C. Pauly, and Marek-Jerzy Pindera
University of Virginia
Charlottesville, Virginia

January 1997

Prepared for
Lewis Research Center
Under Grant NAG3–1319

National Aeronautics and
Space Administration

Abstract

The results of an extensive experimental characterization and a preliminary analytical modeling effort for the elastoplastic mechanical behavior of 8-harness satin carbon/copper (C/Cu) composites are presented. Previous experimental and modeling investigations of woven composites are discussed, as is the evolution of, and motivation for, the continuing research on C/Cu composites. Experimental results of monotonic and cyclic tension, compression, and Iosipescu shear tests, and combined tension-compression tests, are presented. With regard to the test results, emphasis is placed on the effect of strain gauge size and placement, the effect of alloying the copper matrix to improve fiber-matrix bonding, yield surface characterization, and failure mechanisms. The analytical methodology used in this investigation consists of an extension of the three-dimensional generalized method of cells (GMC-3D) micromechanics model, developed by Aboudi (1994), to include inhomogeneity and plasticity effects on the subcell level. The extension of the model allows prediction of the elastoplastic mechanical response of woven composites, as represented by a true repeating unit cell for the woven composite. The model is used to examine the effects of refining the representative geometry of the composite, altering the composite overall fiber volume fraction, changing the size and placement of the strain gauge with respect to the composite's reinforcement weave, and including porosity within the infiltrated fiber yarns on the in-plane elastoplastic tensile, compressive, and shear response of 8-harness satin C/Cu. The model predictions are also compared with the appropriate monotonic experimental results.

Acknowledgments

This investigation was funded under the NASA Lewis Grant NAG3-1319 with Dr. Robert V. Miner as the technical monitor. The authors gratefully acknowledge this support and the assistance of Dr. David L. Ellis, Dr. Robert V. Miner, and Dr. Michael V. Nathal of NASA Lewis Research Center and Dr. Sandra M. DeVincent of Metal Matrix Castings, Inc. in carrying out the experimental portion of this investigation. The authors also thank Dr. Jacob Aboudi for fruitful discussions regarding the micromechanical modeling effort.

Table of Contents

1. Introduction

1.1 Woven Composites

Woven and braided composites, as a class of materials, are rapidly gaining popularity. The reinforcement phase of these composites consists of a woven or braided fabric formed by individual fibers, or by bundles of fibers, called yarns. One or more layers of the woven or braided fabric are used to reinforce traditional matrix materials. It is interesting to note that the concept of woven composites is not a new one. Ancient Egyptians used cotton fabrics impregnated with resin to protect fragile mummies. The effort to use woven composites for structural applications, though possibly less captivating, is considerably more recent.

By incorporating a woven reinforcement phase into a composite, rather than utilizing unidirectional fibers only, several benefits are realized. A single ply of a woven composite can have balanced thermomechanical properties in several directions. A single ply reinforced by a biaxial weave is similar to a [0/90] laminate, while a ply reinforced by a triaxial weave can mimic a [0/±60] laminate, as illustrated in Figure 1.1. In contrast, a unidirectional ply often has poor thermomechanical properties transverse to the fiber direction due to the lack of continuous reinforcement in this direction. The deficiency of a continuous ply in the transverse direction is often exacerbated by a weak fiber/matrix interface.

Woven and braided composites usually have superior out-of-plane properties with regard to impact and crack resistance relative to composites laminated with unidirectional plies. In fact, coated fabrics, which are in essence woven composites, are used to make bullet proof vests. Movement of the reinforcement weave can distribute the energy of an impact throughout many yarns, and, if a crack does form, there are fibers oriented in at least two directions to inhibit crack growth. Since the reinforcement phase has a tendency to remain intact independently from the matrix, woven composites are less prone to delamination and splitting along the fibers.

Finally, and perhaps most importantly, a woven or braided reinforcement phase offers superior stability during composite manufacturing compared to unidirectional fibers. A weave of fiber yarns is much simpler to handle than the thousands of individual fibers used in a graphite fiber reinforced composite, for example. The benefits of the weave's dimensional stability go further. Preforms with complex shapes can be woven or braided from the fiber yarns. These shapes can then be infiltrated with a metal or epoxy matrix to form a composite in the shape of the preform. This procedure is not feasible if individual unidirectional fibers are used. In addition, three-dimensional weaves and braids can be produced (see Figure 1.2). A third dimension of reinforcement can improve the properties of the composite even further.

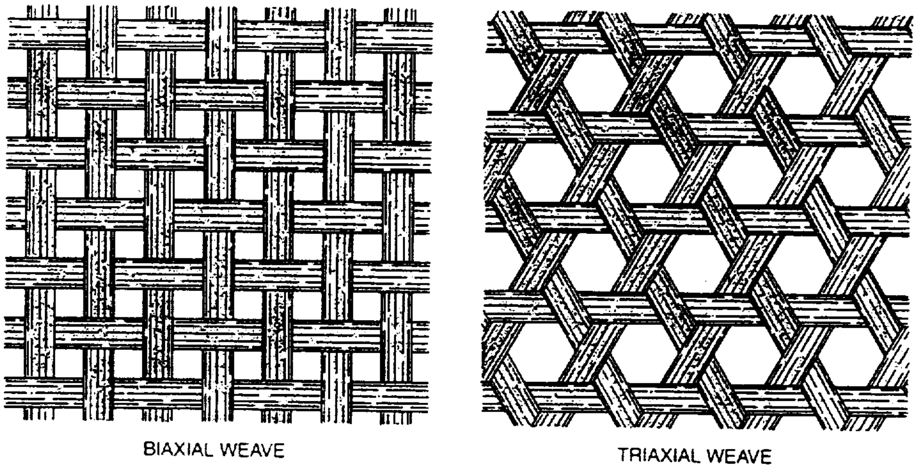

Figure 1.1. a) Biaxial weave pattern; b) Triaxial weave pattern (Chou, *et al.*, 1986).

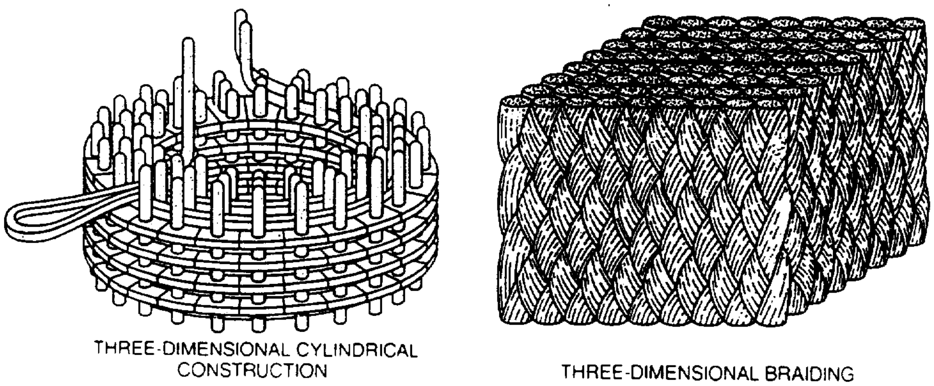

Figure 1.2. Examples of 3-D weave patterns. a) Cylindrical construction. b) 3-D braiding (Chou, *et al.*, 1986).

1.2 Modeling of Woven Composites

While woven composites offer advantages over unidirectional composites and laminates, they also present more of a challenge in terms of modeling. The woven reinforcement phase consists of yarns that undulate in and out of a plane. Thus the geometry of the composite is inherently three-dimensional. In addition, there are many different ways in which the reinforcement fabric can be woven (see Figure 1.3), and each of these weaves has a different repeating unit cell. These factors make modeling of woven composites challenging.

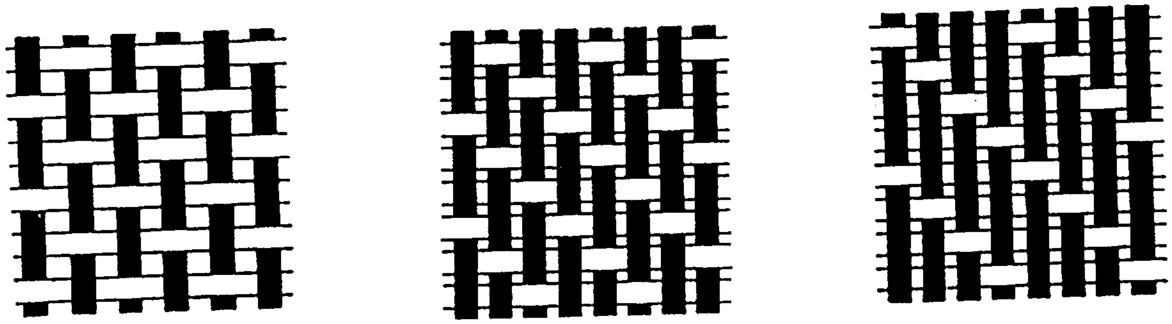

Plain Weave

2/1 Warp, Twill

3/1 Warp, Twill

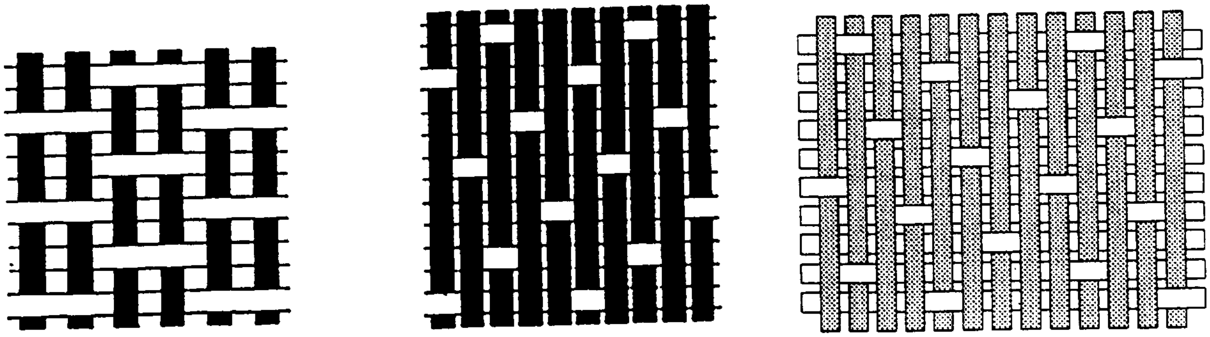

2/2 Cord

5-Harness Satin

8-Harness Satin

Figure 1.3. Examples of biaxial weaves (Miller, 1968).

1.2.1 Finite-Element and Boundary-Element Models

The complex three-dimensional geometry of woven composites makes finite-element modeling difficult. One can imagine constructing a three-dimensional mesh for finite-element implementation for each type of weave. Then if the geometry is changed slightly, for example if adjacent yarns are placed closer together, an entirely new mesh would be required. The effort required for such numerical modeling may be prohibitive. However, this type of effort was undertaken by Dasgupta and Bhandarkar (1994) and Dasgupta *et al.* (1996) to model a plain weave glass/epoxy with elastic phases. In this investigation, reasonable elastic constants were predicted for a realistic geometric representation of the composite, but only with great computational effort.

Whitcomb *et al.* (1992) proposed a finite-element model for woven composites in which spatial variations of material properties were accounted for within a single element. This approach can potentially decrease the number of elements required to accurately model the geometry of the weave. However, Whitcomb and Srirengan (1996) used a traditional three-dimensional finite-element analysis to model progressive failure in plain weave graphite/epoxy composites with varying degrees of fiber waviness. The finite-element approach was also used by Glaessgen *et al.* (1996) to examine the internal displacement and strain energy density fields in a plain weave glass/epoxy composite. Here, geometric complexities inherent to woven reinforcements (which greatly affect internal fields) are accounted for, but at a high computational cost. It should be noted that the above finite-element analyses considered only plain weave reinforced composites with elastic phases. Modeling of more complex weave patterns and including material nonlinearity would complicate these analyses considerably.

A boundary-element model developed by Goldberg and Hopkins (1995) that has been used to examine the elastic response of woven composites deserves reference. The boundary-element method requires less computational and mesh generating effort than the finite-element method, yet it can offer similar geometrical accuracy for woven composites. A version of this model with matrix plasticity is under development which may have potential for modeling woven metal matrix composites.

1.2.2 Approximate Analytical Models

Another route to modeling woven composites was taken by Chou and Ishikawa (1989). They have developed a series of models based on classical lamination theory for predicting the thermoelastic response of certain types of woven composites. The mosaic model treats the weave as an assemblage of cross-ply laminates, however, only a portion of the true composite repeating unit cell is considered (see Figure 1.4). Similarly, the crimp model considers only a portion of the true repeating unit cell, but adds crossover of the fiber yarns (see Figure 1.5). The bridging model combines the mosaic and crimp models (see Figure 1.6) by taking weighted averages of effective stiffness terms in order to account for the two-dimensionality of the weave repeating unit cell. This model still represents a highly idealized geometric representation of a woven composite, but, like the mosaic and crimp models, it offers the ability to model composites reinforced with some more complex weaves beyond the plain weave pattern.

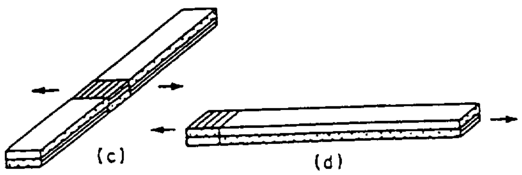

Figure 1.4. Mosaic model geometry. (Chou and Ishikawa, 1989)

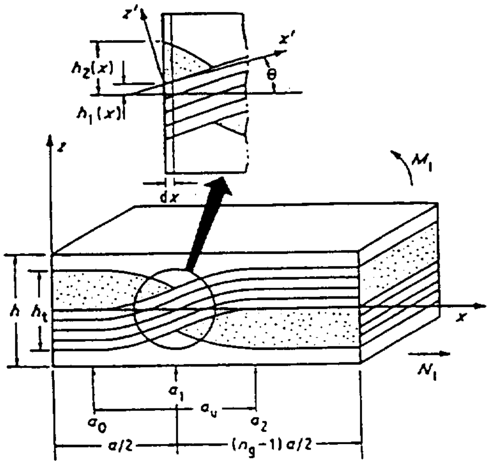

Figure 1.5. Crimp model geometry. (Chou and Ishikawa, 1989)

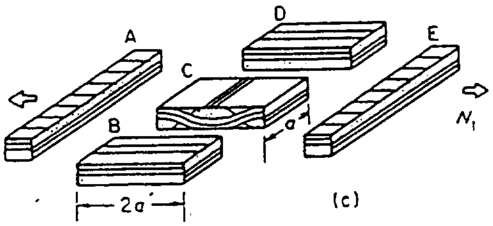

Figure 1.6. Bridging model geometry (Chou and Ishikawa, 1989).

Naik and co-workers have developed several models for plain weave composites based on the approach of Kabelka (1980, 1984). Kabelka's approach was to consider a repeating element from a single cross-section of the composite in each of the fiber directions. The geometry is shown in Figure 1.7, where warp and weft refer to the two fiber directions in the biaxial plain weave reinforcement pattern (weft is also referred to as fill). Expressions were developed for the local dimensions and fiber angles in these cross-sections. The effective properties of the cross-sections were then taken as the mean integral values of the local effective properties determined via classical lamination theory. This method is unrealistic in that it models the behavior of the composite as the behavior of one cross-section or "slice" of the geometry in each direction, while in reality the cross-sectional geometry is changing throughout the composite. Naik and Ganesh (1992) remedied this limitation by performing a Kabelka-type analysis on a number of "slices" from the three-dimensional plain weave composite unit cell, and assembling these slices under an iso-strain condition. The authors refer to this model as the Slice Array Model (SAM) (see Figure 1.8). The Element Array Model (EAM) considers slices taken in both in-plane directions such that discrete elements, rather than slices, are formed (see Figure 1.9). Each element is modeled with classical lamination theory, and the elements are assembled in one direction to form slices, and then in the other direction to form the repeating unit cell of the plain weave composite. The elements are assembled under the iso-stress condition along the loading direction and under the iso-strain condition across the loading direction. The order in which these two assembly processes proceed distinguishes two distinct models whose predictions vary significantly. Comparison with experimental in-plane modulus data for plain weave graphite/epoxy show that one model or the other is reasonably accurate for the various composite properties. However, the SAM and EAM models consider only elastic phases and have only been applied to plain weave composites.

A model developed by Karayaka and Kurath (1994) uses a homogenization technique in conjunction with classical lamination theory. Effective (homogeneous) properties of a single ply of a woven composite representative volume element are determined via a unit cell analysis in which in-plane strains and out-of-plane stresses are assumed to be constant in the composite. The effective properties of the woven composite plies are then used in classical lamination theory to model a nine-ply 5-harness satin weave graphite/epoxy laminate. Comparison with experimental data indicates that the elastic predictions of the model are reasonably accurate.

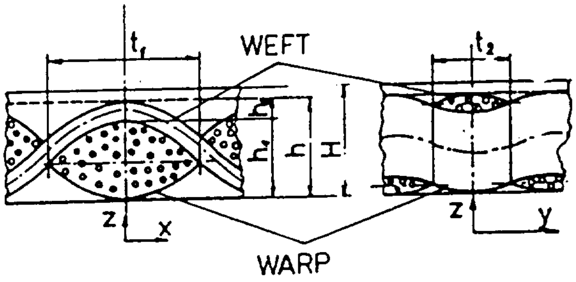

Figure 1.7. Cross-section geometry modeled by Kabelka (1984)

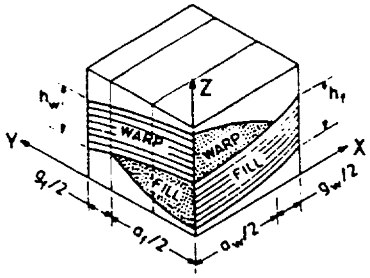

(a) UNIT CELL

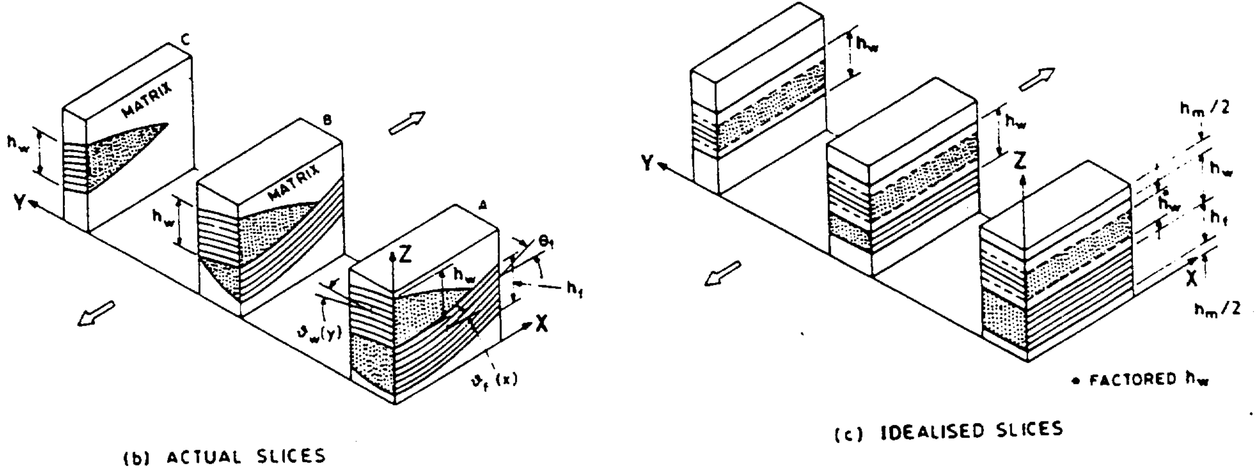

(b) ACTUAL SLICES

(c) IDEALISED SLICES

Figure 1.8. SAM model geometry (Naik and Ganesh, 1992).

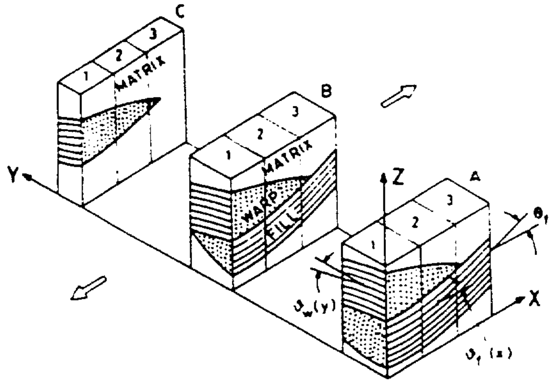

(a) SERIES-PARALLEL COMBINATION

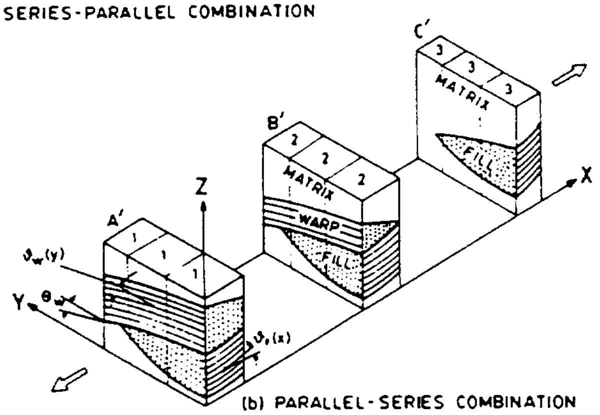

(b) PARALLEL-SERIES COMBINATION

Figure 1.9. EAM model geometry (Naik and Ganesh, 1992).

1.3 Mechanical Testing of Woven Composites

The above review of woven composite modeling research indicates that the effort thus far has concentrated exclusively on application to polymer matrix composites. The experimental work performed thus far on woven composites has been similarly focused (for example: Adams and Walrath (1987); Gause and Alper (1987); Gong and Sankar (1991); Fujita *et al.* (1993); Kang and Lee (1994); Zhou and Davies (1995); Rodriguez *et al.* (1996)). In addition, much of the experimental work has been centered on the fracture and failure of woven polymer matrix composites (for example: Kriz (1985); Reifsnider and Mirzadeh (1988); Harding (1993); Jackson and Ifju (1994); Fujii *et al.* (1994); Miyano *et al.* (1994); Xiao and Bathias (1994); Fleck *et al.* (1995); Fujii and Lin (1995)).

A significant conclusion pertaining to experimental work on woven composites was drawn by Ifju *et al.* (1995). This conclusion is that the repeating volume element of the reinforcement weave is often as large or larger than the strain gauges commonly used for strain measurement on unidirectional composites. Thus, when strain gauges are used, the measured strain values may not represent the average strains for the specimen, but rather the strains resulting from the local geometry of the composite. As will be shown, this conclusion has ramifications that transcend woven polymer matrix composites.

1.4 Carbon and Graphite Fiber-Reinforced Copper Matrix Composites

Carbon/copper (C/Cu) and graphite/copper (Gr/Cu) composites are candidate materials for high heat flux aerospace applications because of the high thermal conductivity offered by the copper matrix. By compositing the copper with carbon or graphite fibers, lower density, higher strength, higher stiffness, and less thermal expansion can be realized compared to pure copper and other traditional high thermal conductivity materials. As future spacecraft and satellites become larger and more complex, they will require more power. Higher power demands will necessitate a larger heat rejection system with a higher operating temperature. The potential thermo-mechanical properties represented by C/Cu and Gr/Cu are ideal for application in the radiators of such space power systems.

A significant amount of work has been done on unidirectional Gr/Cu composites (Ellis, 1992; Bednarcyk and Pindera, 1994; DeVincent, 1995), though production of the material has continued to be somewhat problematic. Fiber-matrix bonding has been a concern because copper does not wet graphite or carbon fibers. Thus alloying the copper matrix with small amounts of chromium and titanium has been used to improve the wetting, and thus improve the interfacial bond. Porosity, incomplete matrix infiltration, and nonuniform fiber distribution have also hindered unidirectional C/Cu and Gr/Cu composite production in the past. Cracking and buckling have occurred during the production of some C/Cu and Gr/Cu plates. Only recently has a reliable pressure infiltration casting procedure for producing small unidirectional C/Cu and Gr/Cu plates been developed. By employing a woven reinforcement phase, the production of these composites has been simplified and made more reliable.

1.5 8-Harness Satin Carbon/Copper

The present investigation considers a woven C/Cu composite. By employing a woven reinforcement phase, it is hoped that nonuniform fiber distribution effects can be minimized, while the ease of manufacture can be enhanced. In addition, components fabricated from C/Cu may have complex shapes. Thus, the ability to use a woven or braided net-shaped preform is desirable.

An 8-harness satin carbon cloth serves as the preform for the composites produced for this investigation. This cloth is biaxial; thus the continuous carbon fiber yarns are oriented in two normal directions. These directions are referred to as the fill (0°) and warp (90°) directions. In traditional woven fabrics, the fill yarns were put in place, then the warp yarns were woven in and out of the fill yarns.

Figure 1.10 shows optical micrographs of a C/Cu-Cr composite. In the micrograph, the copper matrix is white, the carbon fibers are gray, and voids are black. The presence of voids indicates that either complete infiltration of the carbon yarns by the matrix was not achieved, or that porosity arises during cool-down from the fabrication temperature. Whatever the cause of this yarn porosity, it is a feature of the composite which must be considered.

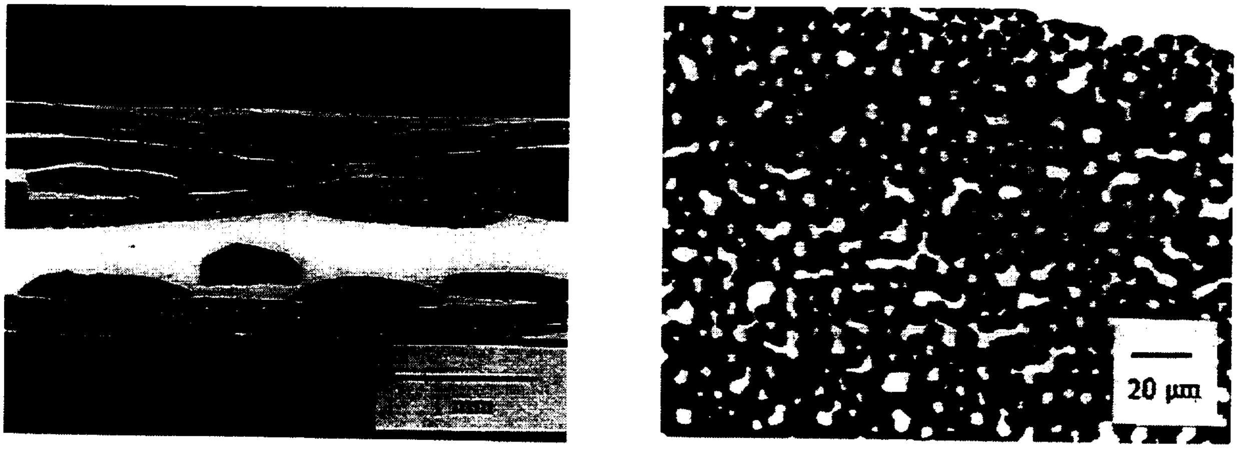

Figure 1.10. Optical micrographs of 8-harness woven C/Cu. a) Plate cross-section. b) Fiber/matrix yarn.

1.6 Objectives of Present Investigation

The objectives of this investigation are to characterize the mechanical response of the novel 8-harness satin woven C/Cu material and to model the tensile, compressive, and shear response of this material. The experimental phase of the investigation includes monotonic and cyclic tension and compression tests, combined tension-compression tests, and monotonic and cyclic Iosipescu shear tests. Test specimens with three matrix types, i.e., Cu, Cu-Cr, Cu-Ti, were prepared with either the fill (0°) or warp (90°) direction of the reinforcement weave oriented longitudinally. As previously mentioned, small amounts of titanium and chromium were added to the copper matrix to improve the fiber-matrix bond. Thus, the effects of the different matrix alloys, as well as the effect of the weave orientation, can be observed.

The mechanical characterization includes determination of initial moduli, yield stress, post-yield behavior, including hardening and the possible role of damage on the hysteretic behavior, and ultimate strength. The strain measurements in the mechanical tests were obtained predominantly using strain gauges. Thus, the work by Ifju *et al.* (1995) suggesting that surface strains in a woven composite could be highly nonuniform due to the large weave repeating unit cell is relevant. Hence, an additional objective of the mechanical tests was to characterize the effect of the strain nonuniformity, and how it affects the strain measurements.

The modeling phase of the present investigation involves an extension of the three-dimensional method of cells (GMC-3D). This extension allows the geometry of the woven composite to be "built up" from subcells which represent yarns of fibers impregnated with the matrix material. Plastic behavior of the metal matrix is also accommodated in the extended model. The model is discussed in detail in Section 4.

The model is used to examine the effect of refining the representative geometry of the composite, the effect of altering the composite fiber volume fraction, the effect of strain gauge size and placement (as affected by surface strain nonuniformity), and the effect of porosity in the fiber yarns on the tensile response of 8-harness satin woven C/Cu. The tensile, compressive, and shear response predicted by the model is then compared to the experimentally determined response in order to evaluate the degree to which the objective of developing an accurate model for the woven C/Cu is achieved.

2. Experimental Methodology

2.1 Test Specimens

The C/Cu composite plates for the experimental phase of this investigation were produced by Metal Matrix Castings, Inc. under contract to NASA Lewis Research Center. A proprietary pressure infiltration casting technique was used. For details of the fabrication procedure, see DeVincent (1995). A total of eighteen 3 inch by 8 inch composite plates were cast. All plates were reinforced with three layers of Amoco 8-harness satin VCX-11 carbon fiber cloth and cast such that the fill yarn direction was aligned with the 8 inch direction in the plates. Three types of matrices were used. Six plates were cast with each matrix type: pure copper; copper with 0.7 percent (by weight) chromium; copper with 0.5 percent (by weight) titanium. These three types of composites will be referred to as C/Cu, C/Cu-Cr, and C/Cu-Ti, respectively.

Tension, tension-compression, and Iosipescu shear test specimens were machined from the plates via wire electrical discharge machining at NASA Lewis Research Center. The two specimen layouts according to which the specimens were cut from the plates are shown in the appendix. Three plates of each matrix type (Cu, Cu-Cr, Cu-Ti) were cut following each of the two layouts. Figure 2.1 shows details of the three types of mechanical specimens used in this investigation, and Figure 2.2 shows a picture of typical specimens. The total number of each type of specimen tested is summarized in Table 2.1. It should be noted that the combined tension-compression type specimens were used for the monotonic and cyclic compression tests as well as the combined tension-compression tests. No tension-compression type specimens were produced in the 90° orientation due to the length requirement of the specimen (4 inches) and the width restriction of the plates (3 inches).

Strain gauges were used for strain measurement in all mechanical tests. The standard gauge configuration for tension specimens was a 10 mm (gauge length) unidirectional strain gauge on one side, and a 3 mm strain gauge rosette on the reverse side. Fiberglass tabs were bonded to the ends of all tension specimens in order to allow application of sufficiently high gripping pressure to prevent the specimen from slipping in the grips prior to failure. The standard strain gauge configuration for tension-compression specimens was a 5 mm rosette on one side and a 10 mm unidirectional strain gauge on the reverse side. The standard strain gauge configuration for the Iosipescu shear specimens was a 3 mm rosette on one side and a 3 mm unidirectional strain gauge on the reverse side.

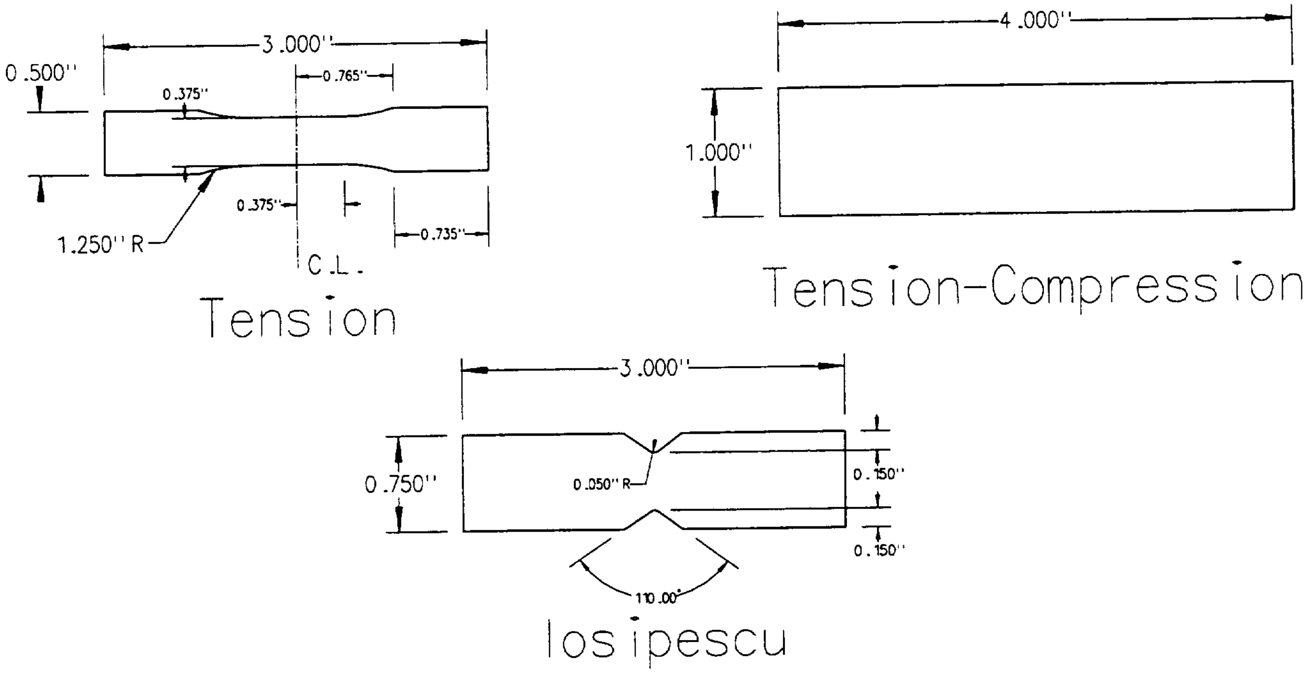

Figure 2.1. Detail of the mechanical test specimens.

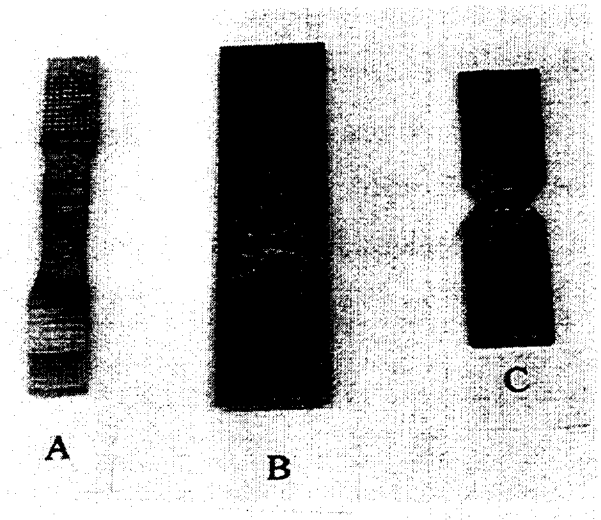

Figure 2.2. Test specimens. a) Tension. b) Tension-compression. c) Iosipescu shear.

Table 2.1. Summary of test specimens.

Matrix Alloy	Specimen Type	Weave Orientation	Number Tested
Cu-Cr	Tension	0°	6
		90°	12
	T-C	0°	9
		90°	0
	Shear	0°	6
		90°	6
Cu-Ti	Tension	0°	3
		90°	12
	T-C	0°	6
		90°	0
	Shear	0°	6
		90°	6
Cu	Tension	0°	3
		90°	12
	T-C	0°	9
		90°	0
	Shear	0°	6
		90°	6

2.2 Loadstand and Data Acquisition

Testing was performed on an 810 Materials Testing System (MTS) Axial Tension/Compression loadframe with a capacity of 22 kips. This loadframe operates under the guidance of four controls which act as one system: the MicroConsole, AC/DC Controllers, Function Generator, and the MicroProfiler. This apparatus is shown in Figure 2.3. Data acquisition was performed using the National Instruments® LabVIEW software package.

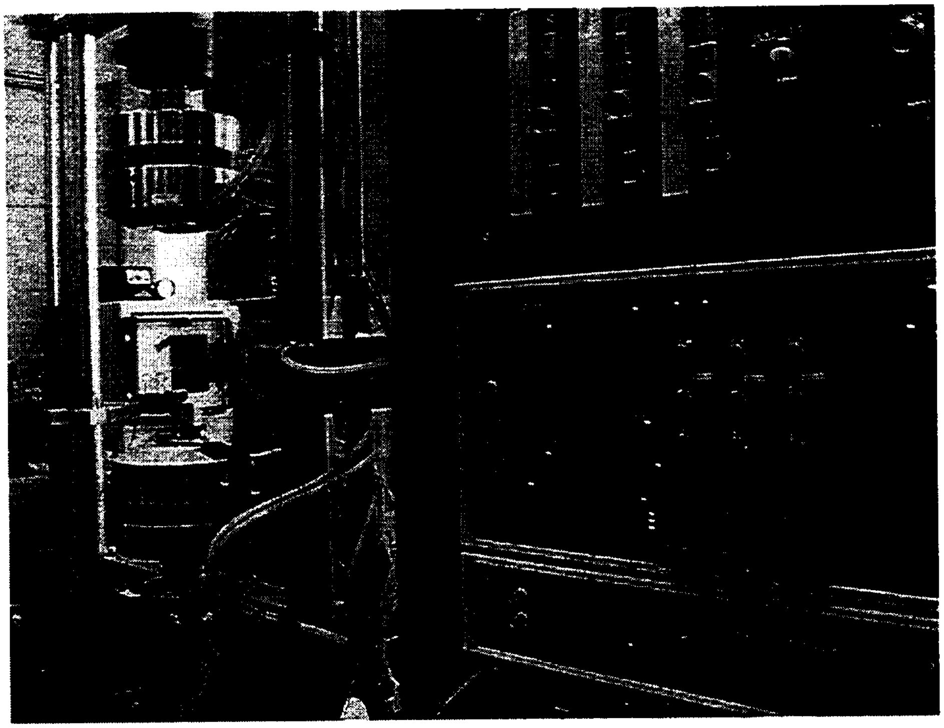

Figure 2.3. Loadstand and controller apparatus

2.3 Testing Procedure

Table 2.2 summarizes the control method and the stress rate or displacement rate used for the mechanical tests. The monotonic tests were conducted in displacement control while the cyclic tests were performed in load control for tension, compression, and combined tension-compression. Load control was used for the cyclic tests because it was desirable to prescribe unloading stresses rather than unloading displacements during the tests. It was not possible to accurately predict the strains associated with the unloading stresses due to the lack of accurate a priori knowledge of the inelastic stress-strain relation. Thus prescribing an unloading strain was not feasible. Due to the nature of the Iosipescu shear fixture, it was desirable to test both monotonic and cyclic shear specimens in displacement control. Thus the loading reversals for the cyclic shear tests were performed manually when the stress reached the desired level. In all cases, stress and strain rates were similar at similar points in the loading history.

Table 2.2. Testing control and rate summary.

Test	Control	Rate
Monotonic Tension	displacement	0.0025 in./min.
Cyclic Tension	load	2.5 ksi/min.
Monotonic Compression	displacement	0.0025 in./min.
Cyclic Compression	load	2.5 ksi/min.
Tension-Compression	load	2.5 ksi/min.
Compression-Tension	load	2.5 ksi/min.
Monotonic Shear	displacement	0.0025 in./min.
Cyclic Shear	displacement	2.5 ksi/min.

2.3.1 Tension Tests

The gripping apparatus for the tension tests is shown in Figure 2.4. Specimen gripping was accomplished via a novel procedure using a hybrid of the off-axis gripping system developed by Pindera and Herakovich (1985). The system consists of one half of a bell house gripping mechanism, which eliminates the effects of bending due to uneven gripping or off-axis specimen behavior. Although only half of the bell-housing mechanism was used (because of the small specimen length), a significant reduction in specimen bending was observed compared to earlier tests performed without the off-axis grips.

Once the tensile specimen was gripped and in place, it was subjected to five one minute loading cycles between 0 ksi and 1 ksi (load control). These cycles served to 'seat' the gauges on the specimen, and to allow verification of proper testing apparatus set up. After these initial shake-down cycles, some specimens were tested monotonically to failure in displacement control at a rate of 0.0025 in/min. Other tensile specimens were cycled in load control between 0 ksi and nominal stress levels of 5, 7.5, 10, 15, 20, and 30 ksi, at a rate of 2.5 ksi/min. These cyclic tension tests were subsequently conducted to failure in displacement control with a monotonic rate of 0.0025 in./min. Table 2.3 provides a summary of monotonic and cyclic tension tests performed on each type of specimen.

In order to verify strain gauge readings and to examine strain gauge size effects, six additional tension tests were performed. Three tension-compression specimens were cut in half longitudinally to provide six 4 inch by 1/2 inch rectangular specimens. The larger size of these specimens compared to the standard tension specimens allowed additional strain measurement instrumentation. Strain was measured for each of these long specimens using a 3 mm rosettes, a 30 mm unidirectional strain gauge, as well an MTS 1 inch gauge length extensometer. Results of these tests are presented in Section 3.

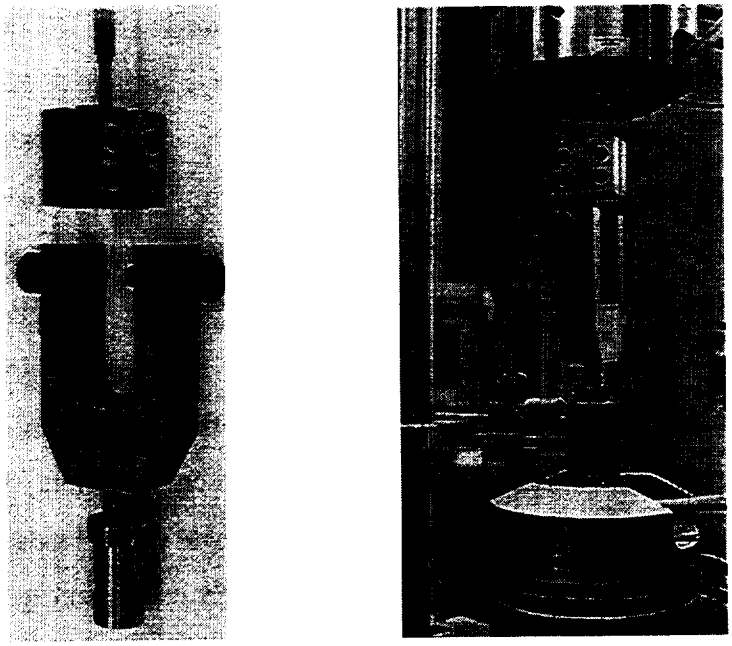

Figure 2.4. a) Tension grips with specimen. b) Gripping setup for tension tests.

Table 2.3. Summary of tension test specimens.

Matrix Alloy	Test Type	Weave Orientation	Number of Tests
Cu-Cr	monotonic	0°	3
		90°	6
	cyclic	0°	3
		90°	6
Cu-Ti	monotonic	0°	3
		90°	5
	cyclic	0°	0
		90°	4
Cu	monotonic	0°	3
		90°	6
	cyclic	0°	0
		90°	6

2.3.2 Combined Tension-Compression Tests

Figure 2.5 shows the tension-compression gripping system and how the system is held in the loadstand. The tension-compression type specimen, and the tension-compression gripping apparatus was used for the following tests: monotonic compression, cyclic compression, tension-compression (T-C), and compression tension (C-T). The tension-compression gripping apparatus is a novel design developed by Lin and Pindera (1988) specifically for investigation of the nonlinear response of metal matrix composites. The specimen is gripped outside of the fixture in an aluminum trough. This trough is machined to fit the grips, and it allows exact alignment of the tension-compression specimen. The specimen and the grips are then placed in the fixture, which itself is designed with several noteworthy features that allow accurate testing. To prevent the gross bucking of the specimen in compressive loading, four side support plates contact the sides of the specimen. Tapered wedges are slid into place between the grips and the inside surfaces of the fixture housing blocks to eliminate play. A bi-directional joint is used to transmit the load from the loadstand to the fixture, both in tension and compression. The pins, of which this joint is composed, can be adjusted to eliminate misalignment of the loadstand crosshead and bottom support plate. The grips allow for both compression or tension to be applied to the specimen. They also allow the load to progress from compression to tension or from tension to compression within a single test.

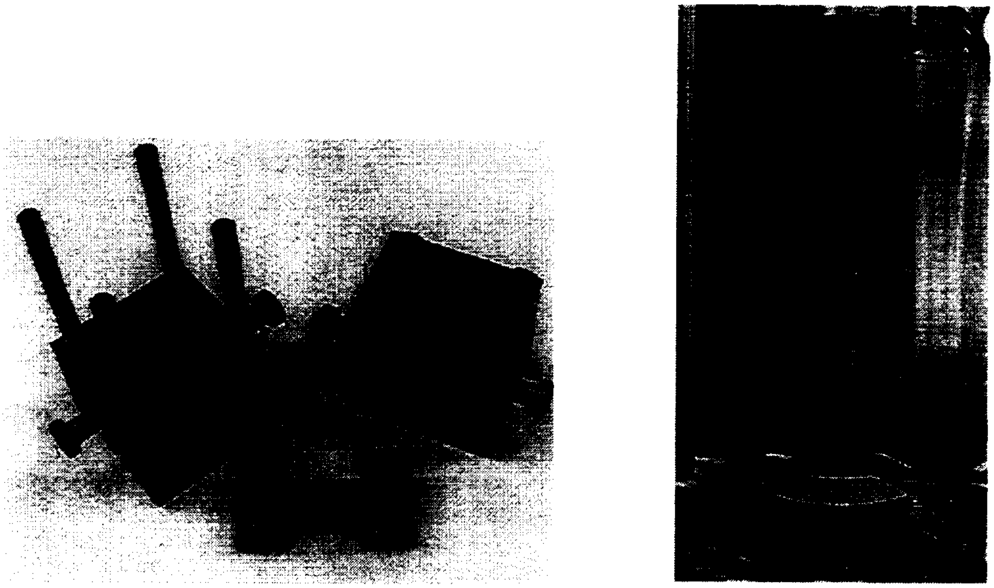

Figure 2.5. a) Tension-compression grips with specimen. b) Gripping setup for T-C tests.

Once placed in the loadstand, all specimens were cycled in tension-compression to seat the gauges similarly to, and at the same loading rate as the tension specimens. Monotonic compression tests were performed to failure in load control at a compressive stress rate of 2.5 ksi/min. For the cyclic compression tests, the specimens were cycled between 0 ksi and compressive stress levels of 2.5, 5, 7.5, 10, and 15 ksi. These tests were performed in load control at a rate of 2.5 ksi/min.

The combined T-C and C-T tests were also performed in load control at a rate of 2.5 ksi/min. The loading profile for T-C tests was: 2.5, -2.5, 5, -5, 7.5, -7.5, 10, -10, 12.5, -12.5, 15, and -15 ksi, where a negative stress denotes compression. The C-T tests were performed to the same stress levels, except the compression loading was done first. Table 2.4 provides a summary of the monotonic compression (MC), cyclic compression (CC), T-C, and C-T tests performed on each type of specimen.

Table 2.4. Summary of tests for T-C type specimens.

Matrix Alloy	Test Type	Weave Orientation	Number Tested
Cu-Cr	MC	0°	3
	CC	0°	2
	T-C	0°	2
	C-T	0°	2
Cu-Ti	MC	0°	3
	CC	0°	1
	T-C	0°	1
	C-T	0°	1
Cu	MC	0°	3
	CC	0°	2
	T-C	0°	2
	C-T	0°	2

2.3.3 Iosipescu Shear Tests

An Iosipescu fixture, shown in Figure 2.6, was used to conduct both the monotonic and cyclic shear tests. The Iosipescu fixture allows the gauge portion of a notched specimen to experience a state of nearly pure shear (Pindera *et al.*, 1987). In these tests, the strain gauge was seated by again cycling the specimen five times between 0 ksi and 1 ksi in load control at a rate of 2 ksi/min. Monotonic tests were performed in displacement control at a rate of 0.0025 in/min. The cyclic tests were also performed in displacement control, thus the reversals of the cross-head direction were performed manually in order to achieve desired peak stresses. In this manner the shear specimens were cycled between 0 ksi and 2, 4, 5.5, 7 ksi, and finally extended to a "load plateau". Table 2.5 provides a summary of the monotonic and cyclic shear tests performed on each type of specimen.

Figure 2.6. Iosipescu shear fixture with specimen.

Table 2.5. Summary of Iosipescu shear test specimens.

Matrix Alloy	Test Type	Weave Orientation	Number Tested
Cu-Cr	monotonic	0°	5
		90°	5
	cyclic	0°	1
		90°	1
Cu-Ti	monotonic	0°	5
		90°	5
	cyclic	0°	1
		90°	1
Cu	monotonic	0°	5
		90°	5
	cyclic	0°	1
		90°	1

2.4 Strain Gauge Size Considerations

The observations of Ifju *et al.* (1995) regarding nonuniform surface strains in woven composites (see Section 1.3) are directly applicable to this investigation. In order to obtain strain values from strain gauges which accurately represent the average strain in the specimen, the strain gauge should be as large as possible. A strain gauge with a large gauge length provides more reliable strain values because of the large repeating unit cell of the 8-harness satin reinforcement weave. This is shown schematically in Figure 2.6. It is the large repeating unit cell that gives rise to macroscopic surface strain gradients as described by Ifju *et al.* (1995).

The repeating unit cell is the smallest portion of the weave geometry from which the entire weave can be "built up" by repeatedly placing identical unit cells adjacent to each other in the plane of the weave. For an 8-harness satin weave, this unit cell consists of an area encompassing eight yarns in each direction (since a yarn follows the pattern: over one, under seven, over one, under seven, etc. ...). The repeating unit cell is outlined and labeled in Figure 2.6. Since the unit cell repeats infinitely to form the weave, the thermomechanical behavior of each unit cell can be assumed to be identical. However, within a unit cell, the thermomechanical behavior will vary significantly. This remains true when the weave is infiltrated to form a composite. Thus, when loading is applied to a woven composite, the displacements, stresses, and strains vary from point to point in the composite, with respect to the weave. If average values for the field variables are desired, they must be measured for an integral number of repeating unit

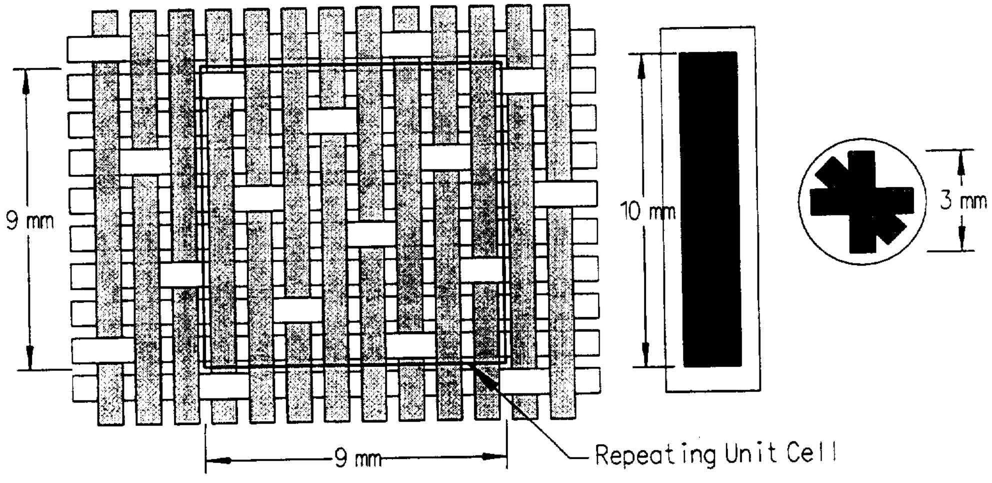

Figure 2.6. Schematic representation of the 8-harness satin weave repeating unit cell and strain gauge dimensions.

cells of the weave. Unfortunately, the strain gauge cannot be selected (or placed) such that it covers one, and only one, weave repeating unit cell.

For the 8-harness satin C/Cu composites tested, the dimensions of the weave repeating unit cell were approximately 9 mm by 9 mm. Hence, measuring the strain with a 3 mm gauge length device, such as the rosette shown in Figure 2.6, yields local strain values. The strain readings obtained from the rosette will vary depending on where the rosette was placed with respect to the weave. This point was observed by Ifju *et al.* (1995), and it can be seen quite clearly in Figures 2.7(a) and (b). Figure 2.7(a) shows the stress-strain curves for six 90° C/Cu-Cr tension specimens where the strains were measured by the longitudinal arm of the 3 mm rosette. Figure 2.7(b) shows the stress-strain curves for the same six specimens where the strains were measured by the 10 mm unidirectional strain gauge. The greater degree of scatter present in the rosette results is due to weave-induced surface strain gradients, and the fact that the rosette is measuring the strain over a small region of the surface. The 10 mm gauge spans an entire weave repeating unit cell, and thus the scatter in the stress-strain curves between specimens is much less. The 10 mm gauge provides strain values which are closer to the quantity that is desired: the average composite strain.

It should also be noted from Figures 2.7(a) and (b) that the scatter is small for both the rosette and the unidirectional gauge in the linear elastic region of the stress-strain curves. Only when plastic deformation begins to occur do the surface strain gradients become sufficiently large to affect the strain measurements.

Tensile test results from the six 4 inch by 1/2 inch specimens, formed by cutting three tension-compression specimens, substantiate the above conclusions. A typical stress-strain curve from such a test is shown in Figure 2.8. In this case a 3 mm rosette, a 30 mm unidirectional strain gauge, and a 1 inch extensometer were used to measure the strain. The specimen was unloaded at 10 ksi and subsequently reloaded in order to confirm that the strain gauge size effect would act the same for cyclic testing. All three measuring devices agree well in the linear elastic region, but once plastic deformation set in, the rosette strain readings diverge significantly. The extensometer and 30 mm gauge, on the other hand, agree well throughout the loading cycle. The slight divergence during unloading and reloading is probably due to extensometer slippage.

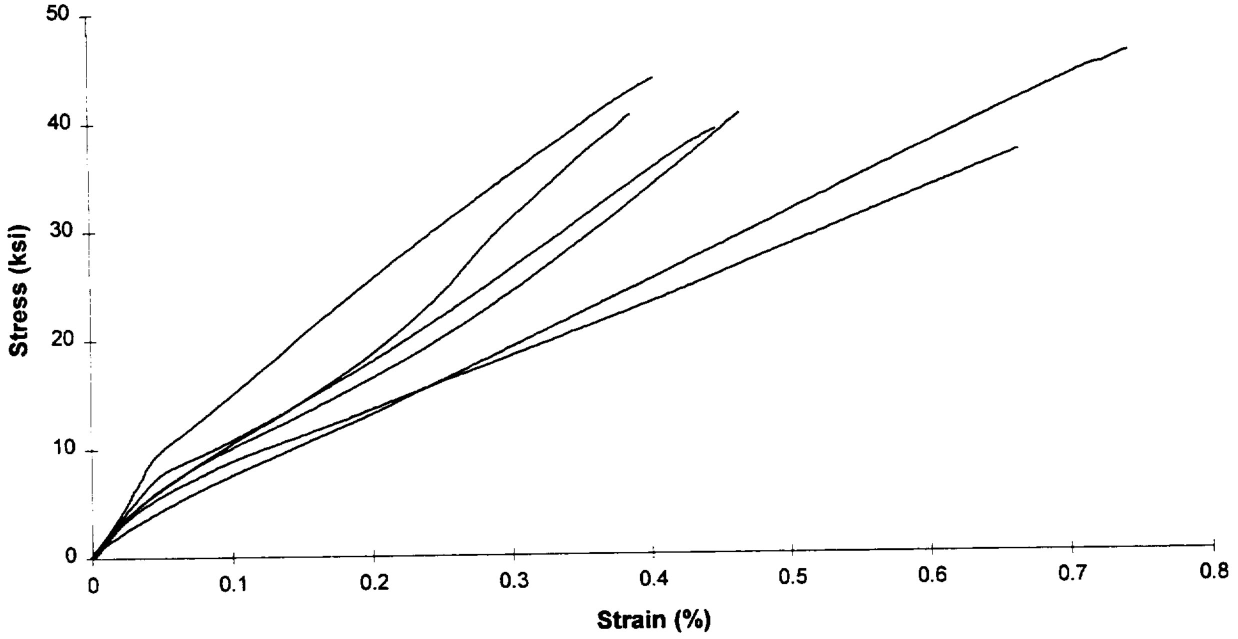

Figure 2.7(a). Scatter in experimental stress-strain results when strain is measured with a 3 mm rosette.

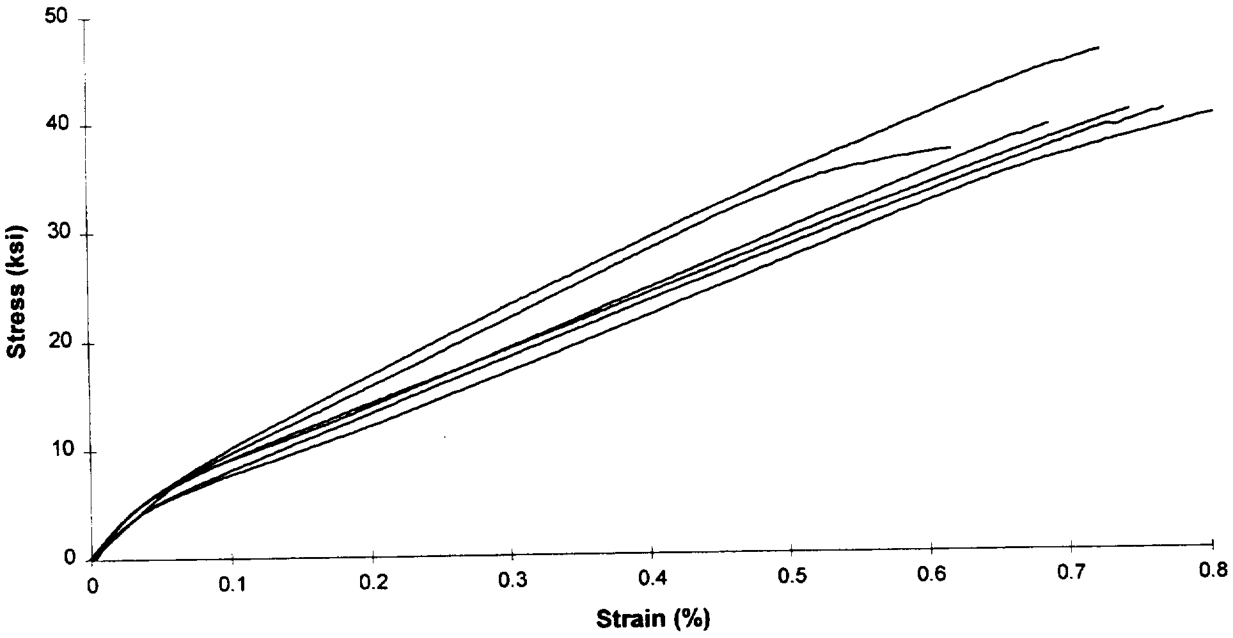

Figure 2.7(b). Scatter in experimental stress-strain results when strain is measured with a 10 mm unidirectional strain gauge.

Figure 2.8 suggests that using the extensometer or a 30 mm unidirectional strain gauge would have been desirable for all tests, but due to the size of the specimens (see section 2.1), this was not possible. The largest size strain gauge that fit in the tension specimen test section was a 10 mm gauge. This was also the largest gauge that could be used for the compression tests due to the configuration of the tension-compression fixture. Hence, all of the tension and compression data presented herein have been generated using the strain readings from the 10 mm gauges. This limits the data to longitudinal strain readings, thus Poisson ratios cannot be generated. This is understandable since the scatter in the 3 mm strain gauge results is exacerbated by the inherently small magnitude of transverse strain readings. This is illustrated in in appendix A.2, which shows the Poisson plots (negative transverse strain vs. longitudinal strain) for six tension tests on 90° C/Cu. The scatter is large, even in the elastic region. In fact, calculated values for the initial Poisson ratio for these tests varies from 0.339 to -0.092. Clearly, an attempt to characterize the transverse response of this material via conventional methods is futile.

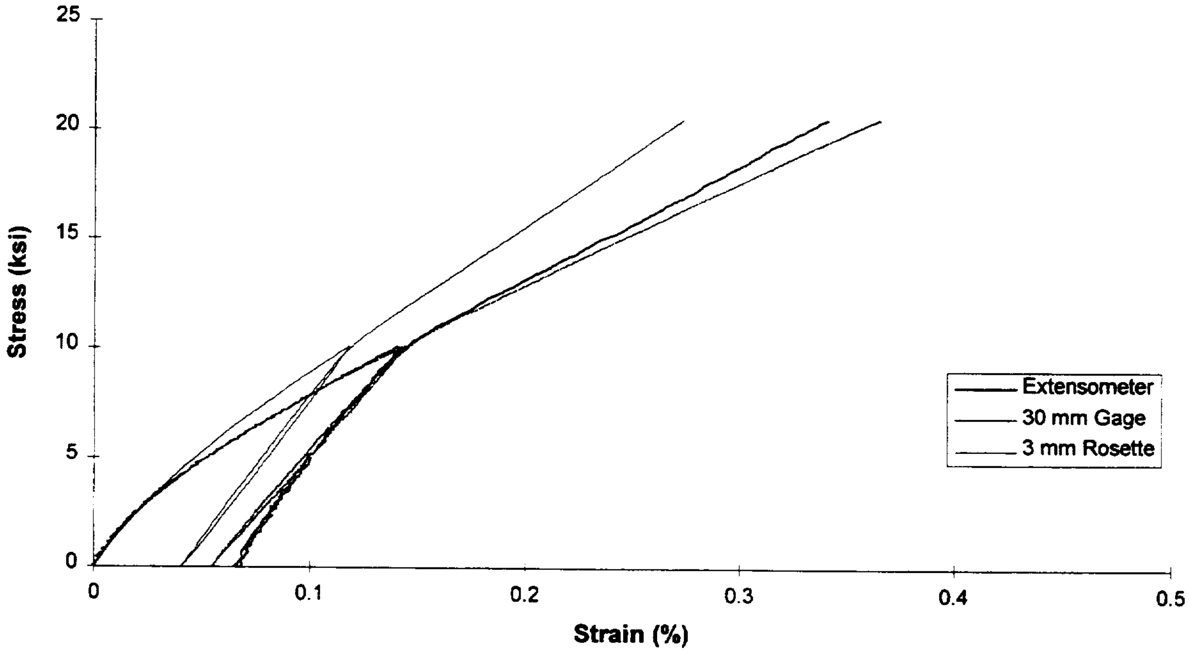

Figure 2.8. Typical stress-strain curve from a long specimen. Strain was measured using a 3 mm rosette, a 30 mm unidirectional gauge, and a 1 inch extensometer.

3. Experimental Results

3.1 Tension and Compression Tests

3.1.1 Monotonic Tension and Compression

Figure 3.1 shows the results of typical tension and compression tests for 8-harness satin C/Cu. The tensile response of the copper matrix and that of the graphite fiber (in the longitudinal and transverse directions) are included for comparison. The curves shown in the figure are for C/Cu-Cr specimens with 0° weave orientation (results for 90° specimens will be presented later). Several features in Figure 3.1 are noteworthy. First, in tension, the elastic portion of the stress-strain curve is quite small; yielding occurs at a stress lower than the yield stress for pure copper. This is because of stress concentrations in the matrix due to the fiber yarns and the presence of fiber yarns oriented transverse to the loading direction. Although the average stress applied to the composite is not sufficient to yield pure copper, at certain points within the composite (such as yarn cross-over regions) the local stresses exceed the yield stress of copper.

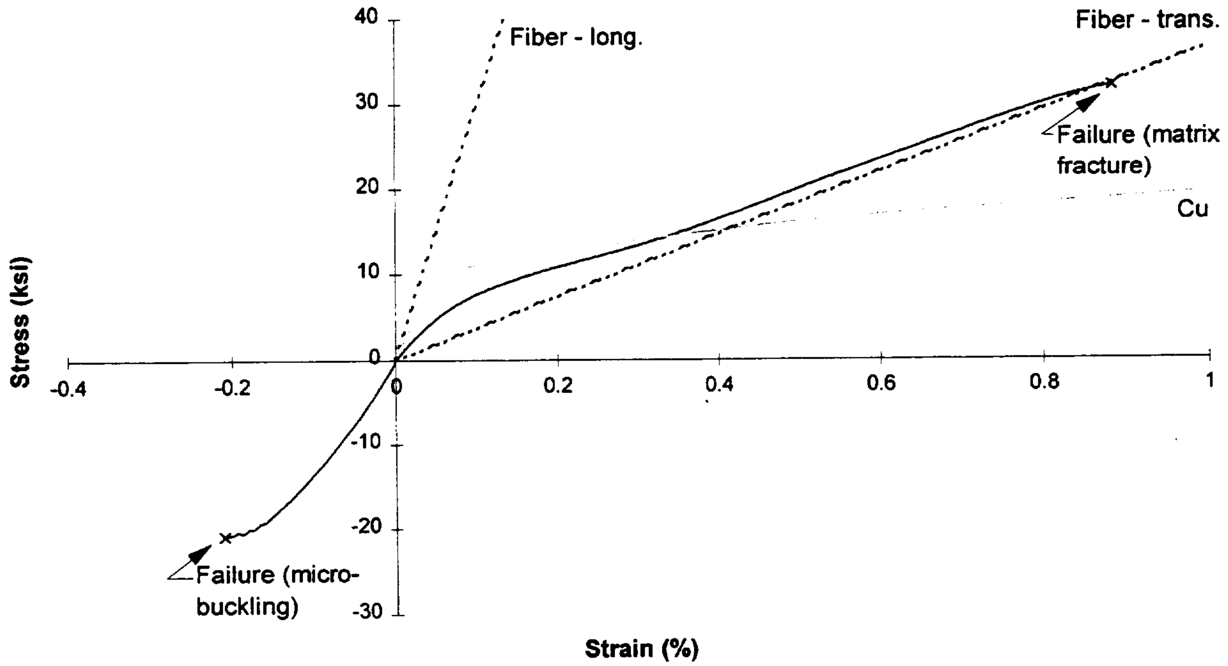

Figure 3.1. Typical monotonic tension and monotonic compression response for 8-harness satin C/Cu-alloy composites.

After yielding, the composite initially exhibits hardening typical of metals and metal matrix composites. The hardening is qualitatively similar to that of pure copper. At higher tensile strains (>0.3%), the composite exhibits stiffening. This behavior is due to the movement or rotation of the reinforcement weave as the yarns tend to straighten and the weave is deformed. As this occurs, the yarns become more aligned with the direction of the load; the waviness of the yarns, as they undulate in and out of the plane, is reduced. The better alignment of the yarns then allows them to support more load, and the composite behavior is stiffer. This stiffening behavior is typical of woven fabrics, and it can be readily observed by pulling on a portion of one's clothing.

Stiffening typically continued in tension until the onset of failure. Failure occurred by fracture of the copper matrix between the reinforcement yarns and was accompanied by an audible "pop", and an abrupt drop in the load. The fiber yarns were left intact across the cracked matrix surfaces after failure, and these bridging fiber yarns prevented the crack from opening significantly.

In compression, the initial modulus of the composite is somewhat higher than that in tension due, most likely, to the grip constraint effect that will be discussed later (see Section 3.3 for numerical modulus results). The onset of plastic strain is more gradual than in tension, and the compressive yield stress seems to have a higher magnitude than the tensile yield stress. No stiffening occurred in compression since the fiber yarns do not tend to straighten. Compressive failure occurred at a much lower strain than in tension, and the mechanism of failure was micro-buckling of the layers of the reinforcement weave. This micro-buckling usually occurred near one of the grips, and the bowing of the weave layers in the failed specimens was visible. Figure 3.2 shows a photo-micrograph of the micro-buckling in a typical failed compression specimen. As compressive failure commenced, the load dropped gradually, and a faint ripping sound was audible.

Figure 3.3(a) shows the tensile and compressive stress-strain curves for the C/Cu composites with the three matrix alloy types with 0° weave orientation. Figure 3.3(b) shows typical tensile stress-strain curves for the composites with 90° weave orientation. Note that there was some scatter between specimens within each matrix alloy type and weave orientation (see

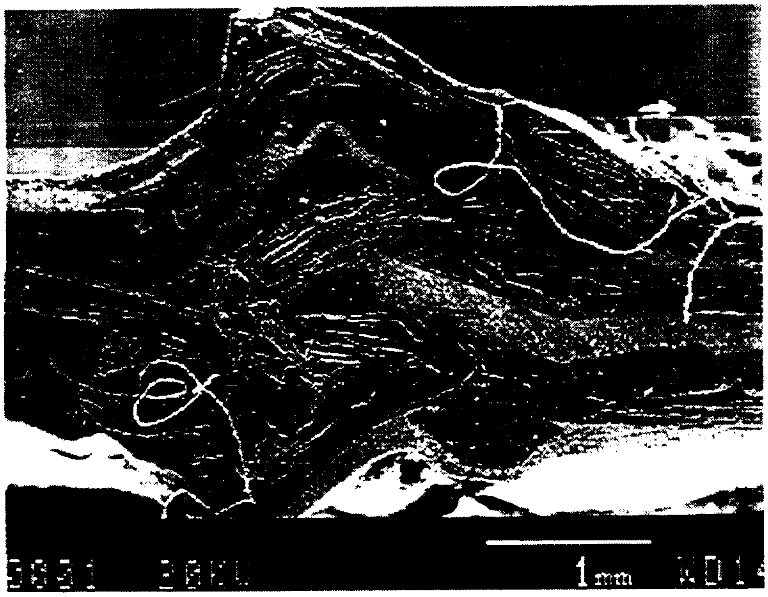

Figure 3.2. Photo-micrograph of micro-buckling in a tested compression specimen.

Figure 2.7(b), for example). The curves presented in the figures are representative of an average stress-strain response for the particular specimen type.

In the elastic region, little difference is observed in the stress-strain responses of the C/Cu-alloy composites, regardless of matrix alloy, weave orientation (compare Figures 3.3(a) and 3.3(b)), or whether they were tested in tension or compression. Differences due to these effects become substantially more apparent after the material yields. The differences among the stress-strain curves shown in Figures 3.3(a) and (b) should thus be explainable by considering the quality of the fiber-matrix bond in the specimens. The C/Cu-Cr composite has the largest amount of alloying element added to the matrix (0.7 wt. %). Thus, this composite would be expected to have the best fiber-matrix bonding, followed by C/Cu-Ti, and finally by C/Cu. The experimental tensile test data shows that in tension, poor fiber-matrix bonding *raises* the stress-strain curve (i.e., stiffer overall response), while in compression, poor fiber-matrix bonding *lowers* the stress-strain curve (i.e., more compliant overall response). It is not readily apparent why the bonding effect manifests itself in this way. In fact, in tension, it is somewhat opposite of what would be expected in a traditional composite.

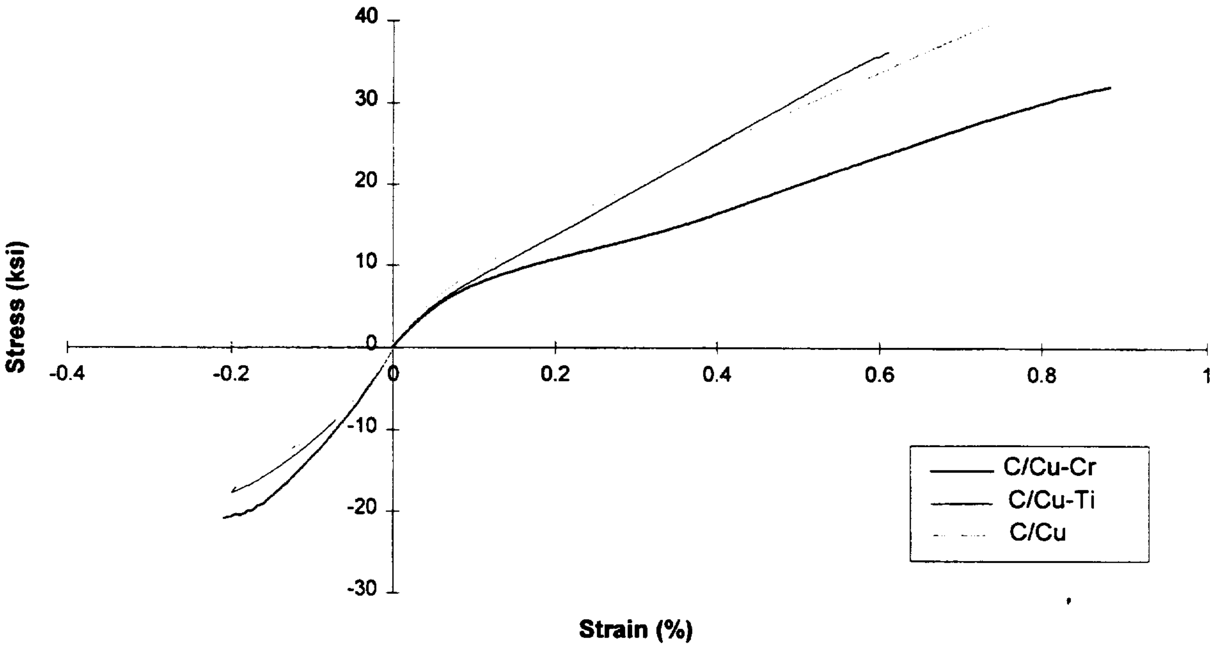

Figure 3.3(a). Typical monotonic tension and monotonic compression curves for 0° C/Cu-alloy specimens.

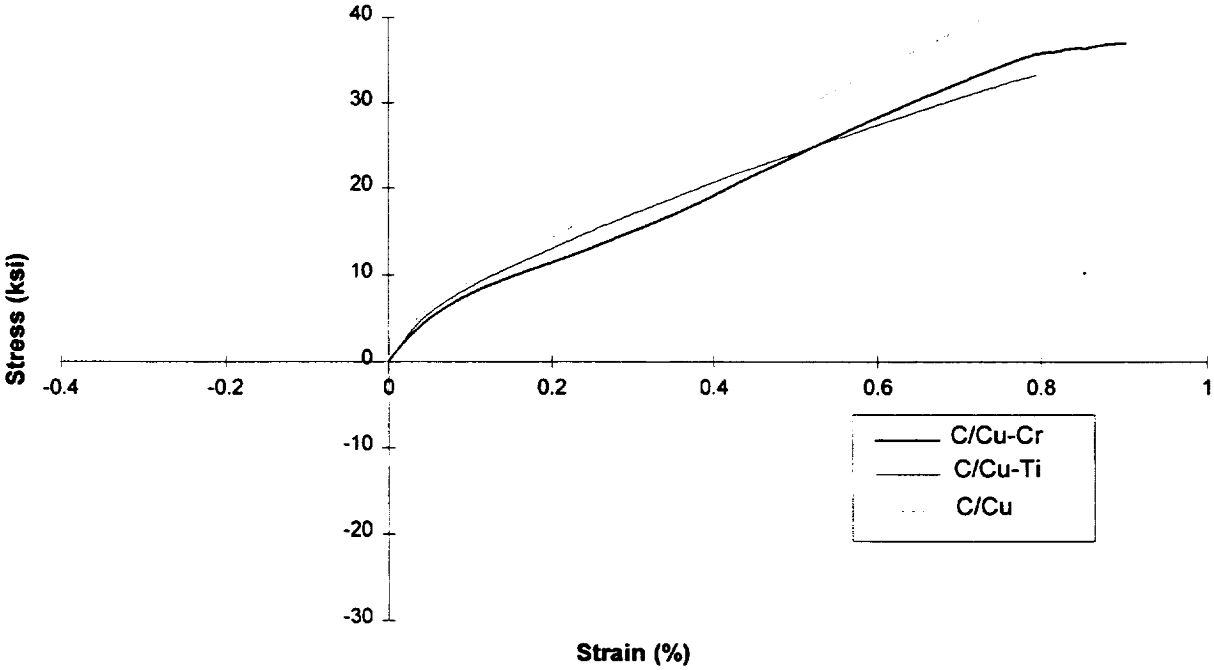

Figure 3.3(b). Typical monotonic tension curves for 90° C/Cu-alloy specimens.

In a traditional (non-woven) composite, such as a $[0°/90°]_s$ laminate for example, it would be expected that in tension, poor bonding in the 90° layers would cause the fibers to behave as holes and lead to a more compliant response. The 0° layers would not be affected significantly by the poor bonding. In compression, on the other hand, poor bonding would not affect the 90° layers significantly as the matrix would have no tendency to pull away from the fibers. If the matrix tends to expand away from the fibers in the 0° layers, the trend observed in compression in Figure 3.3(a) would be expected. The fibers would then be free to buckle within the space left by the expanding matrix. However, the axial Poisson ratio of the fiber is higher than the Poisson ratio of the copper matrix (see Table 5.2). Thus, in compression, the 0° fibers would expand transversely more than the copper matrix, and the interface would remain closed. The compressive data shows a trend that cannot be explained by traditional bonding arguments, while the experimental tensile data shows a trend opposite to that expected. Hence, although an 8-harness satin woven composite is similar to a [0°/90°] laminate, the differences between the reinforcement microstructure in these two composites must account for the unexpected trends in the data.

One possible explanation for the observed trends is that superior bonding leads to more load transfer between the fiber and the matrix in regions of high stress concentration. In this scenario, the regions in which yarns pass over one another in the weave pattern serve as "weak links". As the yarns tend to straighten in tension, a superior bond would allow more shear stress transfer to the matrix in the cross-over regions, and thus earlier yielding and more plastic flow. If this mechanism were to operate, it would result in a trend based on interfacial bonding opposite to that which follows from the traditional poor bonding argument discussed above. In compression, cross-over regions might serve as weak links as well, but in this case a superior bond would tend to restrict deformation. By acting to keep the fiber-matrix interface closed, superior bonding would prevent buckling of the fibers and allow less overall deformation. This would explain the trend in the compressive stress-strain curves in Figure 3.3(a).

The question remains as to why the effect of poor bonding in the cross-over regions has a greater impact on the observed tensile stress-strain curves than the effect of poor bonding on the tensile response of a biaxial laminate. It may be due partly to the poor transverse stiffness of the carbon fibers. The transverse modulus of the carbon fiber is 3.67 MPa, while the modulus of copper is 18.8 MPa. Thus, replacing the fiber with holes in 90° layers to simulate debonding probably would have a relatively minor effect. In addition, since the longitudinal modulus of the fiber is 29.42 MPa, the 0° layers are stiff and able to pick up stress transferred from the 90° layers (due to their decrease in stiffness) without a great deal of additional strain. Hence, in C/Cu composites, it appears that the effect of poor bonding on the transverse yarns is relatively small, and the effect of poor bonding on the deformation of the cross-over regions may dominate.

Importance of the weave cross-over regions in tension, and the effect of fiber-matrix bonding on these regions, is further evidenced by stiffening observed in Figures 3.3(a) and (b). C/Cu-Cr exhibits the largest amount of stiffening, followed by C/Cu-Ti, and finally C/Cu. Stiffening is due to straightening of the fiber yarns, concentrated in the cross-over regions. Thus, it appears that improved bonding causes more deformation in the cross-over regions, possibly due to the greater stress transfer to the matrix in these regions.

It should be noted that, due to the complexity of the effects being considered, arguments of the type presented above are mainly speculation. Confirmation of the mechanisms involved in the observed mechanical behavior would require a micromechanics model including fiber-matrix debonding. The above hypotheses will, however, be addressed further in this report.

3.1.2 Cyclic Tension and Compression

Figure 3.4(a) shows typical cyclic tension and cyclic compression curves for 0° C/Cu-Cr. Figures 3.4(b) and (c) show typical cyclic compression curves for 0° C/Cu-Ti and 0° C/Cu, respectively. Recall that due to material limitations, no 0° C/Cu-Ti or 0° C/Cu specimens were tested cyclically in tension.

The envelopes of both the cyclic tension and cyclic compression curves shown in Figure 3.4(a) appear similar to their monotonic counterparts (see Figure 3.1). Upon reloading for each cycle, the curves pass closely to the point of maximum stress reached in the previous cycle. In both tension and compression, the response is characterized by hysteresis loops beyond a certain stress level. In fact, the appearance of the unloading portions of the loops suggests that reverse yielding is occurring during unloading. Frictional effects caused by sliding along the poorly bonded fiber-matrix interface may contribute to the hysteretic behavior as well.

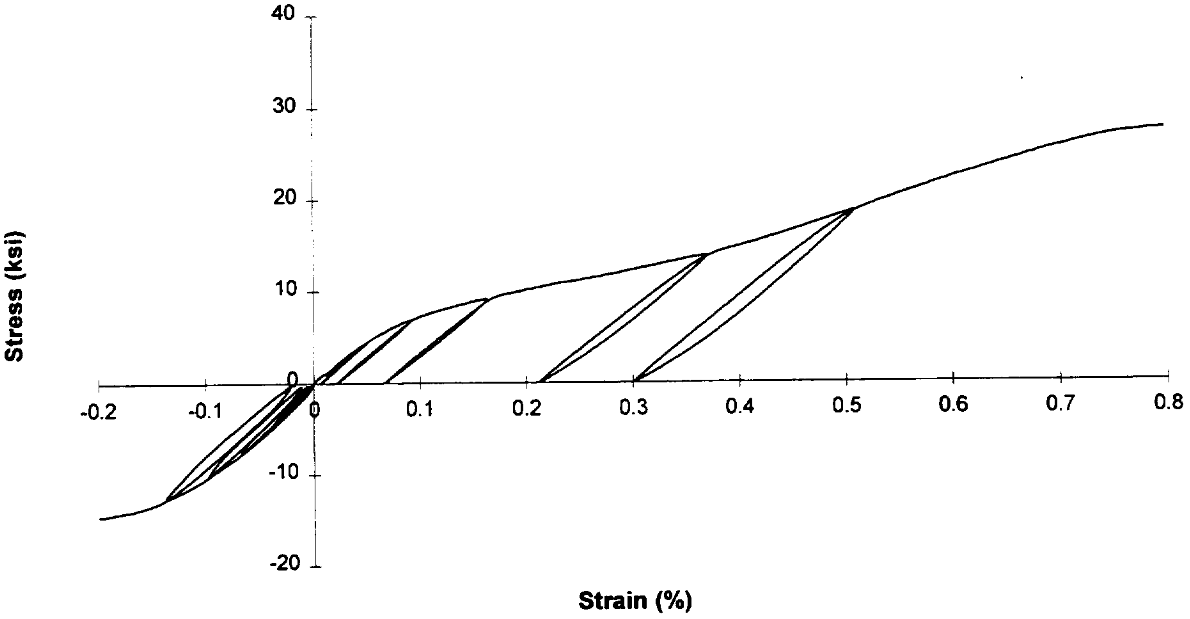

Figure 3.4(a). Typical cyclic tension and cyclic compression curves for 0° C/Cu-Cr.

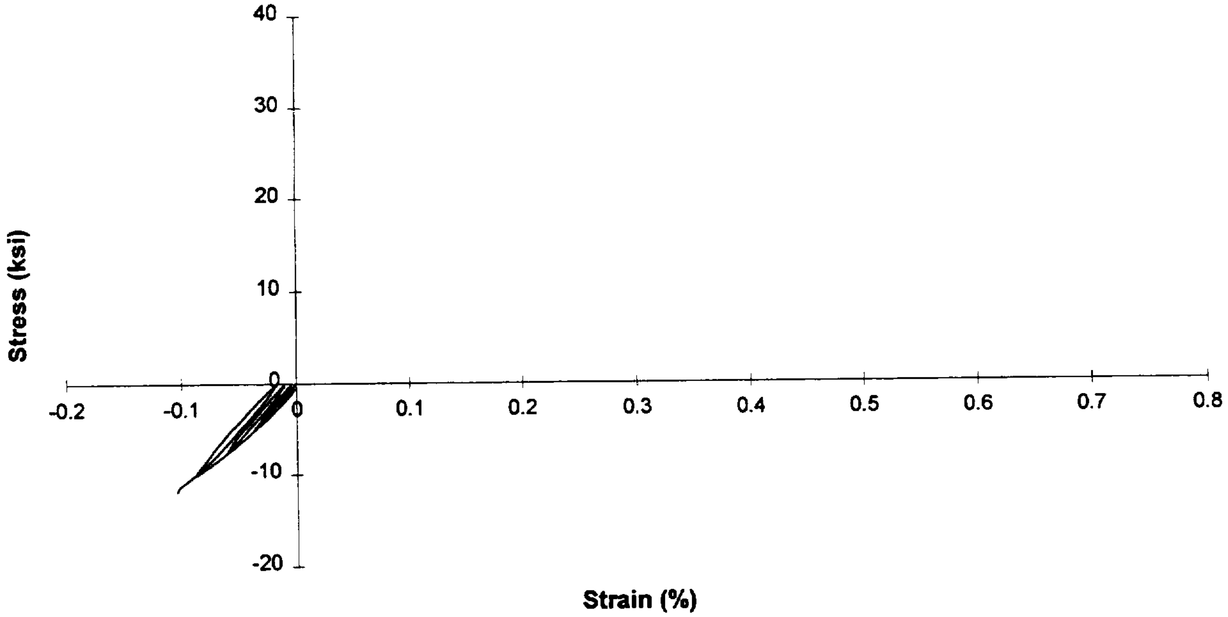

Figure 3.4(b). Typical cyclic compression curve for 0° C/Cu-Ti.

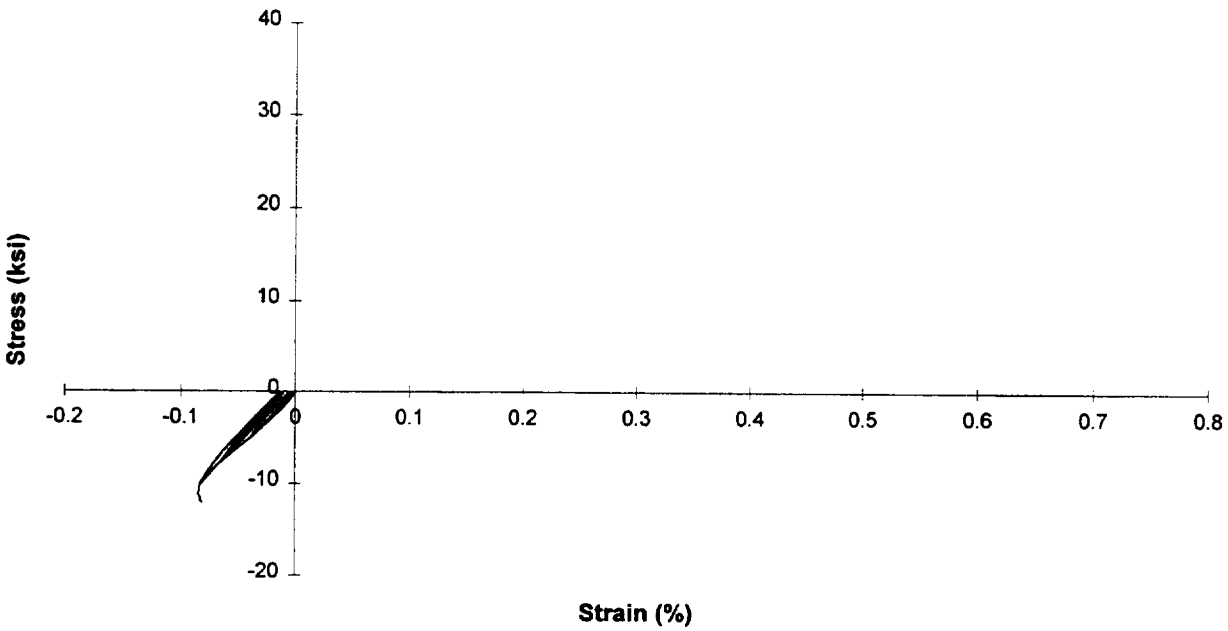

Figure 3.4(c). Typical cyclic compression curve for 0° C/Cu.

The envelopes of the cyclic compressive stress-strain curves in Figures 3.4(a), (b), and (c) show that the trend based on matrix alloy type is similar to that for monotonic compression for the 0° specimens. The apparent difference in the amount of hysteresis between the 0° C/Cu-Cr compressive curve and the compressive curves shown in Figures 3.4(b) and (c) is due to the fact that the 0° C/Cu-Cr specimen survived to be unloaded from -12.5 ksi. The 0° C/Cu-Ti specimen and the 0° C/Cu specimen both failed before the compressive stress reached this level. Hence, the 0° C/Cu-Cr compressive curve has an additional cycle, which resulted in a larger amount of hysteresis. The amount of hysteresis present in the first four cycles for each matrix alloy type was similar.

Figure 3.5 shows typical cyclic tension curves for 90° C/Cu-alloy specimens. Little can be deduced from the 90° C/Cu-Ti curve because the specimen slipped in the grips prior to failure. However, the trend in the envelopes of the curves based on matrix alloy type is similar to that observed for the monotonic specimens (see Figure 3.3(b)). During unloading, the 90° C/Cu specimen exhibited more hysteresis than the 90° C/Cu-Cr specimen. This may be due in part to the fact that during unloading, compressive yielding is occurring. As was shown in Figure 3.3(a), C/Cu yields at a lower compressive stress than does C/Cu-Cr. This leads to a larger

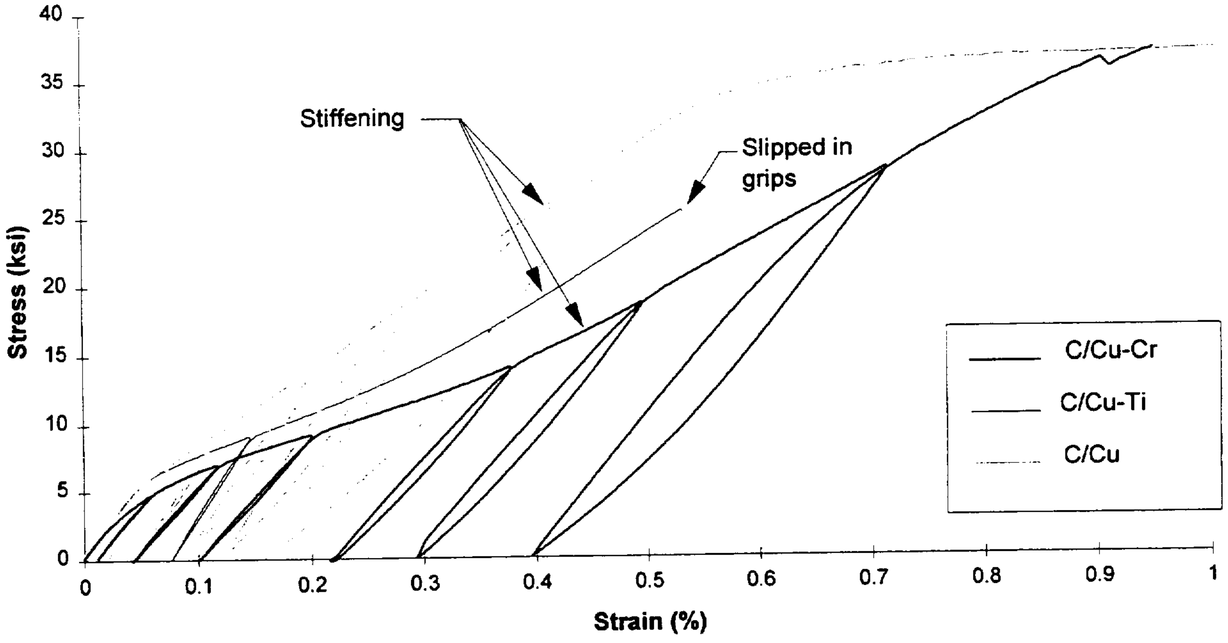

Figure 3.5. Typical cyclic tension curves for 90° C/Cu-alloy specimens.

hysteresis loop for C/Cu since, upon unloading, compressive yielding occurs sooner than it does for C/Cu-Cr. The poorly bonded C/Cu composite may also be affected to a larger extent by frictional effects than the C/Cu-Cr. This too would result in a larger hysteresis loop for C/Cu, as is observed in Figure 3.5.

One might argue that the hysteresis loops in Figure 3.5 are caused by damage to the composite rather than compressive yielding (which implies kinematic hardening) or frictional effects. However, damage can be ruled out as a significant hysteretic mechanism by examining the unloading and reloading elastic moduli for each cycle in a cyclic tension test. Figure 3.6 is a plot of the unloading and reloading moduli as a function of the maximum stress for each cycle in a typical cyclic tension test. The loading and unloading moduli remain nearly constant throughout the cyclic loading. If damage were an important mechanism leading to the hysteretic behavior, a significant decrease in the elastic modulus would be expected as the specimen was loaded. Since this did not occur, it can be concluded that the hysteretic behavior of C/Cu-alloy composites is not due to damage. The hysteretic behavior exhibited by the composite is probably due to movement of the yield surface associated with kinematic hardening and frictional effects

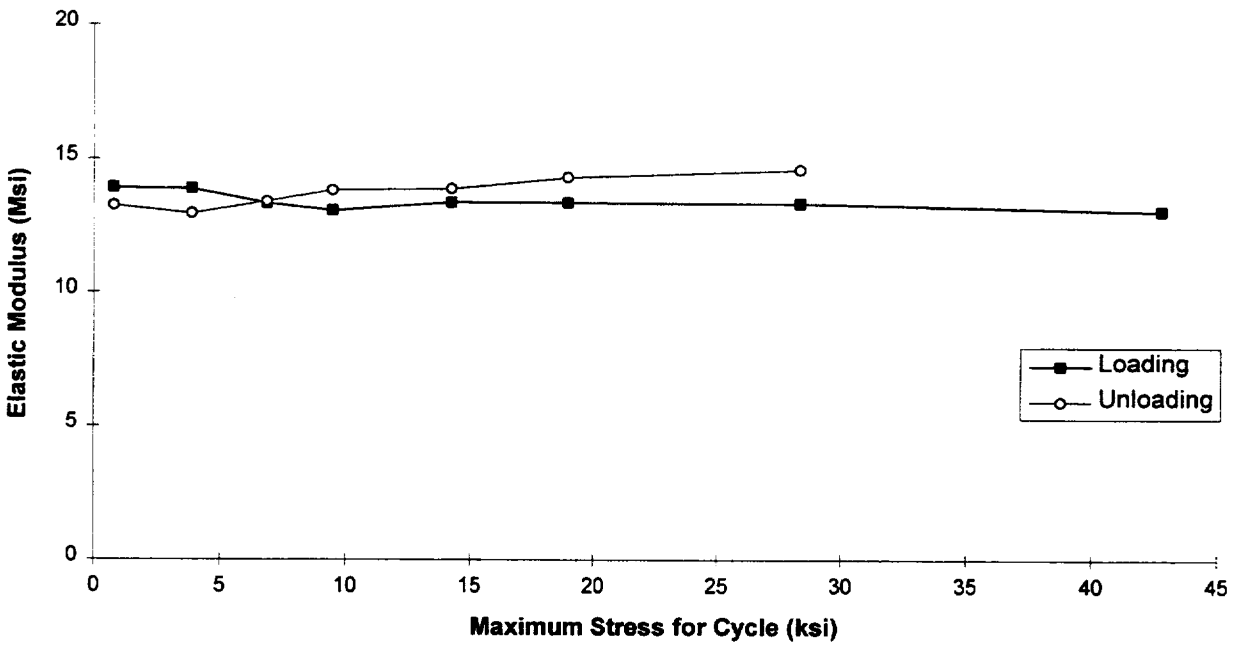

Figure 3.6. Loading and unloading elastic moduli during cyclic tension (C/Cu specimen).

caused by poorly bonded fiber-matrix interfaces. Kinematic hardening results in translation of the yield surface as the composite is loaded in tension. Then, upon unloading, the compressive yield stress of the composite is reached while the average stress on the composite remains tensile. Frictional sliding at the fiber-matrix interface is a dissipative process which would not initially lower the composite modulus upon reloading but would result in hysteresis loops.

3.1.3 Combined Tension-Compression

Figures 3.7(a) and 3.7(b) show combined tension-compression (T-C) and combined compression-tension (C-T) test results, respectively. The curves in the figures represent tests performed on 0° C/Cu-Cr specimens, but the qualitative appearance of the combined test curves did not vary significantly based on matrix alloy type.

The specimens failed in compression rather than tension in both the T-C and C-T tests. This is because the strength of the composite is much lower in compression due to the micro-buckling failure mechanism (see Figures 3.1 and 3.3(a)). Another interesting similarity for both tests is the fact that in tension, the curve for subsequent cycles passed through the maximum

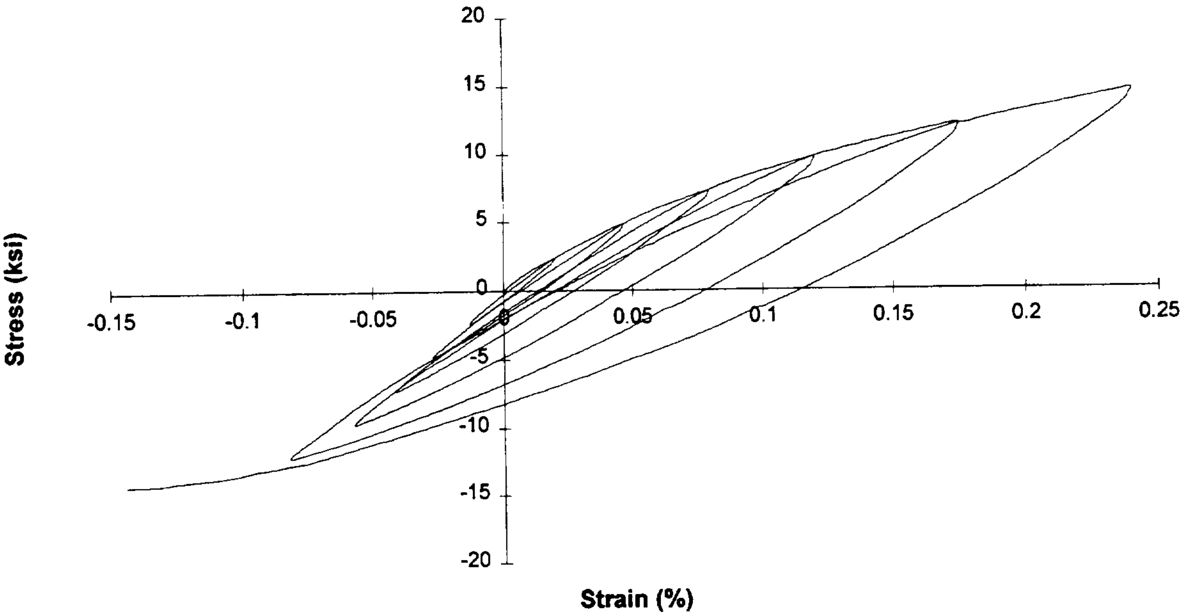

Figure 3.7(a). Typical combined tension-compression test results.

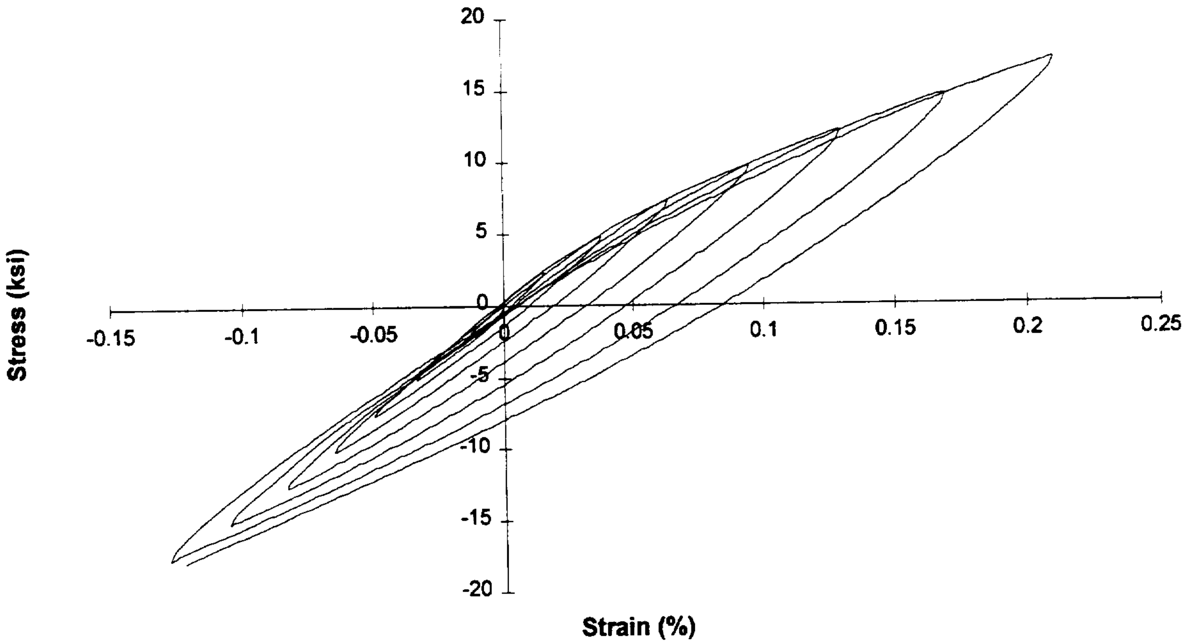

Figure 3.7(b). Typical combined compression-tension test results.

stress reached in the previous cycle. This is not the case in compression. In addition, while a significant amount of permanent tensile strain is present in each cycle after tensile unloading, no permanent compressive strain remains after compressive unloading. These observations indicate a major difference between the stress and strain distributions within the composite in tension and compression. The distinctions are probably due to the fact that, for a given stress magnitude, a larger amount of strain occurs in tension compared to compression. To further understand these distinctions, micromechanical modeling of the cyclic response of the composite would be required.

Comparison of Figures 3.7(a) and (b) indicates that more permanent strain is present upon tensile unloading in the T-C test than the C-T test. This can be observed by comparing the points at which the stress-strain curves cross the positive strain axis for each cycle in the two figures. This is probably caused by the differences in plastic flow and hardening between the tensile and compressive regimes. In the T-C test, each progressively higher stress magnitude is reached first in tension. As observed in Figures 3.1 and 3.3, more plastic flow, and thus more kinematic hardening, occurs in tension compared to compression. Hence, in the T-C test the yield surface is translated in the tensile direction first. Then, upon compressive loading, less plastic flow occurs and the yield surface does not translate as far in the compressive direction. In the C-T test, each progressively higher stress magnitude is reached first in compression. Thus the yield surface has not been moved so far in the tensile direction each time the specimen is placed in compression, so a higher compressive stress can be reached before yielding commences. In addition, compression has a "head start" over tension in the C-T tests to move the yield surface in the compressive direction first for each loading cycle.

The movement of the yield surface in the T-C and C-T tests can be examined in more detail using a newly developed "bedpin" diagram. The diagram consists of the loading path plotted on stress versus cycle number axes. The tensile and compressive yield stresses for the cycle (based on a 0.1% stress-strain departure from linearity, in this case) are also plotted. The bedpin diagram thus gives a clear indication of the yield surface progression throughout the cyclic loading history. The horizontal distance along the loading path from the previous maximum stress magnitude to the yield stress for each cycle is a measure of the yield surface size. The location of these stresses, with respect to the stress axis, corresponds to the position of the points of the yield surface that intersect the primary stress axis in the loading direction.

The bedpin diagrams for typical T-C and C-T tests on C/Cu-alloy specimens are given in Figures 3.8(a) and (b). In Figure 3.8(a), yielding first occurs in tension at 4.55 ksi during the third cycle. From this point until the loading reverses, the material hardens in tension. The loading reverses at 4.86 ksi, and compressive loading (tensile unloading) commences. At this point, loading is occurring inside the specimen's yield surface. At -3.47 ksi, compressive yielding occurs. Clearly, the line connecting this compressive yield point at -3.47 ksi and the previous maximum stress, 4.86 ksi, is a measure of the yield surface size and position (along the loading direction principal stress axis). The yield surface is 8.33 ksi wide, and centered at 0.695 ksi. Of course, as the material is cycled further, these quantities change. The material deforms plastically as compressive loading continues until -4.83 ksi. Then, tensile loading commences, and tensile yield occurs at 3.67 ksi. Now the yield surface is 8.50 ksi wide and centered at -0.58 ksi. The size of the yield surface has grown slightly, but it has translated considerably. This is kinematic hardening as opposed to isotropic hardening. As cyclic loading continues, it is easy to see that the yield surface continues to translate in response to each successive tensile and compressive loading, but it does not become substantially larger. Thus, it appears that for C/Cu-alloy composites, the hardening behavior is predominantly kinematic as opposed to isotropic.

The bedpin diagram for the C-T test (Figure 3.8(b)) is similar (in form) to that of the T-C test. Again, it is clear that kinematic hardening dominates. In addition, it is clear from the loading path shown in the figure that in the C-T test, each successive maximum stress magnitude occurs first in compression rather than tension (as was the case in the T-C test). As discussed previously, there is a major difference between the tensile and compressive stress and strain distributions in the composite. This difference, and its effect on the cyclic hardening behavior, accounts for the difference in the appearances of Figures 3.7(a) and 3.7(b).

3.2 Iosipescu Shear Tests

3.2.1 Monotonic Shear Tests

Typical monotonic shear stress-strain curves for the 0° C/Cu-alloy Iosipescu specimens are presented in Figure 3.9(a). Figure 3.9(b) shows typical monotonic shear stress-strain curves

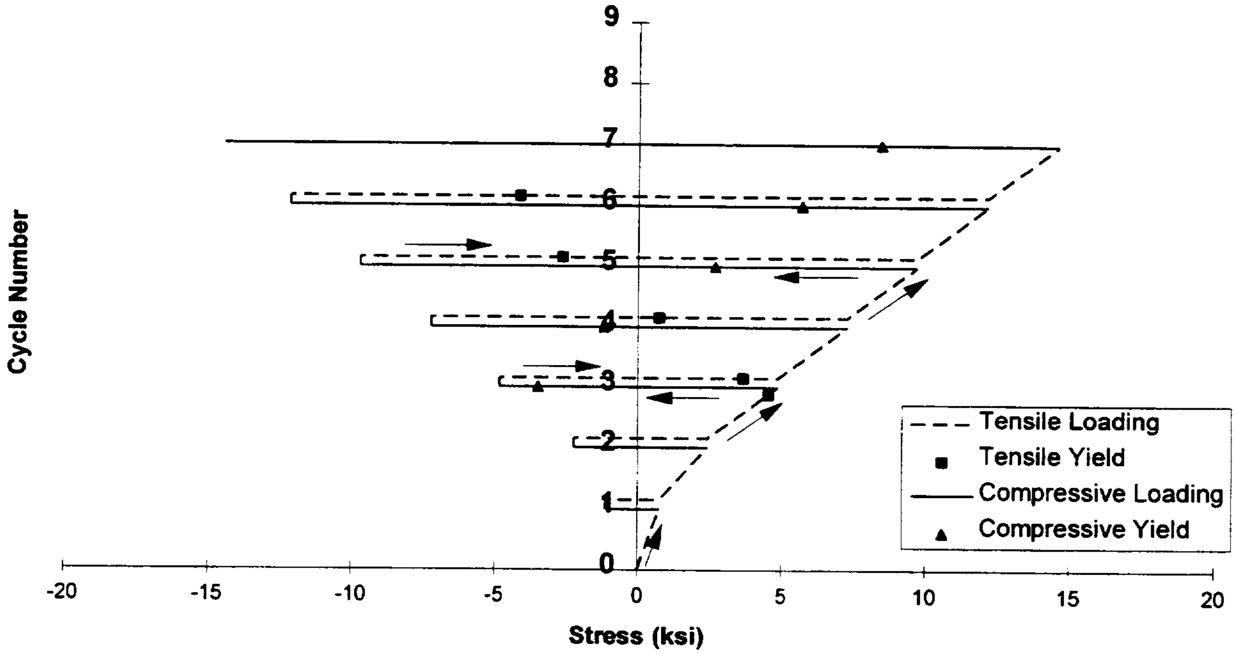

Figure 3.8(a). Bedpin diagram for a typical T-C test on a C/Cu-alloy specimen.

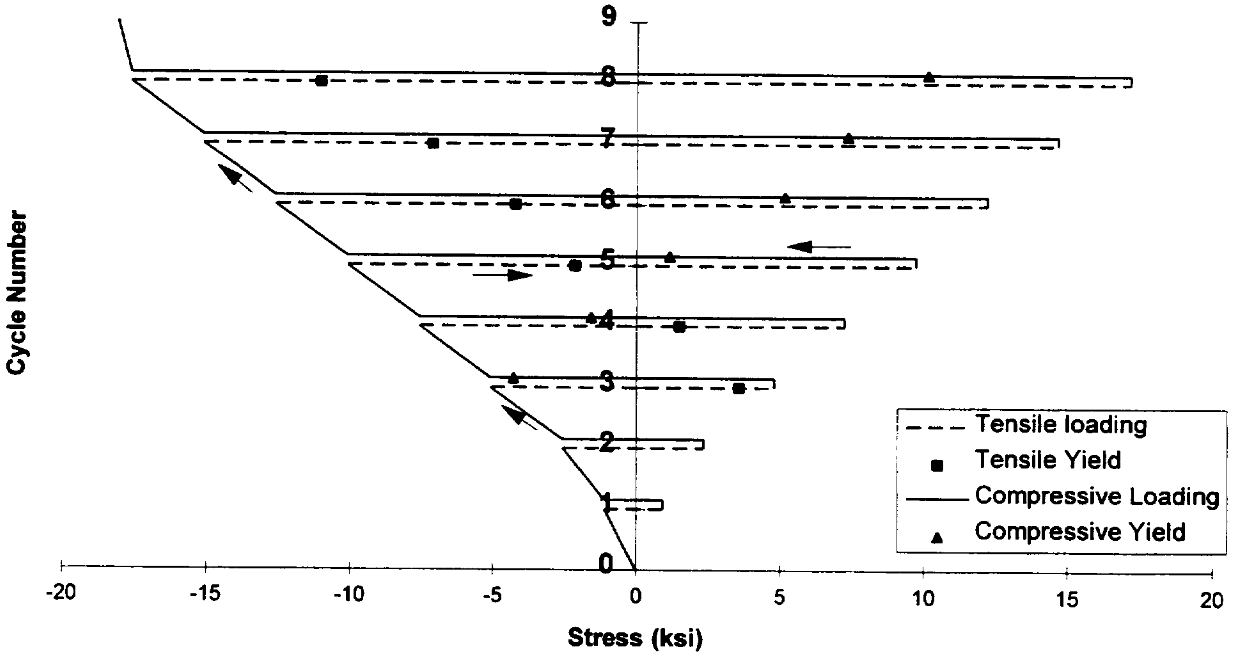

Figure 3.8(b). Bedpin diagram for a typical C-T test on a C/Cu-alloy specimen.

for the 90° C/Cu-alloy Iosipescu specimens. In general, the shear response of C/Cu-alloy composites is typified by early yielding, compliant hardening behavior, a great deal of permanent strain prior to "failure", and "failure" at a low shear stress. The low post-yield slope of the shear stress-strain curves, as compared to the tensile stress-strain curves, is typical of continuous fiber-reinforced composites. This is due to the fact that in shear, the fibers and matrix share the load to a greater degree than in tension, and thus the strain in the matrix is much higher. For this reason, the post-yield behavior in shear is dominated by the matrix.

The term "failure" is used loosely with regard to the shear tests, because in fact, the specimens were not tested until some distinct failure event occurred. The Iosipescu shear tests were performed in displacement control, thus an instability leading to fracture of the specimen could not be achieved. Rather, a great deal of fiber yarn movement, coupled with large-scale matrix deformation and some matrix cracking, occurred in the gauge section of the typical specimen. Tested specimens also showed local evidence of micro-buckling of the weave layers, similar to the specimens failed in compression. As the specimen shear strain became large, the load did not drop but stayed constant, resulting in the "flat" appearance of most shear stress-strain curves. The test was stopped when contact of certain components of the Iosipescu fixture was imminent. Hence, the shear stress at the point where the test was stopped does represent a "failure" stress for the specimen, since this is the maximum shear stress that the specimen could support. Imposing a larger stress at this point would have caused fracture. An accurate shear strain to failure, however, could not be determined.

Examining Figures 3.9(a) and (b), the matrix alloy type clearly has a major effect on the shear response of C/Cu-alloy composites. The specimens exhibited similar shear behavior in the elastic range regardless of weave orientation and matrix type. However, the stress-strain curves diverge significantly once inelastic deformation begins to occur. For the 0° weave orientation, the C/Cu specimen yielded first, followed by the C/Cu-Ti specimen, and finally the C/Cu-Cr specimen. In addition to occurring at a higher stress, yielding in the 0° C/Cu-Cr specimen occurred more gradually than the other specimens. Therefore, the 0° C/Cu-Cr specimen has the highest ultimate shear strength as well, followed by the 0° C/Cu-Ti specimen, and finally the C/Cu specimen. For the 90° weave orientation, the above trends in yield stress and ultimate shear strength are also evident. However, the small difference in the shear response of the 90°

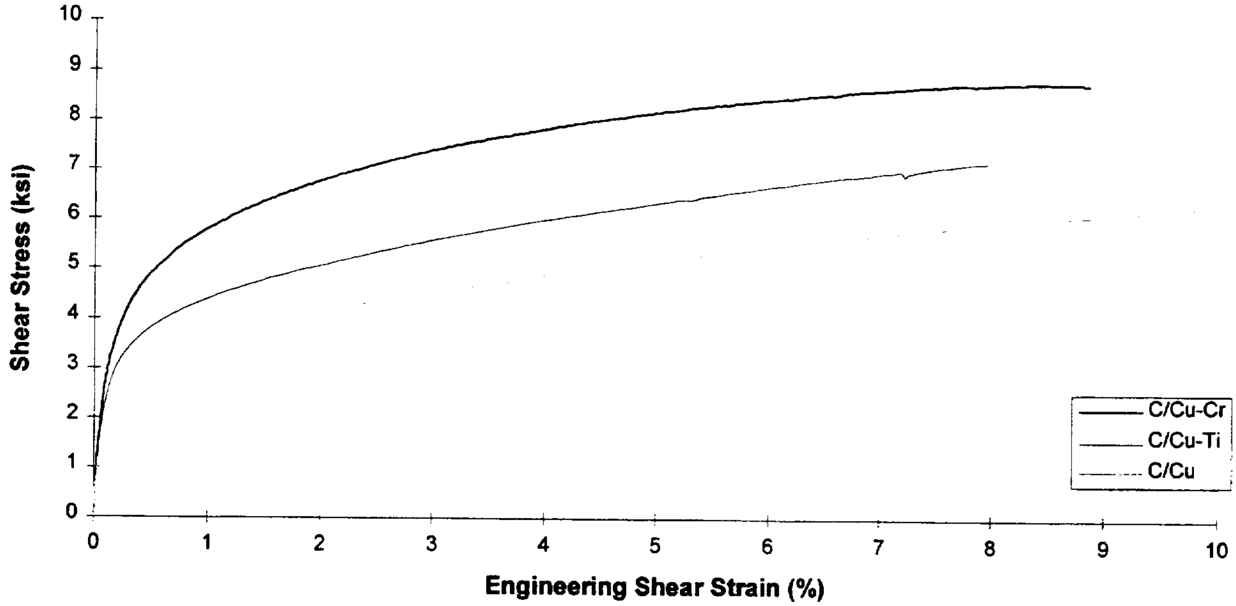

Figure 3.9(a). Typical monotonic shear stress-strain curves for 0° C/Cu-alloy specimens.

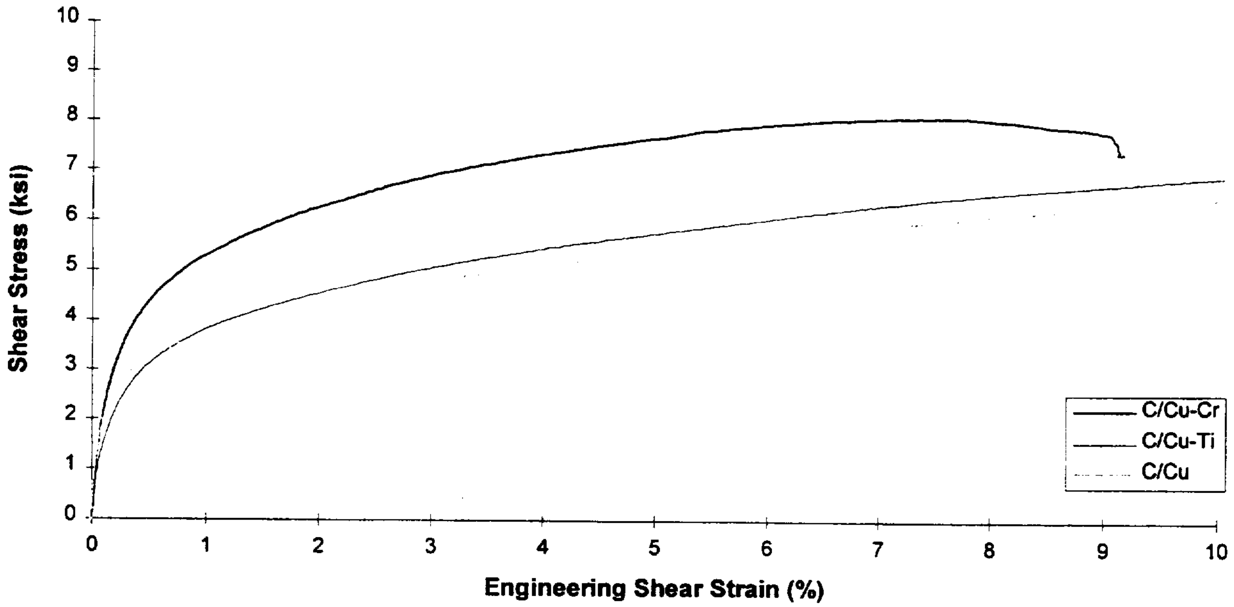

Figure 3.9(b). Typical monotonic shear stress-strain curves for 90° C/Cu-alloy specimens.

C/Cu-Ti specimen and the 90° C/Cu specimen is probably insignificant due to scatter in the results within specimens of identical weave orientation and matrix alloy. Figure 3.10 shows the amount of scatter within a specimen type that was typically observed in the Iosipescu shear tests. It should be noted that shear strains were necessarily measured with a 3 mm strain gauge rosette (due to the size of the Iosipescu specimen gauge section), thus a significant amount of scatter is expected due to the large repeating unit cell of the reinforcement weave (see Figure 2.6).

The trends apparent in Figures 3.9(a) and (b) with respect to matrix alloy type provide further insight into the fiber-matrix bonding in C/Cu-alloy composites. If, once again, the 8-harness satin C/Cu composite is thought of as a "traditional" $[0°/90°]_s$ laminate (as discussed in Section 3.1.1) one would expect the observed trends. Poor bonding (as in the C/Cu composite) would cause the fibers to behave like holes, reducing the overall stiffness of the composite. However, the question remains as to why this $[0°/90°]_s$ poor bonding argument is valid in the case of shear while it is not valid for tension. The cross-over regions are still important in shear, and closure of the fiber-matrix interface does not occur, yet the observed trend is opposite to that expected based on the cross-over region stress concentration argument. The observed trend can

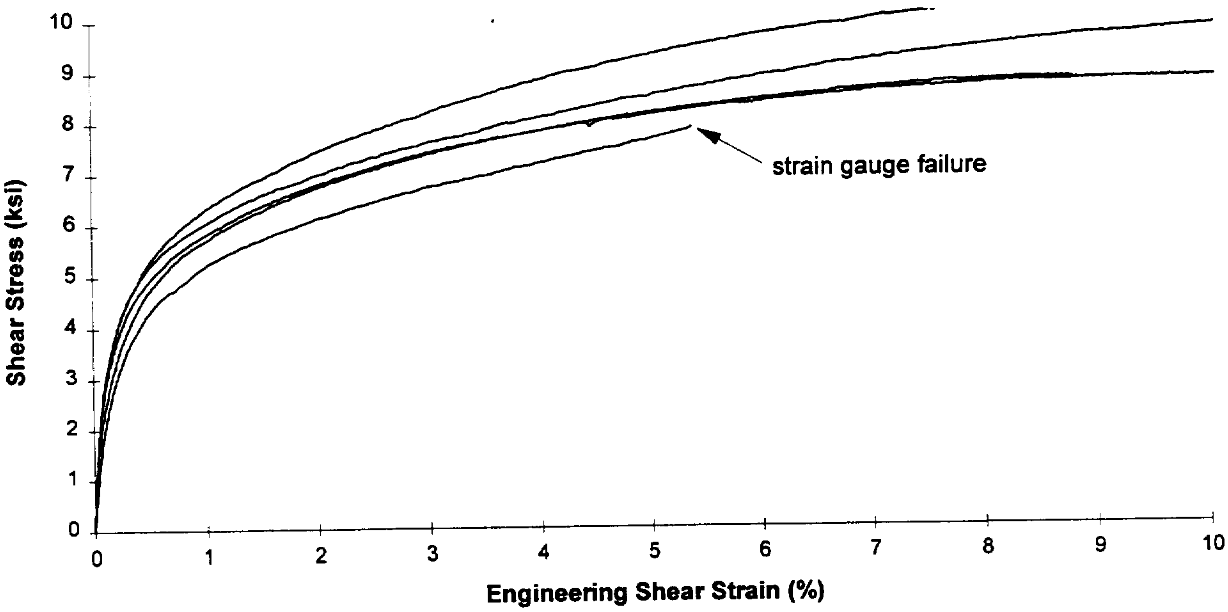

Figure 3.10. Typical scatter in experimental shear stress-strain curves within a specimen type.

be explained by the fact that in shear, there is no distinction between 0° and 90° layers. Both layer orientations respond identically to in-plane shear. Thus, a stiff layer cannot compensate for a compliant layer, as was the case in tension. Both layers are subject to the stiffness loss associated with debonding, and the traditional argument based on poor bonding should be valid. Judging from the data in Figures 3.9(a) and (b), this appears to be the case.

Superior fiber-matrix bonding seems to have had the greatest effect on the shear yield stress of the composite. The delay in yielding associated with the bonding, and the fact that the onset of permanent deformation was more gradual for the C/Cu-Cr specimen as compared to the C/Cu-Ti and C/Cu specimens, is directly responsible for the higher ultimate strength of the C/Cu-Cr specimen. Once the transition from elastic behavior is complete ($\gamma > 0.2\%$), the post-yield behavior of the specimens is quite similar. In fact, the post-yield slopes of the C/Cu-Ti and C/Cu shear specimens are slightly greater than that of the C/Cu-Cr shear specimens. Hence, it is the superior elastic and transition behavior ($\gamma < 0.2\%$) of the C/Cu-Cr specimens that is responsible for their superior shear strengths. The lower post-yield slope of the superior bonded C/Cu-Cr composite was also observed in tension.

Differences between the shear responses of 0° and 90° weave orientation specimens within a matrix alloy type are reasonably small. The extent of any weave orientation effect is certainly masked to some degree by the experimental scatter. Direct comparison of all monotonic shear stress-strain curves for each alloy type reveals that for C/Cu-Cr and C/Cu-Ti, the curves for the 0° specimens are slightly higher (i.e. stiffer overall response) than the curves for the 90° specimens. For the C/Cu specimens, the stress-strain curves for the 90° specimens are higher than those of the 0° specimens. Again, it must be emphasized that, due to the experimental scatter, these observations are tentative. Furthermore, since the woven preform is expected to be nearly identical in the 0° and 90° directions, and micrographs of the woven C/Cu composite appear identical in the two directions, the cause of the weave orientation effect cannot, at present, be determined.

3.2.2 Cyclic Shear

A typical cyclic shear stress-strain curve is shown in Figure 3.11. Comparing the response of specimens with different matrix alloys and weave orientations subjected to cyclic

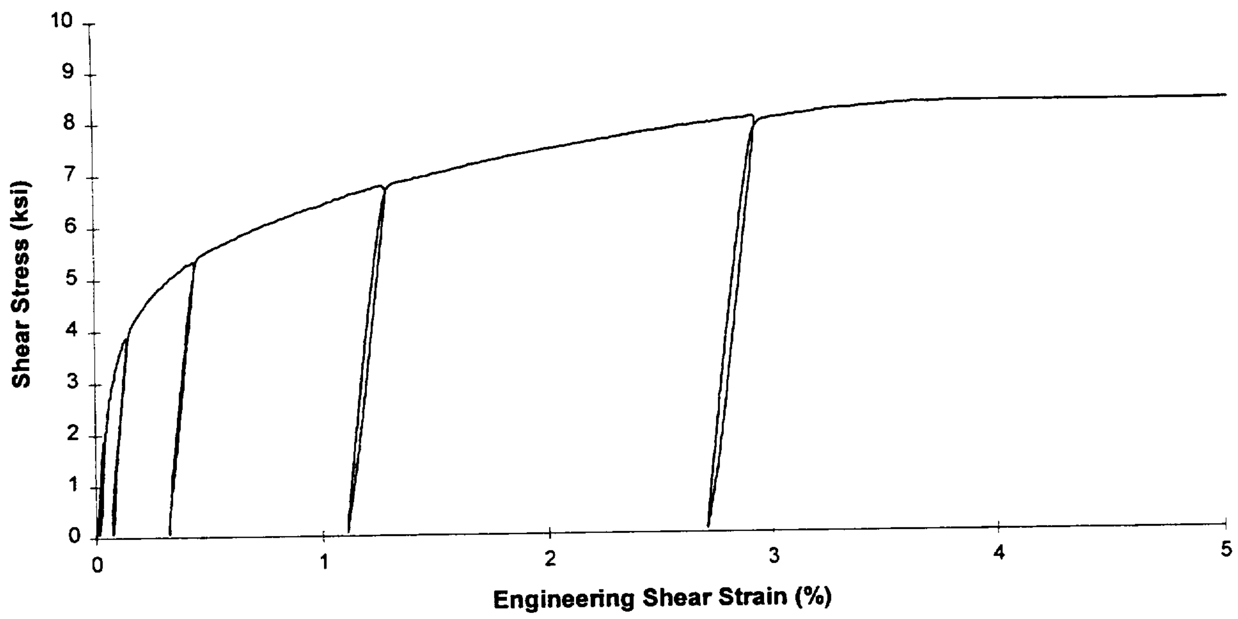

Figure 3.11. Typical cyclic Iosipescu shear response of C/Cu-alloy specimens.

shear loading reveals little additional information to what was gleaned from the monotonic response. Significant observations from the cyclic shear tests involve the hysteretic behavior. Upon unloading, the material does not yield significantly. Upon reloading, the stress-strain curve follows the unloading curve quite closely and bends over abruptly (due to yielding) once the maximum stress from the previous loading cycle is reached. This small hysteretic behavior indicates that the hardening that occurs in shear is mainly due to expansion of the yield surface (isotropic hardening) as opposed to the kinematic hardening observed in tension. Since the post-yield shear response of woven C/Cu is dominated by the matrix while the post-yield tensile response is influenced significantly by the reinforcement weave, it can be concluded that the large amount of kinematic hardening in tension is due to the presence of the reinforcement weave and the microstructural interaction between the weave and the matrix.

3.3 Summary of Experimental Results

3.3.1 Initial Modulus

Figure 3.12 provides a summary of the average initial tensile (T), compressive (C), and shear (S) modulus data for all tests (monotonic and cyclic). The chart is divided by test type, matrix alloy type, and weave orientation. The moduli of pure copper are included for comparison. The initial modulus was taken as the average slope of the stress-strain curve from the first 1 ksi of loading. Recall that five cycles to a stress level of 1 ksi were used to seat the strain gauges in all tests. Error bars in Figure 3.12 denote the high and low values for each specimen type. The large error bars in the figure indicate that the initial modulus results contain a significant amount of scatter, thus conclusions drawn from this data must be treated as tentative.

For each 0° C/Cu-alloy composite, Figure 3.12 indicates that the initial compressive modulus is greater than the initial tensile modulus. This is probably an artifact of the different testing techniques used for tensile and compressive tests. As discussed in Section 2.3, tensile testing was performed on small dog-boned specimens, while compressive testing was performed on larger rectangular (T-C) specimens. The T-C specimens were 4 in. x 1 in., and 2 in. of the specimen length was used for gripping. Thus, the gauge section had an aspect ratio of only 2, which is probably insufficiently large to neglect end constraint effects. Constraint effects due the grips tend to prevent the gauge section from expanding or contracting laterally during axial compressive or tensile loading. This transverse constraint then constrains the deformation in the loading direction. Hence, a stiffer apparent response for T-C specimens compared to the tensile specimens results.

Further evidence of the misleading nature of the difference between the tensile and compressive initial moduli is given in Figure 3.13. This figure shows a detail of the early loading cycles from a typical tension-compression test stress-strain curve. Clearly, when the state of stress changes from tensile to compressive, or vice versa, the slope of the stress-strain curve does not change. If the material were actually stiffer in compression, as Figure 3.12 would lead one to believe, a noticeable change in the slope of the stress-strain curve would be expected.

Figure 3.12 indicates that for the C/Cu-Cr specimens, the average tensile moduli of specimens with both weave orientations are nearly identical. The average tensile moduli of the 90° C/Cu-Ti and 90° C/Cu specimens are greater than the average tensile moduli for the 0° C/Cu- Ti and 0° C/Cu specimens. However, comparing the differences to the size of the error bars indicates that the differences are probably not significant with respect to scatter within a

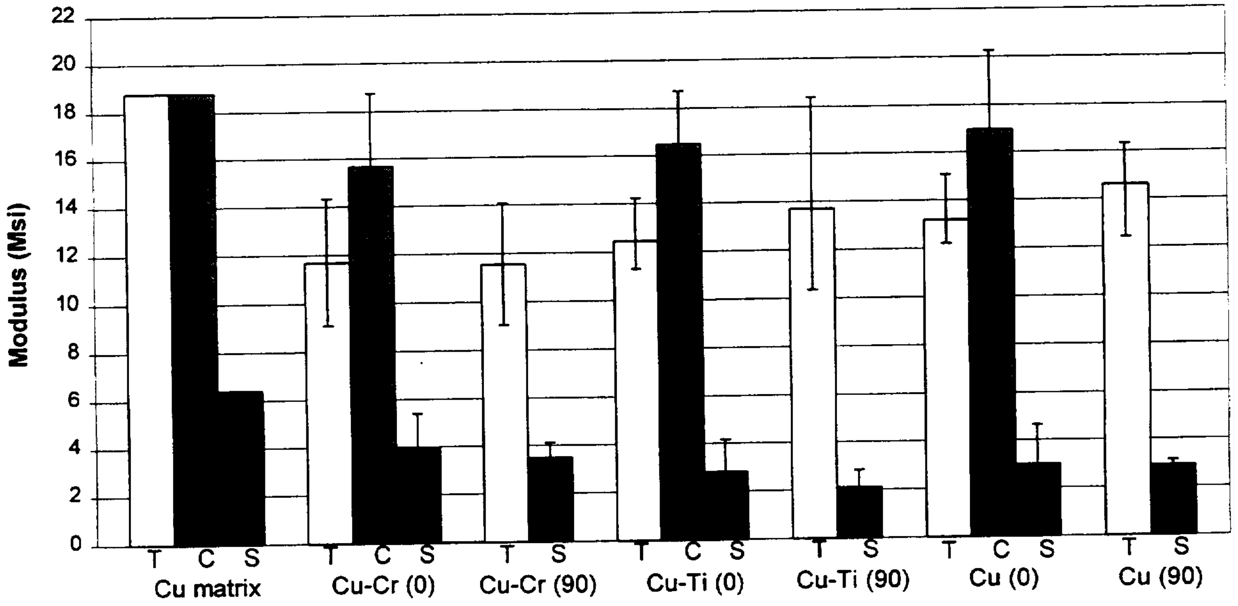

Figure 3.12. Summary of initial modulus results for 0° and 90° C/Cu-alloy tension (T), compression (C), and shear (S) tests. Error bars indicate high and low values.

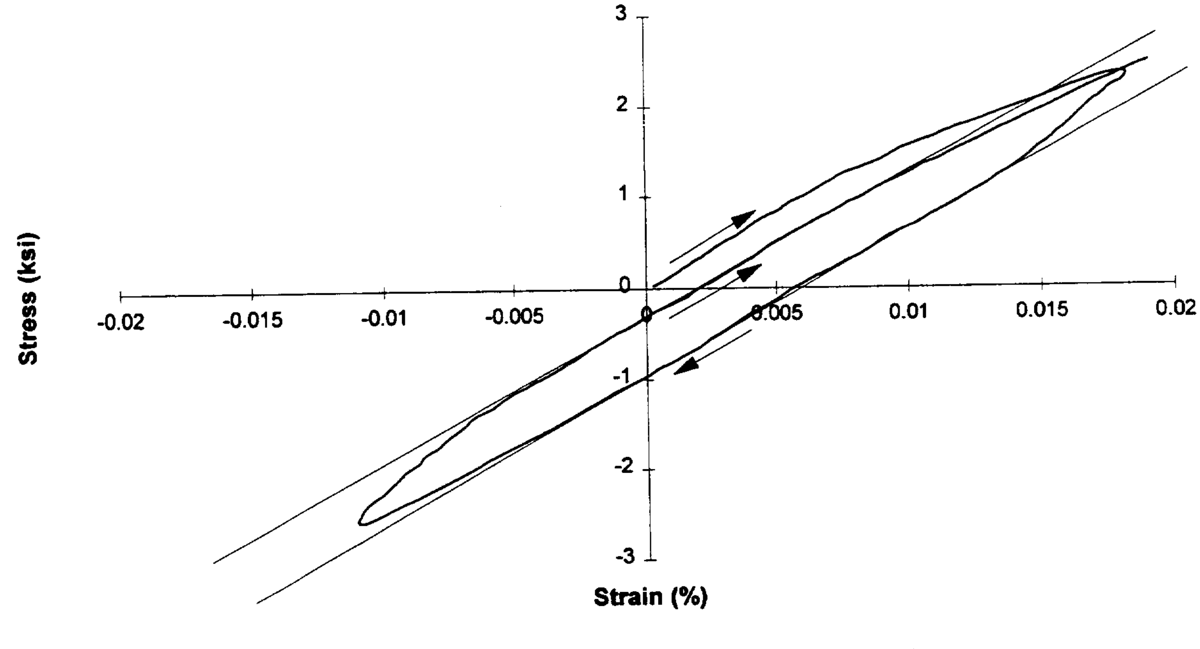

Figure 3.13. Detail of typical tension-compression test stress-strain curve showing that the slope of the curve does not change as the state of stress reverses.

weave orientation. Examining the effect of the weave orientation on the average shear moduli reveals that the average value is greater for the 0° orientation for all three C/Cu-alloy composites. However, the scatter again calls this conclusion into question.

Examining the effect of the matrix alloy type on the average moduli reveals that the C/Cu specimens had the highest tensile and compressive modulus, followed by the C/Cu-Ti specimens, and finally the C/Cu-Cr specimens. Although scatter in the results makes the observations tentative, the observed trend in the tensile moduli agrees with the discussion on interfacial bonding given in Section 3.1.1. Recall that the trend, in order of decreasing interfacial bond effectiveness, is C/Cu-Cr, C/Cu-Ti, C/Cu. Thus, the trend for tensile modulus is the same as the trend observed for the tensile stress-strain curves (see Figures 3.3(a) and (b)). This trend is opposite that expected considering the traditional argument based on poor bonding. As discussed earlier, a possible explanation for the observed trend is the influence of stress concentrations in yarn cross-over regions. Greater transfer of stress from the fiber to the matrix via shear in the well bonded composite could result in more elastic deformation and a more compliant elastic response.

The trend in compressive moduli shown in Figure 3.12 is opposite to the trend in the compressive stress-strain curves shown in Figure 3.3(a). Considering the overall compressive response, Figure 3.3(a) indicates that C/Cu-Cr is the stiffest, followed by C/Cu-Ti, and finally by C/Cu. The trend observed in this figure was explained in Section 3.1.1 by considering yarn cross-over regions as weak links in which compressive deformation is restricted by superior fiber-matrix bonding. If the trend in compressive moduli shown in Figure 3.12 is credible, it is clear that the argument for the compressive data given in Section 3.1.1 is valid only once yielding in the composite occurs. In order to completely explain the observed trend in compressive moduli based on matrix alloy type, a model which include fiber-matrix debonding would be required.

The shear modulus was highest for the C/Cu-Cr composites, followed by C/Cu, and finally C/Cu-Ti. This trend does not follow one based on interfacial bonding (since C/Cu and C/Cu-Ti are reversed), but the high shear modulus of C/Cu-Cr would be expected based on the traditional interfacial bonding argument, as discussed in Section 3.2.1. Once again, however, the

Table 3.1. Comparison of moduli for Cu and C/Cu.

Modulus	Copper	8-Harness Satin C/Cu
Tensile (Msi)	18.8	12.9
Compressive (Msi)	18.8	16.4
Shear (Msi)	6.4	3.0

Table 3.2. Comparison of specific moduli for Cu and C/Cu.

Specific Modulus	Copper	8-Harness Satin C/Cu
Tensile (in. $\times 10^9$)	58.3	59.5
Compressive (in. $\times 10^9$)	58.3	75.7
Shear (in. $\times 10^9$)	19.9	13.8

large amount of scatter and the need for a model of the bonding limits the conclusions that can be drawn from these observations.

Comparing the moduli of the C/Cu-alloy composites to the moduli of pure copper, it is clear that pure copper provides a higher modulus in all cases. Table 3.1 provides a numerical comparison of the moduli of copper to the average moduli of all C/Cu-alloy specimens. However, if the *specific* moduli (modulus divided by density) are compared, the C/Cu-alloy composite fares much better. Table 3.2 provides a comparison of the specific moduli for copper and C/Cu (based on a fiber volume fraction of 43%).

3.3.2 Yield Stress

Figure 3.14 provides a summary of the average tensile (T), compressive (C), and shear (S) yield stress data for all monotonic tests. Yield stress values from cyclic shear tests were also included when calculating the average shear yield stress since, typically, yielding in shear occurred during the first loading cycle. The yield stress was determined by first calculating an elastic strain for each data point based on the stress level and initial modulus for the specimen. The elastic strain for each data point was then compared to the measured strain for that data point, and the yield stress was taken as the stress at the data point where the difference between

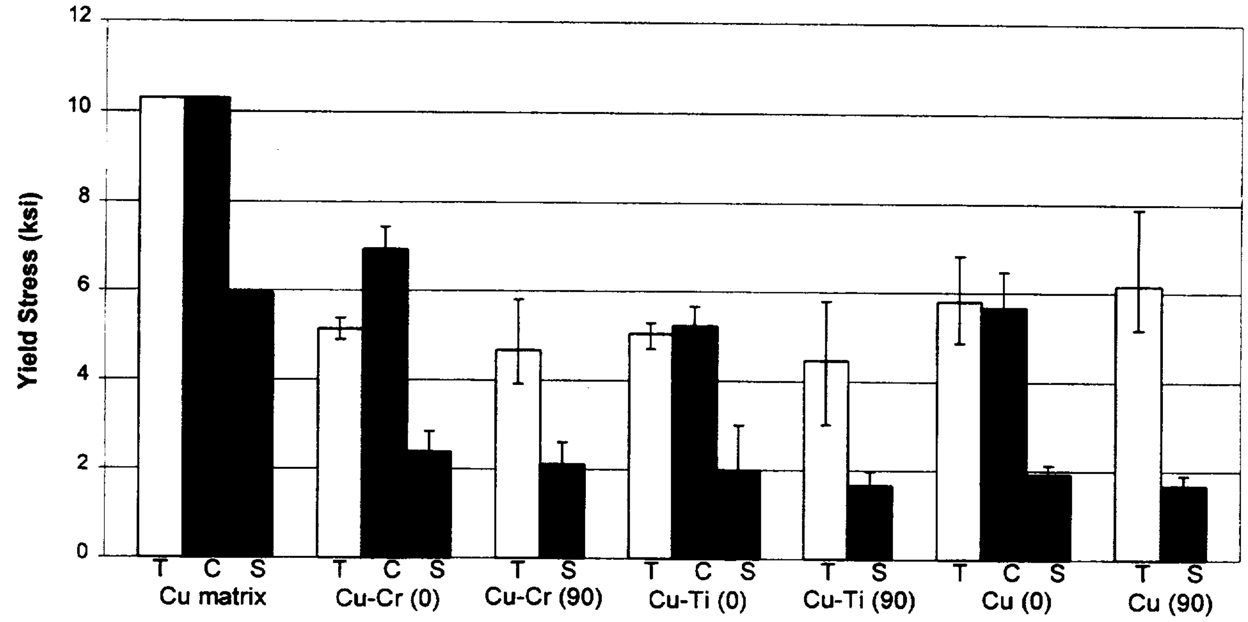

Figure 3.14. Summary of yield stress results for 0° and 90° C/Cu-alloy tension (T), compression (C), and shear (S) tests. Error bars indicate high and low values.

the measured strain and the elastic strain first met or exceeded 0.1 %. The amount of scatter in the yield stress data is slightly less than that in the initial modulus data, but the amount is still significant.

For 0° C/Cu-Cr, the average yield stress in compression is significantly higher than that in tension. For 0° C/Cu-Ti and 0° C/Cu, the average yield stress in tension and compression are nearly the same. Thus it appears that the effects of residual stresses and the grip constraint on yielding are greater when superior fiber-matrix bonding exists.

The effect of the weave orientation on the average tensile yield stress is not consistent. For C/Cu-Cr and C/Cu-Ti, the average tensile yield stress is higher for the 0° orientation, while for C/Cu, it is higher for the 90° orientation. The average shear yield stress is higher for the 0° orientation than the 90° orientation for all three matrix alloy types. However, once again the differences based on weave orientation are reasonably small compared to the scatter in the results. Thus, whether or not a significant difference between the two weave orientations exists cannot be conclusively determined from this data.

The effect of the matrix alloy type on the average yield stress is also not entirely clear. In tension, it is clear that the C/Cu specimens exhibited the highest yield stress, while the C/Cu-Cr and C/Cu-Ti specimens averaged similar yield stresses. As was the case with the moduli, traditional interfacial bonding arguments would suggest the opposite trend, with C/Cu having the lowest yield stress due to the poor fiber-matrix bonding. Thus, the argument based on stress concentrations in yarn cross-over regions, as described in Section 3.1.1, is supported. This mechanism is particularly applicable to yield stress since high local stress concentrations would be expected to lower the macroscopic yield stress. To determine conclusively if this argument is valid, a micromechanics model, like the one mentioned previously, would be required.

In compression, the C/Cu-Cr specimens exhibited the highest average yield stress, while the values for the C/Cu-Ti and C/Cu specimens were reasonably close. In shear, the same trend in yield stress (based on matrix alloy type) as in compression is present. The fact that C/Cu-Cr exhibits the highest yield stress in both compression and shear substantiates the explanation given in Section 3.1.1. However, the experimental scatter may be masking some of the true effects of the matrix alloys and interfacial bonding, making it impossible to discern differences between C/Cu-Ti and C/Cu.

Comparing the yield stresses of the composite to that of pure copper in Figure 3.14 reveals that pure copper exhibits higher tensile, compressive, and shear yield stresses. Table 3.3 presents a numerical comparison of these yield stresses for copper with the average yield stresses for all C/Cu-alloy specimens. Table 3.4 presents a similar comparison, except now the specific yield stress (yield stress divided by density) values (based on a fiber volume fraction of 43%) are presented. In the latter chart, it is clear that the composite performs better when the specific yield stresses are compared.

Table 3.3. Comparison of yield stress for Cu and C/Cu.

Yield Stress	Copper	8-Harness Satin C/Cu
Tensile (ksi)	10.3	5.2
Compressive (ksi)	10.3	5.8
Shear (ksi)	6.0	2.0

Table 3.4. Comparison of specific yield stress for Cu and C/Cu.

Specific Yield Stress	Copper	8-Harness Satin C/Cu
Tensile (in. $\times 10^6$)	32.0	24.0
Compressive (in. $\times 10^6$)	32.0	26.8
Shear (in. $\times 10^6$)	18.6	9.2

3.3.3 Ultimate Strength

Figure 3.15 provides a summary of the average tensile (T), compressive (C), and shear (S) ultimate strength data for all tests (monotonic and cyclic). The ultimate strength is simply the highest stress supported by the specimen during the test. For the tension and compression tests, this was typically the stress at failure. For the shear tests, this was the stress corresponding to the "load plateau" described in Section 3.2. The amount of scatter in the tensile and compressive ultimate strength results is similar to that in the tensile and compressive yield stress results. The amount of scatter in the ultimate shear strength results is smaller than that in the shear yield stress and shear modulus results.

For each matrix alloy type, the compressive strength is significantly smaller than the tensile strength because of the micro-buckling failure mechanism in compression. The effect of the weave orientation on the ultimate strength of the composite is once again unclear. The average tensile strength for the 90° orientation was higher for the C/Cu-Cr and C/Cu specimens, while for the C/Cu-Ti specimens, the average tensile strength for the 0° orientation was higher. The average shear strength for the 0° orientation was higher for the C/Cu-Cr and C/Cu-Ti specimens, while for the C/Cu specimens, the average tensile strength for the 90° orientation was higher. Hence, if the weave orientation does have an effect on the ultimate strengths of C/Cu-alloy composites, it is probably being masked by the experimental scatter.

The effect of the matrix alloy type on the average ultimate strength is somewhat clearer. The tensile strength of the C/Cu composite is the highest. This was also shown in Figures 3.3(a) and (b). The average tensile strength of the C/Cu-Cr specimens is lower than the average tensile strength of the C/Cu specimens. This again follows the trend explained in Section 3.1.1. Based on interfacial bonding arguments or arguments based on stress concentrations in yarn cross-over

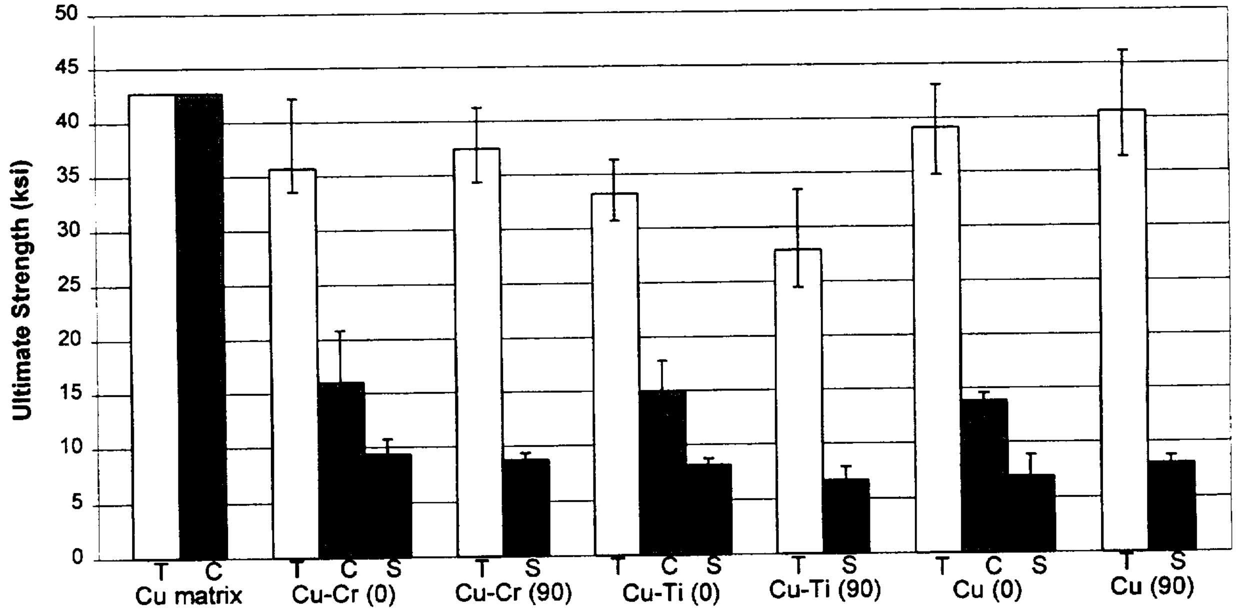

Figure 3.15. Summary of ultimate strength results for 0° and 90° C/Cu-alloy tension (T), compression (C), and shear (S) tests. Error bars indicate high and low values.

regions, one would expect the C/Cu-Ti specimens, with their intermediate degree of fiber-matrix bonding, to have intermediate average ultimate tensile strengths with respect to the C/Cu-Cr and C/Cu specimens. However, the average tensile strengths of the C/Cu-Ti specimens are significantly lower than those of the other C/Cu-alloy specimens. A possible explanation for this can be seen in Figures 3.3(a) and (b). While the C/Cu-Ti tensile specimens typically yielded at a higher stress and exhibited a larger post-yield slope than C/Cu-Cr, they also typically failed at a lower strain. Thus the C/Cu-Cr tensile specimens were able to reach a higher ultimate stress prior to failure. A greater amount of stiffening at the higher strains in the C/Cu-Cr tensile specimens also plays a role in the observed ultimate tensile strengths. It should also be noted that the C/Cu specimens typically failed at lower strains than C/Cu-Cr, but their overall behavior was so much stiffer that C/Cu still exhibited higher average ultimate tensile strengths.

In compression, the average ultimate strengths substantiates the trend shown in Figure 3.3(a) and explained in Section 3.1.1. Namely, that the C/Cu-Cr specimens exhibited the highest average compressive strengths, followed by the C/Cu-Ti specimens, and finally by the C/Cu specimens. The superior fiber-matrix bonding introduced by the alloyed matrices seems to increase the resistance to micro-buckling of the weave layers. The identical trend based on matrix alloy type is present in the average ultimate shear strengths of the 0° specimens, a possible explanation for which was given in Section 3.2.1. For the specimens with reinforcement weaves oriented at 90°, the average ultimate shear strength of C/Cu is higher than that of C/Cu-Ti. This may be due to the experimental scatter which, even for the ultimate shear strength results, is on the order of the differences in the average values for the different specimen types.

Comparing the ultimate strengths of the C/Cu-alloy composites to those of pure copper reveals that the ultimate tensile strength of the composite approaches that of the pure copper. In compression, the composite strength is lower than the bulk (isotropic) copper strength due to the micro-buckling failure mechanism of the composite. A reliable ultimate shear strength for pure copper was not available. A numerical comparison of the copper and average 8-harness satin C/Cu-alloy ultimate strengths is given in Table 3.5. Table 3.6 provides a comparison of the specific strengths (strength divided by density) of copper and the composite (based on a fiber volume fraction of 43%). The specific strengths of the composite compare favorably with those of pure copper. In fact, the specific tensile strength of the C/Cu-alloy composite is significantly higher than that of pure copper.

Table 3.5. Comparison of ultimate strength for Cu and C/Cu.

Ultimate Strength	Copper	8-Harness Satin C/Cu
Tensile (ksi)	42.7	36.1
Compressive (ksi)	42.7	14.9
Shear (ksi)	-	8.0

Table 3.6. Comparison of specific strength for Cu and C/Cu.

Specific Strength	Copper	8-Harness Satin C/Cu
Tensile (in. $\times 10^6$)	133	166
Compressive (in. $\times 10^6$)	133	68.7
Shear (in. $\times 10^6$)	-	36.9

4. Analytical Model

The analytical model used in this investigation is an extension of the three dimensional version of the generalized method of cells micromechanics model (GMC-3D). GMC-3D uses an arbitrary number of homogeneous subcells to represent the repeating unit cell of a material. The extension of this model involved allowing the subcells to be inhomogeneous (and thus able to represent a portion of an infiltrated fiber yarn), including true rotational averaging to allow the infiltrated yarn subcells to exhibit transversely isotropic behavior, and including matrix plasticity on the subcell level.

4.1 GMC-3D

For a complete derivation of the equations for GMC-3D, see Aboudi (1994). The geometry considered for the model is shown in Figure 4.1. The composite is represented by a parallelepiped unit cell which repeats infinitely in the three orthogonal directions. The cell is divided into an arbitrary number of parallelepiped subcells, each denoted by the three indices $(\alpha\beta\gamma)$. The total number of subcells in each direction is denoted by N_α, N_β, and N_γ.

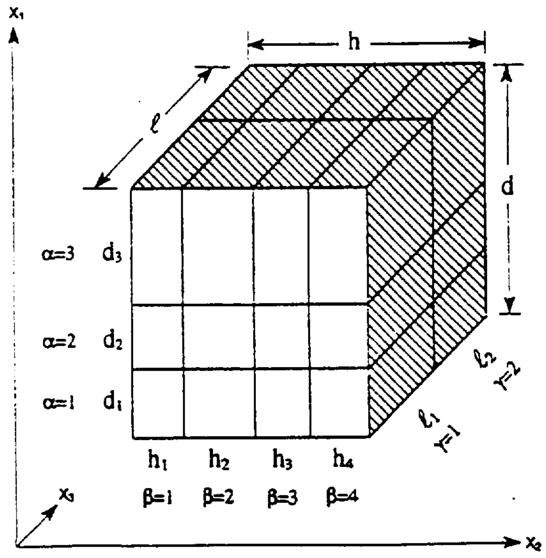

Figure 4.1: GMC-3D geometry.

The displacement field in each subcell is assumed to be first order in the local subcell coordinates, $(\bar{x}_1^{\alpha}, \bar{x}_2^{\beta}, \bar{x}_3^{\gamma})$, centered in the middle of each subcell,

$$u_i^{(\alpha\beta\gamma)} = w_i^{(\alpha\beta\gamma)} + \bar{x}_1^{(\alpha)} \phi_i^{(\alpha\beta\gamma)} + \bar{x}_2^{(\beta)} \chi_i^{(\alpha\beta\gamma)} + \bar{x}_3^{(\gamma)} \psi_i^{(\alpha\beta\gamma)}, \tag{4.1}$$

where the subcell microvariables, $\phi_i^{(\alpha\beta\gamma)}$, $\chi_i^{(\alpha\beta\gamma)}$, $\psi_i^{(\alpha\beta\gamma)}$, determine the displacement dependence on each subcell coordinate. The subcell strain components are given by the usual kinematic relations,

$$\varepsilon_{ij}^{(\alpha\beta\gamma)} = \frac{1}{2}\left(u_{j,i}^{(\alpha\beta\gamma)} + u_{i,j}^{(\alpha\beta\gamma)}\right) \qquad i, j = 1,2,3. \tag{4.2}$$

The strain components in each subcell are uniform, and the average strain components for the unit cell are given by the volume average of the strain components in the subcells,

$$\bar{\varepsilon}_{ij} = \frac{1}{dhl} \sum_{\alpha=1}^{N_\alpha} \sum_{\beta=1}^{N_\beta} \sum_{\gamma=1}^{N_\gamma} d_\alpha h_\beta l_\gamma \varepsilon_{ij}^{(\alpha\beta\gamma)}. \tag{4.3}$$

The stress components in each subcell are also uniform, and they are related to the strain components in the subcell by the subcell constitutive equation,

$$\sigma_{ij}^{(\alpha\beta\gamma)} = C_{ijkl}^{(\alpha\beta\gamma)}\left(\varepsilon_{kl}^{(\alpha\beta\gamma)} - \varepsilon_{kl}^{p(\alpha\beta\gamma)} - \varepsilon_{kl}^{T(\alpha\beta\gamma)}\right), \tag{4.4}$$

where $\varepsilon_{kl}^{p(\alpha\beta\gamma)}$ are the subcell plastic strain components and $\varepsilon_{kl}^{T(\alpha\beta\gamma)}$ are the subcell thermal strain components. The average stress components in the unit cell are given by the volume average of the subcell stress components,

$$\bar{\sigma}_{ij} = \frac{1}{dhl} \sum_{\alpha=1}^{N_\alpha} \sum_{\beta=1}^{N_\beta} \sum_{\gamma=1}^{N_\gamma} d_\alpha h_\beta l_\gamma \sigma_{ij}^{(\alpha\beta\gamma)}. \tag{4.5}$$

Continuity of displacements and tractions is required between subcells within the unit cell, and between the unit cell and adjacent unit cells. These continuity requirements are imposed in an average sense, which is to say that the integrals of the appropriate displacement and traction components along the appropriate boundaries are required to be continuous.

Imposing the displacement continuity conditions gives rise to the system of equations,

$$\mathbf{A}_G \,\varepsilon_s = \mathbf{J}\,\bar{\varepsilon}, \tag{4.6}$$

where, $\bar{\varepsilon} = \{\bar{\varepsilon}_{11} \;\; \bar{\varepsilon}_{22} \;\; \bar{\varepsilon}_{33} \;\; 2\bar{\varepsilon}_{23} \;\; 2\bar{\varepsilon}_{13} \;\; 2\bar{\varepsilon}_{12}\}$, and ε_s is the $6N_\alpha N_\beta N_\gamma$ order subcell strain vector given by $\varepsilon_s = \{\varepsilon^{(111)} \;\ldots\; \varepsilon^{(N_\alpha N_\beta N_\gamma)}\}$, where each vector $\varepsilon^{(\alpha\beta\gamma)}$ consists of the six subcell strain components. $\mathbf{A}_G$ contains cell geometric dimensions only, and it is a $[N_\alpha(N_\beta + N_\gamma + 1) + N_\beta(N_\gamma + 1) + N_\gamma] \times 6N_\alpha N_\beta N_\gamma$ matrix. $\mathbf{J}$ contains cell dimensions, and it is a $[N_\alpha(N_\beta + N_\gamma + 1) + N_\beta(N_\gamma + 1) + N_\gamma] \times 6$ matrix.

Imposing the traction continuity and using (4.4) gives rise to the system of equations,

$$\mathbf{A}_M\left(\varepsilon_s - \varepsilon_s^P - \varepsilon_s^T\right) = \mathbf{0}, \tag{4.7}$$

where ε_s^P and ε_s^T are $6N_\alpha N_\beta N_\gamma$ order subcell plastic and thermal strain vectors similar in composition to ε_s. Combining (4.7) and (4.6) gives,

$$\tilde{\mathbf{A}}\,\varepsilon_s - \tilde{\mathbf{D}}\left(\varepsilon_s^P + \varepsilon_s^T\right) = \mathbf{K}\,\bar{\varepsilon}, \tag{4.8}$$

where, $\tilde{\mathbf{A}} = \begin{bmatrix} \mathbf{A}_M \\ \mathbf{A}_G \end{bmatrix}$, $\tilde{\mathbf{D}} = \begin{bmatrix} \mathbf{A}_M \\ \mathbf{0} \end{bmatrix}$, $\mathbf{K} = \begin{bmatrix} \mathbf{0} \\ \mathbf{J} \end{bmatrix}$. Equation (4.8) can be solved for ε_s,

$$\varepsilon_s = \mathbf{A}\,\bar{\varepsilon} + \mathbf{D}\left(\varepsilon_s^P + \varepsilon_s^T\right) , \tag{4.9}$$

where, $\mathbf{A} = \tilde{\mathbf{A}}^{-1}\mathbf{K}$ and $\mathbf{D} = \tilde{\mathbf{A}}^{-1}\tilde{\mathbf{D}}$. If the matrices $\mathbf{A}$ and $\mathbf{D}$ are partitioned into $N_\alpha N_\beta N_\gamma$ sixth-order square submatrices such that $\mathbf{A} = \begin{bmatrix} \mathbf{A}^{(111)} \\ \vdots \\ \mathbf{A}^{(N_\alpha N_\beta N_\gamma)} \end{bmatrix}$ and $\mathbf{D} = \begin{bmatrix} \mathbf{D}^{(111)} \\ \vdots \\ \mathbf{D}^{(N_\alpha N_\beta N_\gamma)} \end{bmatrix}$, then equation (4.9) implies that,

$$\varepsilon^{(\alpha\beta\gamma)} = \mathbf{A}^{(\alpha\beta\gamma)}\bar{\varepsilon} + \mathbf{D}^{(\alpha\beta\gamma)}\left(\varepsilon_s^P + \varepsilon_s^T\right) . \tag{4.10}$$

This equation gives the strain components in each subcell in terms of the applied cell strains, the subcell plastic and thermal strains, and two concentration matrices, $\mathbf{A}^{(\alpha\beta\gamma)}$ and $\mathbf{D}^{(\alpha\beta\gamma)}$.

Substituting (4.10) into (4.4) yields,

$$\sigma^{(\alpha\beta\gamma)} = \mathbf{C}^{(\alpha\beta\gamma)}\left[\mathbf{A}^{(\alpha\beta\gamma)}\bar{\varepsilon} + \mathbf{D}^{(\alpha\beta\gamma)}\left(\varepsilon_s^p + \varepsilon_s^T\right) - \left(\varepsilon^{p(\alpha\beta\gamma)} + \varepsilon^{T(\alpha\beta\gamma)}\right)\right], \tag{4.11}$$

and using (4.5), the effective elastoplastic thermo-mechanical constitutive equation can be found,

$$\bar{\sigma} = \mathbf{B}^*\left(\bar{\varepsilon} - \bar{\varepsilon}^p - \bar{\varepsilon}^T\right) , \tag{4.12}$$

where the effective elastic stiffness matrix is,

$$\mathbf{B}^* = \frac{1}{dhl}\sum_{\alpha=1}^{N_\alpha}\sum_{\beta=1}^{N_\beta}\sum_{\gamma=1}^{N_\gamma} d_\alpha h_\beta l_\gamma \, \mathbf{C}^{(\alpha\beta\gamma)}\,\mathbf{A}^{(\alpha\beta\gamma)} , \tag{4.13}$$

the cell plastic strain vector is,

$$\bar{\varepsilon}^p = \frac{-\left(\mathbf{B}^*\right)^{-1}}{dhl}\sum_{\alpha=1}^{N_\alpha}\sum_{\beta=1}^{N_\beta}\sum_{\gamma=1}^{N_\gamma} d_\alpha h_\beta l_\gamma \, \mathbf{C}^{(\alpha\beta\gamma)}\left(\mathbf{D}^{(\alpha\beta\gamma)}\varepsilon_s^p - \varepsilon^{p(\alpha\beta\gamma)}\right), \tag{4.14}$$

the average thermal strain vector is,

$$\bar{\varepsilon}^T = \frac{-\left(\mathbf{B}^*\right)^{-1}}{dhl}\sum_{\alpha=1}^{N_\alpha}\sum_{\beta=1}^{N_\beta}\sum_{\gamma=1}^{N_\gamma} d_\alpha h_\beta l_\gamma \, \mathbf{C}^{(\alpha\beta\gamma)}\left(\mathbf{D}^{(\alpha\beta\gamma)}\varepsilon_s^T - \varepsilon^{T(\alpha\beta\gamma)}\right), \tag{4.15}$$

$\bar{\sigma}$ is the average stress vector, and $\bar{\varepsilon}$ is the imposed average strain vector.

4.2 Global Equation Solution Procedure in the Presence of Plasticity

The components of the effective stiffness matrix, $\mathbf{B}^*$, and the components of the thermal strain vector, $\bar{\varepsilon}^T$, appearing in equation (4.12) are determined directly from the original method of cells (see Section 4.3), while the global strain vector, $\bar{\varepsilon}$, is known from the imposed mechanical loading. When plasticity is present, the global equation (4.12) is nonlinear, and thus cannot be solved for the global stresses, $\bar{\sigma}$, directly. The nonlinearity arises because the components of the global plastic strain vector, $\bar{\varepsilon}^p$, depend on the local subcell plastic strains (see equation 4.14), which themselves depend implicitly on the global solution. Thus, to solve the global system of equations iteration is necessary to find the correct $\bar{\varepsilon}^p$ for the imposed $\bar{\varepsilon}$. In addition, the mechanical loading in the form of imposed global strains, $\bar{\varepsilon}$, as well as any thermal loading, must be applied in an incremental manner. The subcell plastic strains at a given magnitude of the thermomechanical loading are expressed as the subcell plastic strains at the previous thermomechanical load plus an increment in the subcell plastic strains due to the increment in the thermomechanical load. This procedure was outlined by Mendelson (1983) and can be summarized as,

$$\varepsilon^{p(\alpha\beta\gamma)}\Big|_{current} = \varepsilon^{p(\alpha\beta\gamma)}\Big|_{previous} + d\varepsilon^{p(\alpha\beta\gamma)}, \tag{4.16}$$

where $d\varepsilon^{p(\alpha\beta\gamma)}$ are the increments in the subcell plastic strain vector calculated using the method of cells in conjunction with classical incremental plasticity theory. Section 4.5 will discuss how the plastic strain increments are calculated at the subcell level.

The iterative procedure actually used in the model allows equation (4.12) to be bypassed. The subcell strain concentration equation (4.9) is used instead. The subcell and global stresses are calculated after convergence has occurred for a particular loading increment and are not active in the iteration procedure. The iterative procedure is as follows:

1) Apply a loading increment (i.e., a small increase in temperature or strain).

2) Estimate the subcell plastic strains from equation (4.16).

3) Obtain the strains in each subcell from equation (4.9) ($\bar{\varepsilon}$ and ε_s^T are known).

4) Apply these subcell strains to the original method of cells, from which new estimates of the subcell plastic strain increments are determined (through the use of the plasticity equations).

5) Update the subcell plastic strains with equation (4.16) using the new plastic strain increment values.

6) Check for convergence of the subcell plastic strains.

7) If convergence has been achieved, calculate the subcell and global stresses from equations (4.11) and (4.12) and go to step 1.

8) If convergence has not been achieved, go to step 3.

4.3 Heterogeneous Subcells via the Original Method of Cells

In order to model a woven composite with GMC-3D, it is necessary to allow the 3D subcells to be unidirectional composites. The fiber direction of the unidirectional composite in each 3D subcell is arbitrary, as is the fiber material, matrix material, and fiber volume fraction. The unidirectional composite in each subcell is modeled in its principal material coordinates by the original method of cells, also developed by Aboudi (1987) (see Figure 4.2).

The original method of cells develops effective constitutive equations for the two-dimensional unit cell shown in Figure 4.2 consisting of three matrix subcells and one fiber subcell. These constitutive equations, in turn, describe the average response of the subcells $(\alpha\beta\gamma)$ in GMC-3D. The procedure for developing the effective constitutive relations is similar to the procedure used in GMC-3D: a first order displacement field is assumed for the subcells and continuity of displacements and tractions between subcells and between cells is imposed in an average sense. The resulting effective constitutive equations are,

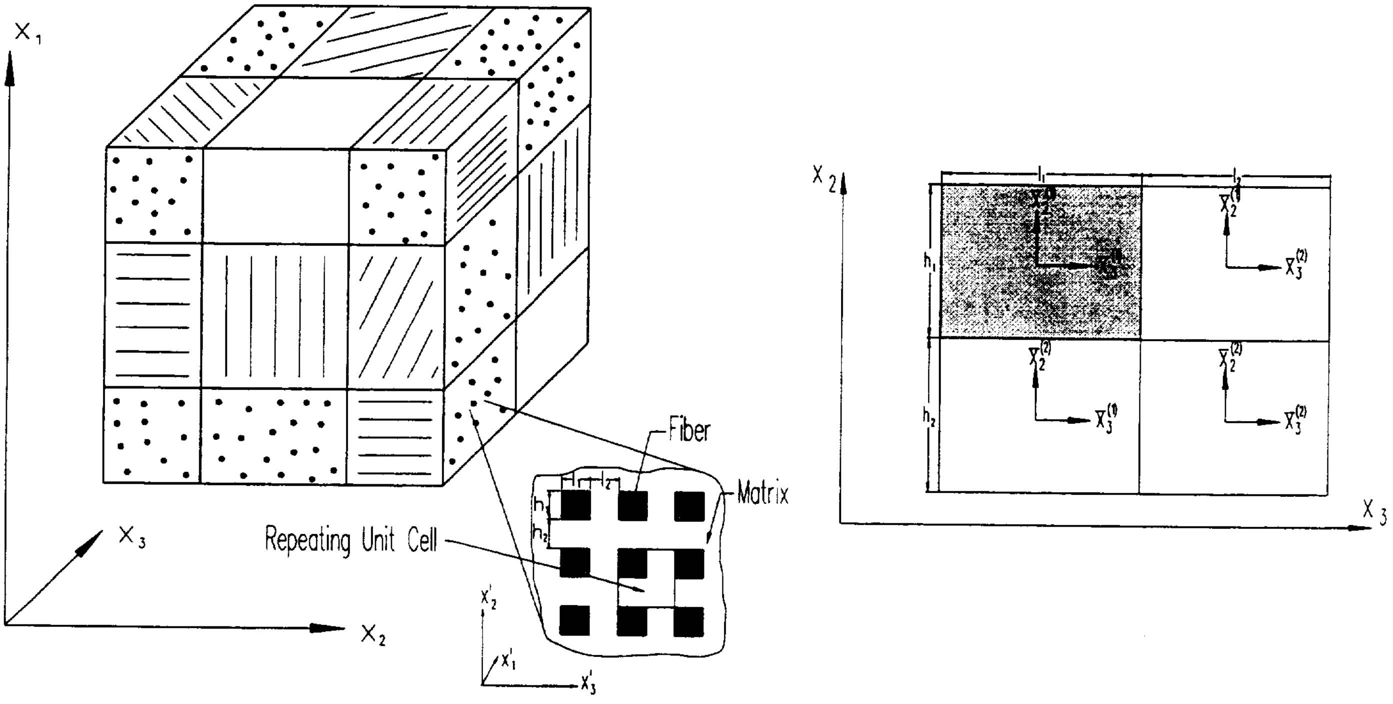

Figure 4.2. Incorporation of composite subcells into GMC-3D via the original method of cells.

$$\begin{bmatrix} \bar{\sigma}_{11} \\ \bar{\sigma}_{22} \\ \bar{\sigma}_{22} \\ \bar{\sigma}_{12} \\ \bar{\sigma}_{13} \\ \bar{\sigma}_{23} \end{bmatrix}^{(\alpha\beta\gamma)} = \begin{bmatrix} b_{11} & b_{12} & b_{13} & 0 & 0 & 0 \\ b_{12} & b_{22} & b_{23} & 0 & 0 & 0 \\ b_{13} & b_{23} & b_{33} & 0 & 0 & 0 \\ 0 & 0 & 0 & b_{44} & 0 & 0 \\ 0 & 0 & 0 & 0 & b_{55} & 0 \\ 0 & 0 & 0 & 0 & 0 & b_{66} \end{bmatrix}^{(\alpha\beta\gamma)} \left\{ \begin{bmatrix} \bar{\varepsilon}_{11} \\ \bar{\varepsilon}_{22} \\ \bar{\varepsilon}_{33} \\ 2\bar{\varepsilon}_{12} \\ 2\bar{\varepsilon}_{13} \\ 2\bar{\varepsilon}_{23} \end{bmatrix}^{(\alpha\beta\gamma)} - \Delta T \begin{bmatrix} \alpha_1^* \\ \alpha_2^* \\ \alpha_3^* \\ 0 \\ 0 \\ 0 \end{bmatrix}^{(\alpha\beta\gamma)} \right\} - \begin{bmatrix} H_{11} \\ H_{22} \\ H_{33} \\ H_{12} \\ H_{13} \\ H_{23} \end{bmatrix}^{(\alpha\beta\gamma)}, \quad (4.17)$$

where b_{ij} are components of the effective stiffness matrix, H_{ij} contain the plastic terms, and α_i^* are the effective cell CTEs. The expressions for b_{ij}, H_{ij}, and α_i^* are given in the appendix. For a square cell and square subcells (i.e., $h_1 = h_2$ and $l_1 = l_2$), $b_{12} = b_{13}$, $b_{22} = b_{33}$, and $b_{44} = b_{55}$.

Thus, given the geometry and properties of the fibers and matrix that constitute the unidirectional composites in each 3D subcell, the original method of cells is used to calculate effective thermo-elastic properties for each 3D subcell in the principal material coordinates of the given 3D subcell. An effective stiffness matrix is then assembled for each 3D subcell in the principal coordinates, and this stiffness matrix is rotated in three dimensions to the coordinates of the 3D cell. GMC-3D uses these effective stiffness matrices for each 3D subcell to determine the effective stiffness matrix and effective properties for the 3D cell. If the woven composite is treated as purely elastic, this is all that is required to allow modeling. However, if matrix plasticity is included, the formulation becomes more complex.

As discussed in the previous section, the subcell plastic strain increments are determined from the original method of cells in conjunction with the classical incremental plasticity theory. The total strains in each 3D subcell, known from the solution of the global equations (4.12) and equation (4.10), represent the average unit cell strains in the original method of cells. From these average unit cell strains, strain components for each of the original method of cells subcells can be determined via concentration equations from the original method of cells. The knowledge of these original subcell strains allows the determination of original subcell stresses, and thus plastic strain increments within each original subcell using the classical incremental plasticity theory equations presented in Section 4.5. These original subcell plastic strain increments are then used to evaluate increments in the plastic terms (the H_{ij} terms) in (4.17). The H_{ij} increments are then used to determine the original unit cell plastic strain increments from,

$$\left\{\begin{matrix} d\bar{\varepsilon}_{11}^{p} \\ d\bar{\varepsilon}_{22}^{p} \\ d\bar{\varepsilon}_{33}^{p} \\ d\bar{\varepsilon}_{12}^{p} \\ d\bar{\varepsilon}_{13}^{p} \\ d\bar{\varepsilon}_{23}^{p} \end{matrix}\right\}^{(\alpha\beta\gamma)} = \begin{bmatrix} b_{11} & b_{12} & b_{13} & 0 & 0 & 0 \\ b_{12} & b_{22} & b_{23} & 0 & 0 & 0 \\ b_{13} & b_{23} & b_{33} & 0 & 0 & 0 \\ 0 & 0 & 0 & b_{44} & 0 & 0 \\ 0 & 0 & 0 & 0 & b_{55} & 0 \\ 0 & 0 & 0 & 0 & 0 & b_{66} \end{bmatrix}^{(\alpha\beta\gamma)^{-1}} \left\{\begin{matrix} dH_{11} \\ dH_{22} \\ dH_{33} \\ \frac{1}{2}\,dH_{12} \\ \frac{1}{2}\,dH_{13} \\ \frac{1}{2}\,dH_{23} \end{matrix}\right\}^{(\alpha\beta\gamma)} . \tag{4.18}$$

These original unit cell plastic strain increments are rotated back to the global coordinates, and then they represent the 3D subcell plastic strain increments for the 3D subcell considered. The 3D subcell plastic strain increments are used as described in Section 4.2 to solve the global equations (4.12), for the entire 3D unit cell.

4.4 True Rotational Averaging

The effective elastoplastic constitutive equation from the original method of cells (equation (4.17)) includes six independent effective elastic stiffness constants, b_{ij}, when the subcells are square. However, a unidirectional composite containing small diameter fibers is typically transversely isotropic, represented by five independent elastic constants. To obtain the desired transversely isotropic composite behavior from the method of cells, a modification to the stiffness components must be made. Aboudi (1987) suggested that orientational averages of the b_{ij} terms be taken in the $x_2 - x_3$ plane (see Figure 4.2). This is done via the equation,

$$\mathbf{E} = \frac{1}{\pi}\int_0^{\pi} \mathbf{B}'(\theta)\, d\theta , \tag{4.19}$$

where $\mathbf{B}'(\theta)$ is the matrix of the b_{ij} terms rotated by the angle θ in the $x_2 - x_3$ plane, and $\mathbf{E}$ is the resulting matrix of transversely isotropic effective elastic stiffness components.

The above procedure results in transversely isotropic elastic behavior, however, Brayshaw (1994) showed that the procedure results in an inconsistency in the stress concentration composition. This is to say that the volume weighted averages of the subcell stress components no longer equal the average unit cell stress components as a result of the rotational averaging procedure. This inconsistency has serious ramification when three-dimensional rotation of the effective stiffness components is performed, as is done in the present model. For instance, if 3D rotation of the effective transversely isotropic stiffness components were performed such that the unidirectional fiber direction corresponds to the diagonal direction in a cube, the effective behavior should be identical for all three directions in the cube (see Figure 4.3). However, if the composite elastic constants are evaluated based on the stiffness averaging approach, this is not the case. The rotated stiffnesses for the cube-diagonal configuration dictate different elastic behavior for each direction (1, 2, or 3 in Figure 4.3).

Brayshaw (1994) eliminated the inconsistency by performing the rotational averaging based on the subcell strains rather than the stiffnesses. The averaging may be performed directly on the total and plastic-thermal strain concentration matrices in the original method of cells via,

$$\hat{\mathrm{A}}^{(\beta\gamma)} = \frac{2}{\pi} \int_{-\frac{\pi}{4}}^{\frac{\pi}{4}} \left[\mathrm{N}(\theta)^{-1} \mathrm{A}^{(\beta\gamma)} \mathrm{N}(\theta) \right] d\theta \,, \tag{4.20}$$

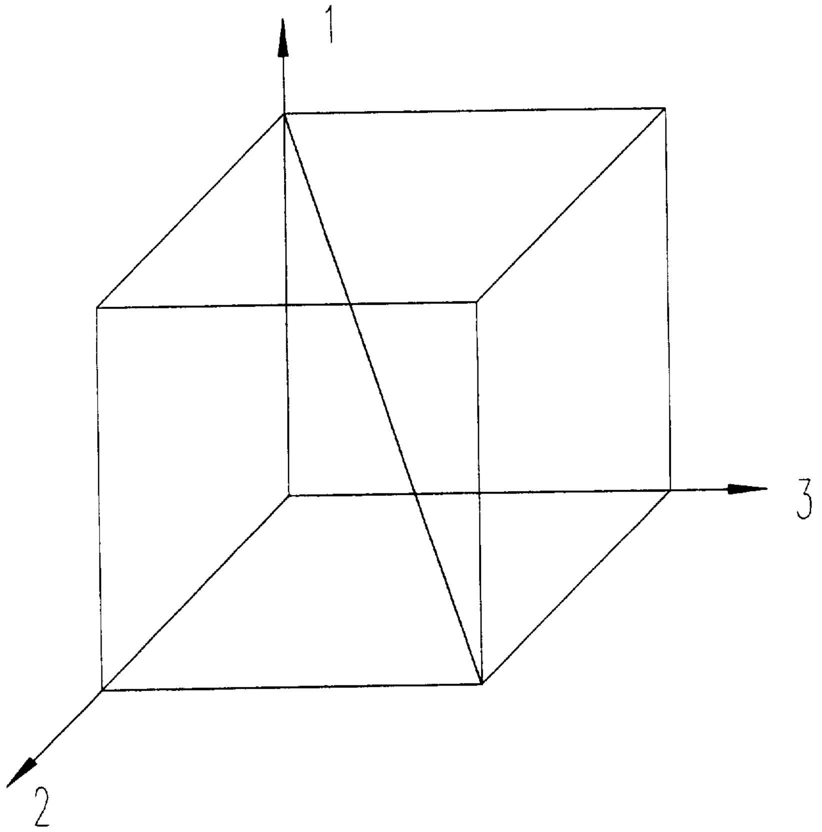

Figure 4.3. Cube-diagonal fiber orientation.

$$\hat{\mathbf{A}}^{PT(\beta\gamma,\xi\eta)} = \frac{2}{\pi}\int_{-\frac{\pi}{4}}^{\frac{\pi}{4}} \left[\mathbf{N}(\theta)^{T}\,\mathbf{A}^{PT(\beta\gamma,\xi\eta)}\,\mathbf{N}(\theta)^{-1T}\right] d\theta\,, \tag{4.21}$$

where $\mathbf{N}(\theta)$ is the rotation matrix,

$$\mathbf{N}(\theta) = \begin{bmatrix} 1 & 0 & 0 & 0 & 0 & 0 \\ 0 & c^2 & s^2 & 0 & 0 & -sc \\ 0 & s^2 & c^2 & 0 & 0 & sc \\ 0 & 0 & 0 & c & -s & 0 \\ 0 & 0 & 0 & s & c & 0 \\ 0 & 2sc & -2sc & 0 & 0 & c^2 - s^2 \end{bmatrix}, \tag{4.22}$$

where s and c are the sine and cosine of the angle θ in the $x_2 - x_3$ plane, respectively. $\mathbf{A}^{(\beta\gamma)}$ is the unaveraged total strain concentration matrix, $\mathbf{A}^{PT(\beta\gamma)}$ is the unaveraged plastic-thermal strain concentration matrix, and hats denote the rotationally averaged quantities. Equations for the averaged and unaveraged strain concentration matrices may be found in Brayshaw (1994) in terms of the subcell dimensions and stiffness terms. The subcell total strains can be represented in terms of the averaged concentration matrices as,

$$\varepsilon^{(\beta\gamma)} = \hat{\mathbf{A}}^{(\beta\gamma)}\bar{\varepsilon} + \sum_{(\xi\eta)} \hat{\mathbf{A}}^{PT(\beta\gamma,\xi\eta)}\varepsilon^{p(\xi\eta)} + \sum_{(\xi\eta)} \hat{\mathbf{A}}^{PT(\beta\gamma,\xi\eta)}\varepsilon^{T(\xi\eta)}. \tag{4.23}$$

The original method of cells effective constitutive equation, equation (4.17), can be written in a form similar to (4.12),

$$\bar{\sigma} = \mathbf{B}\left(\bar{\varepsilon} - \bar{\varepsilon}^{T} - \bar{\varepsilon}^{p}\right)\,, \tag{4.24}$$

where $\varepsilon^{T} = \alpha^{*}\Delta T$ and $\mathbf{H} = \mathbf{B}\bar{\varepsilon}^{p}$. The components of equation (4.24) can then be expressed in terms of the averaged strain concentration matrices as,

$$\mathbf{B} = \sum_{(\beta\gamma)} \frac{h_\beta l_\gamma}{hl}\mathbf{C}^{(\beta\gamma)}\hat{\mathbf{A}}^{(\beta\gamma)}, \tag{4.25}$$

$$\bar{\varepsilon}^{p} = \frac{\mathbf{B}^{-1}}{hl}\left[\sum_{(\beta\gamma)} h_\beta l_\gamma \mathbf{C}^{(\beta\gamma)}\left(\varepsilon^{p(\beta\gamma)} - \sum_{(\xi\eta)} \hat{\mathbf{A}}^{PT(\beta\gamma,\xi\eta)}\varepsilon^{p(\xi\eta)}\right)\right], \tag{4.26}$$

$$\bar{\varepsilon}^{T} = \frac{\mathbf{B}^{-1}}{hl}\left[\sum_{(\beta\gamma)} h_\beta l_\gamma \mathbf{C}^{(\beta\gamma)}\left(\varepsilon^{T(\beta\gamma)} - \sum_{(\xi\eta)} \hat{\mathbf{A}}^{PT(\beta\gamma,\xi\eta)}\varepsilon^{T(\xi\eta)}\right)\right], \tag{4.27}$$

where $C^{(\beta\gamma)}$ is the stiffness matrix for the original subcell $(\beta\gamma)$. The effective constitutive equations, with strain concentration averaging as presented by Brayshaw (1994), are used in the present model to obtain the effective 3D subcell properties and to relate the original unit cell strains and strain increments to the original subcell strains and strain increments.

4.5 Classical Incremental Plasticity Theory

The equations for calculation of the plastic strain increments in the original method of cells subcells are here presented. The derivation follows that of Mendelson (1983) and simplifications provided by Williams and Pindera (1994) and Williams (1995). Omitting the designation $(\beta\gamma)$ that identifies a given subcell in the original method of cells for notational simplicity, the total strain components are given by the sum of the elastic strain components, the plastic strain components, and the plastic strain increments,

$$\varepsilon_{ij} = \varepsilon^{e}_{ij} + \varepsilon^{p}_{ij} + d\varepsilon^{p}_{ij} . \tag{4.28}$$

The modified total strain components are defined as,

$$\varepsilon'_{ij} \equiv \varepsilon_{ij} - \varepsilon^{p}_{ij} . \tag{4.29}$$

Combining equations (4.28) and (4.29) yields,

$$\varepsilon'_{ij} = \varepsilon^{e}_{ij} + d\varepsilon^{p}_{ij} . \tag{4.30}$$

The mean dilatation is subtracted from (4.30) to give,

$$\underbrace{\varepsilon'_{ij} - \frac{1}{3}\varepsilon_{kk}\delta_{ij}}_{e'_{ij}} = \underbrace{\varepsilon^{e}_{ij} - \frac{1}{3}\varepsilon_{kk}\delta_{ij}}_{e^{e}_{ij}} + d\varepsilon^{p}_{ij} , \tag{4.31}$$

where, e'_{ij} and e^{e}_{ij} are deviatoric quantities defined as shown. Elastic Hooke's Law is given by,

$$e^{e}_{ij} = \frac{1}{2G}\sigma'_{ij} , \tag{4.32}$$

and the Prandtl-Reuss equations are given by,

$$d\varepsilon^{p}_{ij} = \sigma'_{ij}\, d\lambda , \tag{4.33}$$

where, $d\lambda$ is the proportionality constant obtained from the consistency condition requiring that the stress vector remains on the yield surface during plastic loading. Eliminating the deviatoric stress using (4.32) and (4.33) yields,

$$e_{ij}^{e} = \frac{1}{2G\,d\lambda}\,d\varepsilon_{ij}^{p}\,, \tag{4.34}$$

and substituting for e_{ij}^{e} in equation (4.31) using (4.34) yields,

$$e'_{ij} = \left(1 + \frac{1}{2G\,d\lambda}\right) d\varepsilon_{ij}^{p}\,. \tag{4.35}$$

The equivalent modified total strain is defined as,

$$\varepsilon_{et} \equiv \sqrt{\tfrac{2}{3} e'_{ij} e'_{ij}}\,. \tag{4.36}$$

Substituting for e'_{ij} in equation (4.36) using (4.35) yields,

$$\varepsilon_{et} = \sqrt{\frac{2}{3}\left(1 + \frac{1}{2G\,d\lambda}\right)^{2} d\varepsilon_{ij}^{p}\, d\varepsilon_{ij}^{p}} = \left(1 + \frac{1}{2G\,d\lambda}\right) \underbrace{\sqrt{\frac{2}{3} d\varepsilon_{ij}^{p}\, d\varepsilon_{ij}^{p}}}_{d\varepsilon_{eff}^{p}}\,, \tag{4.37}$$

where the definition of the effective plastic strain increment, $d\varepsilon_{eff}^{p}$ has been indicated. Combining (4.35) and (4.37) to eliminate the term $\left(1 + \frac{1}{2G\,d\lambda}\right)$ yields,

$$e'_{ij} = \frac{\varepsilon_{et}}{d\varepsilon_{eff}^{p}}\, d\varepsilon_{ij}^{p}\,, \tag{4.38}$$

which, upon rearrangement, becomes,

$$d\varepsilon_{ij}^{p} = \frac{d\varepsilon_{eff}^{p}}{\varepsilon_{et}}\, e'_{ij}\,. \tag{4.39}$$

It can be shown that the proportionality constant, $d\lambda$, can be expressed as,

$$d\lambda = \frac{3}{2}\frac{d\varepsilon_{eff}^{p}}{\bar{\sigma}_{eff}}\,. \tag{4.40}$$

Substituting for $d\lambda$ in equation (4.37) using (4.39) results in,

$$d\varepsilon_{eff}^{p} = \varepsilon_{et} - \frac{\bar{\sigma}_{eff}}{3G}\,, \tag{4.41}$$

and substituting for $d\varepsilon_{eff}^{p}$ in equation (4.39) using (4.41) yields,

$$d\varepsilon_{ij}^{p} = \underbrace{\left(1 - \frac{\bar{\sigma}_{eff}}{3G\,\varepsilon_{et}}\right)}_{d\lambda'} e'_{ij}\,, \tag{4.42}$$

where a modified proportionality constant, $d\lambda'$, has been defined.

The plastic strain increments for the original method of cells subcells are calculated from equation (3.42). This equation represents a modification of the Prandtl-Reuss equations (4.33), such that the plastic strain increments are calculated from the modified total strain deviator rather than from the stress deviator. This form allows better convergence when it is employed in the iterative solution procedure. The terms in equation (4.42) are given by,

$$e'_{ij} = \varepsilon_{ij} - \varepsilon^{p}_{ij} - \frac{1}{3}\delta_{ij}\varepsilon_{kk}\,, \qquad \varepsilon_{et} = \sqrt{\frac{2}{3}e'_{ij}e'_{ij}}\,, \qquad \bar{\sigma}_{eff} = H\varepsilon^{p}_{eff} + Y\,, \tag{4.43}$$

where,

$$H = \frac{E\,H_{SP}}{E - H_{SP}}\,, \tag{4.46}$$

where E, H_{SP}, and Y are the elastic modulus, hardening slope, and yield stress for the material based on a bilinear stress-strain response.

5. Modeling the Mechanical Response of 8-Harness Satin C/Cu

In this chapter, predictions of the analytical model (described in the previous chapter) are presented. In particular, the effects of unit cell refinement, fiber volume fraction, strain gauge size and placement, and porosity on the predicted tensile and shear response of 8-harness satin C/Cu are examined. These effects are investigated in order to determine which are important and how each affects the predictions. Those effects that are important will then be employed in Chapter 6 as the model predictions are compared with experiment.

5.1 Effect of Unit Cell Refinement

One benefit of utilizing GMC-3D to model woven composites is the geometric flexibility offered by the model. As long as a repeating unit cell can be identified for a given inhomogeneous material, the micro-scale geometry can be discretized into parallelepiped subcells and modeled with GMC-3D. In addition, the averaged continuity conditions employed by GMC-3D make precise geometrical representation less important than it is for numerical finite-element or boundary-element models. It has been shown (Wilt, 1995) that for similar geometrical representations, the two-dimensional version of the generalized method of cells (GMC-2D) with 49 subcells matched elastoplastic finite-element predictions obtained using a 1088 element mesh. For the above cases, the CPU time for the finite element model execution was 3550 times that required for GMC-2D execution.

The repeating unit cells for woven composites are often quite complex. The weave of fiber yarns is inherently three-dimensional, and each different weave type has a different repeating unit cell (see Figure 1.3, for example). For an 8-harness satin weave, the repeating unit cell is shown (from above) in Figure 2.6. The unit cell is large, encompassing eight yarns in each of the two directions, but it is the smallest rectangular repeating unit cell for this type of weave. A slightly smaller repeating unit cell can be identified if the rectangular shape requirement is relaxed, but for implementation in GMC-3D, the unit cell must be a parallelepiped.

For a composite reinforced with an 8-harness satin weave, the simplest geometrical representation of the true three-dimensional unit cell is shown in Figure 5.1. This geometry is similar to the mosaic model of Chou and Ishikawa (1989) (see Figure 1.4) in the way it treats the fiber yarn cross-over points. The weave appears similar to a [0/90] laminate, with the 0° and 90° plies reversing stacking sequence at the yarn cross-over points. Unlike the mosaic model, however, the geometry shown in Figure 5.1 represents the entire three dimensional 8-harness satin unit cell, not just a two-dimensional section of it. This geometry will be referred to as the true mosaic model (TMM). Note that the TMM geometry incorporates pure layers of the copper matrix on the top and bottom of the unit cell, which mimics actual woven composites (see Figure 1.10 (a)). The darkened top subcells in Figure 5.1 indicate the positions (in the plane of the weave) of the fiber yarn cross-over points.

An additional point to consider when examining the unit cell geometry shown in Figure 5.1 is the fact that GMC-3D models the geometry shown as a representative part of an infinite medium. That is, the unit cell repeats infinitely in each direction, not just in the plane of the weave. Thus, the geometry shown actually represents an infinite number of reinforcement weave layers, separated by regions of pure copper matrix. This contrasts with the models of Chou and Ishikawa (1989) and Naik and Ganesh (1992) which utilize lamination theory and thus model a plate, with free surfaces, reinforced with a single woven layer.

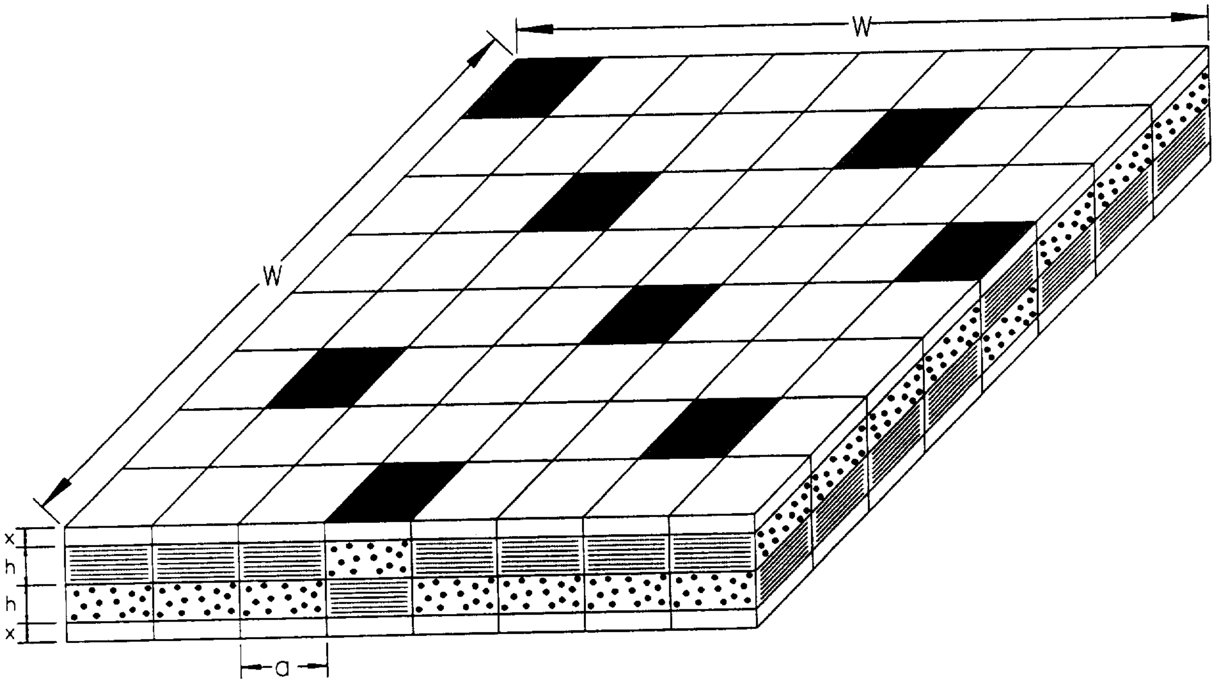

Figure 5.1. True Mosaic Model (TMM) unit cell geometry.

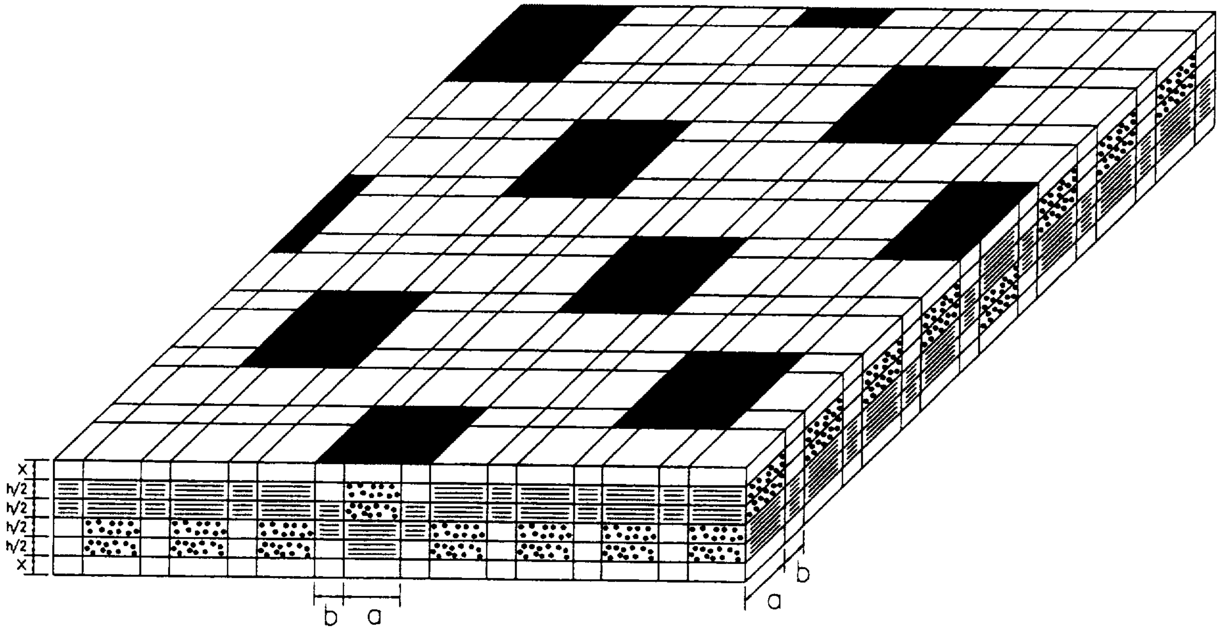

Figure 5.2 (a). Continuous Mosaic Model (CMM) unit cell geometry.

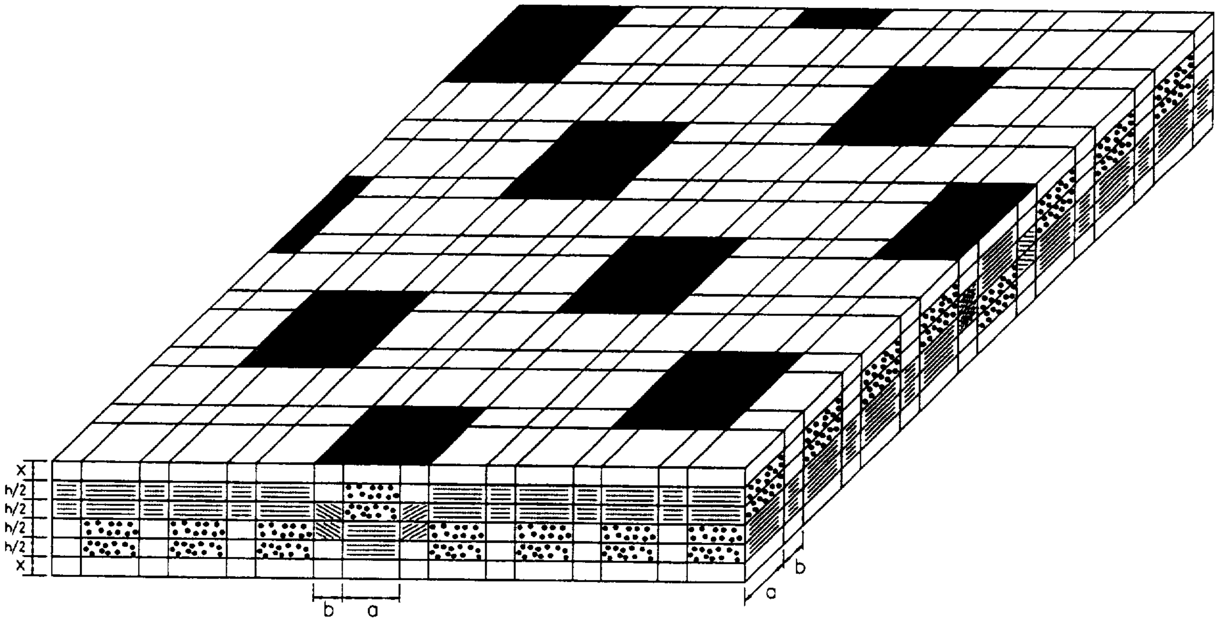

Figure 5.2 (b). Directionally Continuous Mosaic Model (DCMM) unit cell geometry.

The unit cell geometry shown in Figure 5.1 includes pure matrix layers above and below the weave, but no other regions of pure matrix. Thus, in order to vary the overall fiber volume fraction of the woven composite independently of the fiber volume fraction of the yarn subcells, the thickness of the pure matrix layers is varied with respect to the weave subcell thickness. That is, the ratio *x/h* defined in Figure 5.1 is varied. Choice of the dimension *w* is arbitrary. In addition, the TMM geometry lacks fiber continuity at the yarn cross-over points. In order to allow more freedom in varying the fiber volume fraction, as well as a more accurate representation of the cross-over geometry, a unit cell with considerably more subcells must be employed. Figure 5.2(a) and (b) show the next level of refinement for the 8-harness satin weave composite unit cell geometry. The geometry shown in Figure 5.2(a) is referred to as the continuous mosaic model (CMM), and the geometry shown in Figure 5.2(b), which explicitly includes rotated fibers in the cross-over regions, is called the directionally continuous mosaic model (DCMM).

Clearly, the CMM and DCMM geometries provide superior representation of the woven composite compared to the TMM geometry. In addition, the CMM and DCMM geometries include pure matrix subcells besides those located in the top and bottom layers of the unit cell. This allows an additional geometric degree of freedom when tailoring the subcell dimensions to provide a particular overall fiber volume fraction. However, these refinements come at a computational cost. The TMM unit cell is comprised of 256 subcells (8x8x6), while the CMM and DCMM unit cells are each comprised of 1536 subcells (16x16x6). For implementation in the model these numbers can be reduced to 192 (8x8x3) and 1280 (16x16x5) by combining the top pure matrix layer of the unit cell with the bottom pure matrix layer of the unit cell above the unit cell being considered. GMC-3D execution times are quite sensitive to the number of subcells comprising the unit cell considered, and thus full elastoplastic cases using the CMM and DCMM geometries cannot be realistically executed at this time. For this reason, model results for the CMM and the DCMM unit cells are limited to elastic predictions. The majority of the results presented, including those used to examine the effects of fiber volume fraction (Section 5.2), strain gauge size and placement (Section 5.3), and porosity (Section 5.4), were generated using the TMM geometry.

Table 5.1 shows a comparison of the predicted effective elastic properties for 8-harness satin C/Cu using the TMM, CMM, and DCMM geometries to model the composite with a fiber volume fraction of 40%. The properties of the carbon fiber and the copper matrix, which are required as input data for the model, are given in Table 5.2. In these cases, the fiber volume fraction of the fiber yarn subcells was taken to be 65%. This value was determined via microscopic examination of actual C/Cu specimens. The dimensions of the subcells (indicated in Figures 5.1 and 5.2(a)) were tailored such that the overall fiber volume fraction was 40%, while maintaining the yarn subcell fiber volume fraction at 65%. Table 5.3 provides the subcell dimensions utilized. For the CMM and DCMM geometries, the dimensions of the copper layers and the fiber yarn subcells were determined from microscopic examination of C/Cu samples, and the cross-over subcell widths (dimension b in Figure 5.2(a)) were chosen such that the overall fiber volume fraction of the subcell was 40%. The resulting dimensions for the CMM and DCMM unit cells are quite realistic. A rotation angle of 13.5° was used for the fibers in the cross-over subcells in the DCMM geometry.

Table 5.1 indicates that the level of unit cell geometrical refinement has only a minor effect in the elastic region. The model predicts elastic constants that are very similar for all the geometries. In fact, the predicted in-plane elastic properties for the CMM and DCMM geometries are identical. Once yielding of the matrix occurs, divergence of the predictions for the different unit cells is expected. Arnold *et al.* (1995) found the constitutive response of MMCs to be significantly more sensitive to geometry changes after matrix yielding has occurred. At this time, however, the elastoplastic cases cannot be executed, and examination of the effect of unit cell refinement on the post-yield behavior of 8-harness satin C/Cu is thus postponed.

Table 5.1. Comparison of geometric model in-plane elastic property predictions for 40% 8-harness satin C/Cu.

	E (Msi)	*ν*	*G* (Msi)
TMM	15.62	0.254	6.73
CMM	15.47	0.248	6.73
DCMM	15.47	0.248	6.73

Table 5.2. Fiber and matrix mechanical properties.

	E_A (Msi)	E_T (Msi)	G_A (Msi)	ν_A	ν_T	Y (ksi)	H_{SP} (Msi)
VCX-11 Fiber	29.42	3.67	6.40	0.443	0.05	-	-
Copper Matrix	18.8	18.8	6.93	0.35	0.35	10.3	1.425

Table 5.3. Geometrical model subcell dimensions

	x	h	a	b
TMM	0.0125	0.02	-	-
CMM/DCMM	0.01	0.02	0.0833	1

5.2 Effect of Fiber Volume Fraction

5.2.1 Monotonic Tensile Response

Since GMC-3D is a material-based model which presently provides no failure or damage mechanism, and since residual stresses have not been considered, the predicted tensile and compressive behavior of the woven composite is identical, save the reversed sign of the stresses and strains. Hence, only tensile predictions will be provided in this section.

Figure 5.3 shows the predicted tensile response of the woven C/Cu composite using the TMM geometry for the overall fiber volume fractions of 40%, 45%, and 50%. Recall that for the TMM geometry, the overall fiber volume fraction is varied by changing the thickness of the pure copper layers with respect to the thickness of the fiber yarn subcells (see Figure 5.1). The *x/h* ratios for the fiber volume fractions are 0.625, 0.444, and 0.300, respectively, while the fiber volume fraction of the fiber yarn subcells is fixed at 65%.

Figure 5.3 indicates that the differences in the elastic response for all three fiber volume fractions are small. It is not until the onset of plasticity that the predicted tensile stress-strain curves begin to diverge noticeably. Table 5.4 shows that the predicted tensile modulus and yield stress vary with the volume fraction in a manner opposite to that usually expected for unidirectional fibrous composites. That is, the lowest fiber volume fraction results in the highest modulus and yield stress. The transverse stiffness of the carbon fiber is lower than that of the copper matrix, so adding thicker layers of pure copper decreases the overall fiber volume fraction, but increases the effective stiffness. Indeed, the predicted effective elastic tensile

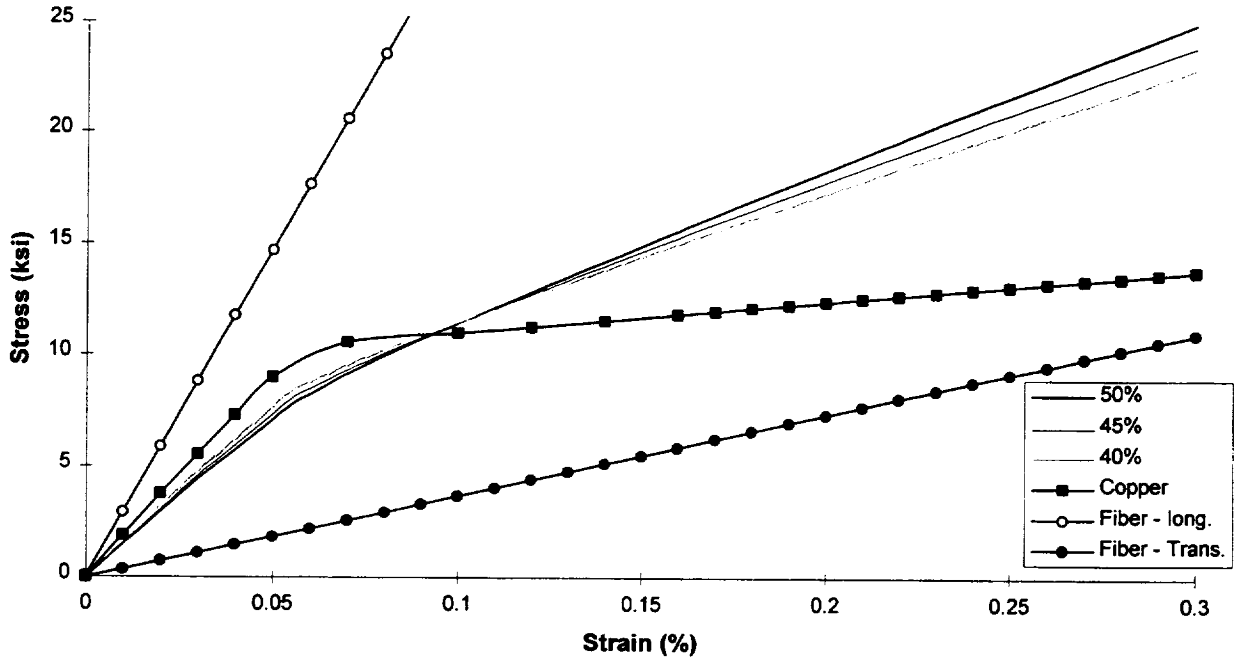

Figure 5.3. Effect of fiber volume fraction on the predicted tensile response of 8-harness satin C/Cu as represented by the TMM geometry.

Table 5.4. Effective in-plane tensile property predictions.

V_f	E (Msi)	ν	Y (ksi)	H_{SP} (Msi)
40 %	15.62	0.254	9.83	6.00
45 %	15.19	0.239	9.32	6.43
50 %	14.76	0.222	9.14	6.93

modulus for each fiber volume fraction is lower than that of pure copper (see Table 5.1). The higher predicted tensile yield stresses associated with the lower overall fiber volume fractions are the result of the higher stiffnesses. The higher stiffness allows a higher stress to be reached at the strain that results in the onset of matrix plasticity.

The predicted in-plane Poisson ratio provides insight into the transverse behavior of the composite. As the thickness of the pure copper layers is decreased (and thus the over fiber volume fraction increased), the high axial stiffness of the yarns oriented transverse to the loading direction provides more constraint to transverse contraction. Thus, as the overall fiber volume fraction is increased, the predicted Poisson ratio decreases.

Once plastic deformation begins to occur, the predicted tensile stress-strain curves in Figure 5.3 cross each other, and the post-yield hardening slopes of the curves follow the opposite trend based on fiber volume fraction compared to the elastic tensile moduli. This is due to the reduction in the effective stiffness in the pure copper subcells associated with yielding. Now the transverse stiffness of the fiber is greater than that of the flowing matrix, and the thicker pure matrix layers decrease the overall post-yield stiffness of the composite.

5.2.2 Monotonic Shear Response

The TMM geometry was also used to predict the elastoplastic response of 8-harness satin C/Cu to monotonic in-plane shear loading. Figure 5.4 shows the predicted shear stress-strain curves for the fiber volume fractions of 40%, 45%, and 50%. Table 5.5 provides the predicted effective shear moduli, shear yield stresses, and shear post-yield hardening slopes for the composites. It should be noted that the axial and transverse shear moduli of the carbon fiber are both lower than the shear modulus of pure copper (see Table 5.2).

The predicted effective shear modulus and post-yield hardening slope for the woven composite follow the same trends based on fiber volume fraction as the predicted effective tensile modulus and post-yield hardening slope. The reason for these trends is the same as well. The pure matrix layers are stiffer in shear than the transverse yarn subcells. However, once yielding occurs, this is no longer the case. The predicted shear moduli for each fiber volume fraction fall between the shear modulus of the copper and the axial shear modulus of the fiber. The difference between these two quantities is small, so the effect of varying the overall fiber volume fraction on the shear modulus is small. The effect of the fiber volume fraction on the predicted post-yield hardening slope is more pronounced.

The predicted yield stress in shear is nearly the same for each fiber volume fraction, but the trend based on fiber volume fraction is opposite the trend predicted for the yield stress in tension. This is because the yield stress reported is actually the stress at which 0.01% permanent strain has accrued. The effective shear moduli for all three fiber volume fractions are so similar that, at the point along the stress-strain curve where 0.01% permanent strain has accrued, the curves have already crossed due to the different post-yield hardening slopes. Thus the differences in the post-yield behavior are enough to dominate the calculated yield stress values.

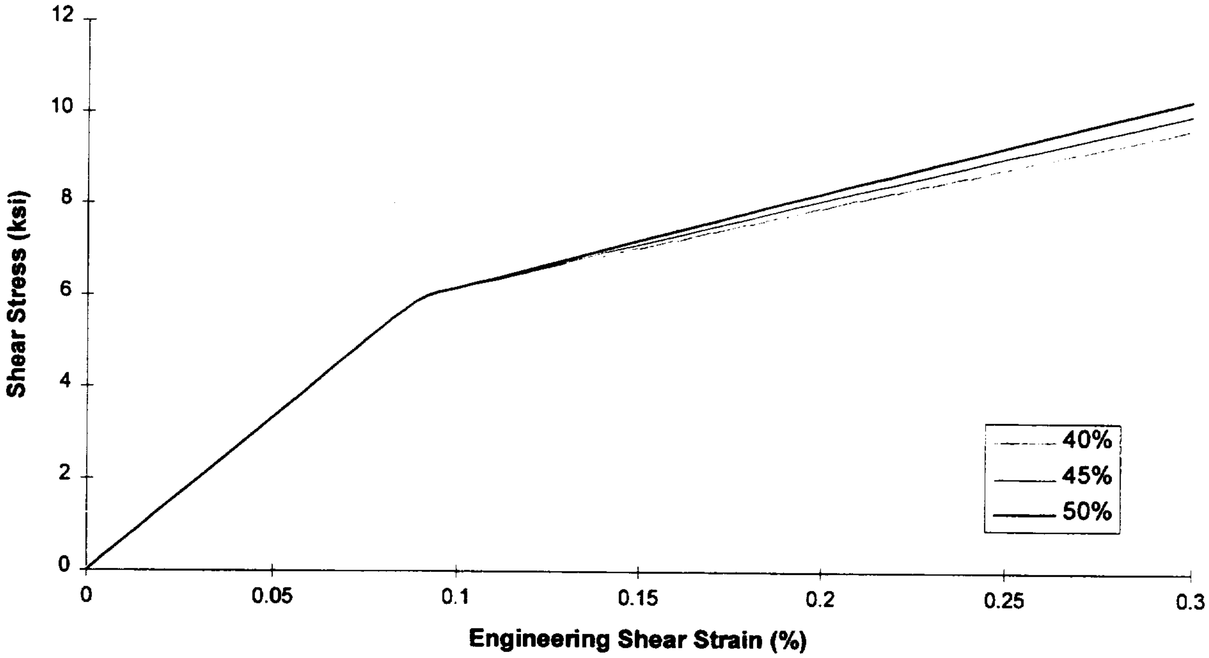

Figure 5.4. Effect of fiber volume fraction on the predicted shear response of 8-harness satin C/Cu as represented by the CMM geometry.

Table 5.5. Effective shear property predictions.

V_f	G (Msi)	k (ksi)	H_{SP} (Msi)
40 %	6.73	6.18	1.76
45 %	6.71	6.21	1.92
50 %	6.68	6.24	2.08

5.3 Effect of Strain Gauge Size and Placement

As discussed in Section 2.4, the size and placement of strain gauges with respect to the reinforcement weave can have a significant effect on the strain readings that are obtained. Of course, average strain readings for the specimen are desired when performing a mechanical test. These are then used, along with the average stress values typically calculated from load cell readings and the specimen cross-section, to generate an average stress-strain curve. However, in an actual mechanical test on an 8-harness satin C/Cu specimen, the strain gauge readings represent local strain values which may be significantly different from the average strain values that are desired. Thus, what is really generated from a mechanical test on 8-harness satin C/Cu is an average stress - local strain curve, where the strain gauge location is unknown.

The model developed for this investigation can be used to examine the effect of strain gauge size and placement. The size of the strain gauges is known, as are the actual weave dimensions. Thus, strain gauge readings can be simulated based on where the gauge is located by recording the strains in the subcells that comprise the layer of copper above the weave subcells (see Figure 5.1). The strains for the subcells located directly under the strain gauge can then be averaged to yield a strain value which would be detected by the strain gauge. These strain readings can be plotted with the average stress applied to the composite to model the stress-strain response measured in practice. It should be noted that the pure matrix layer does not represent an actual free surface to which a strain gauge is bonded, but it does show possible nonuniform strain effects that could occur on such a surface.

Figure 5.5 shows two possible placements for a 10 mm unidirectional strain gauge, and two possible placements for a 3 mm unidirectional strain gauge. Outlines of the strain gauge grid areas are superimposed on a top view of two adjacent TMM unit cells. The shaded squares represent the cross-over subcell positions. The placements of the strain gauges represent the highest and lowest number of cross-over points that may be covered by the gauges, given the gauge dimensions and the weave dimensions. For the 10 mm gauge, the number of cross-over points covered must be between 2.67 and 3.56, while the gauge covers a total of 23.7 subcells. The 3 mm gauge must cover between 0 and 1 cross-over points out of 3.08 total subcells covered.

Figure 5.6(a) shows the predicted tensile response for the woven composite with a fiber volume fraction of 40% for a simulated 10 mm strain gauge covering 2.67 and 3.56 cross-over subcells. Figure 5.6(b) shows the predicted tensile response for a simulated 3 mm strain gauge covering 0 and 1 cross-over subcells. In both figures, the predicted response based on average strains is included for comparison.

For the 10 mm gauge, the effect of the gauge placement is small. This is expected since the gauge covers a large number of subcells, and moving the gauge can only result in a small change in the percentage of these subcells which are above cross-over points. This result is substantiated by the 10 mm strain gauge experimental results which exhibit relatively little

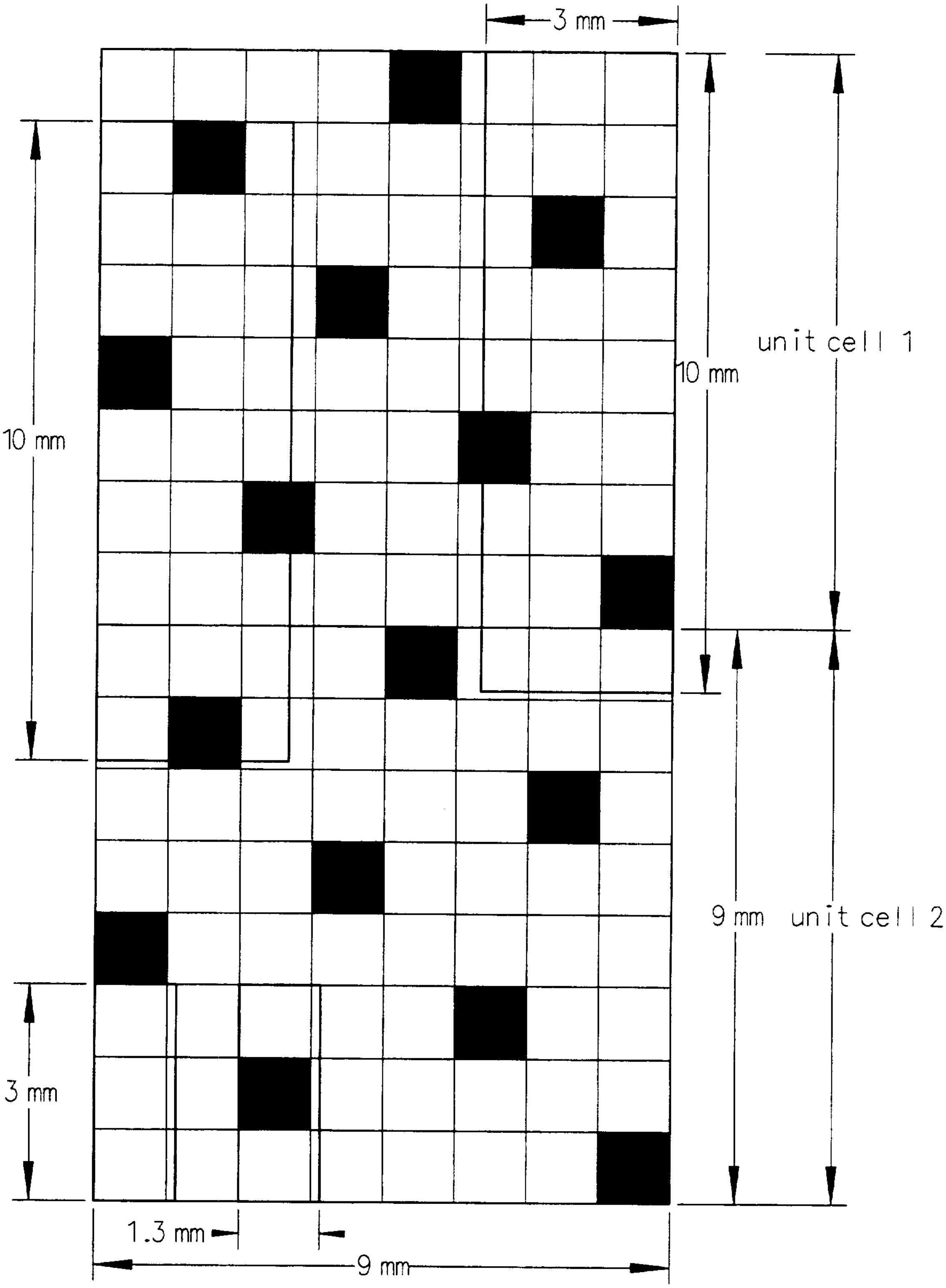

Figure 5.5. Schematic top view of two adjacent TMM unit cells with 10 mm and 3 mm strain gauges superimposed. Shaded subcells indicate cross-over locations.

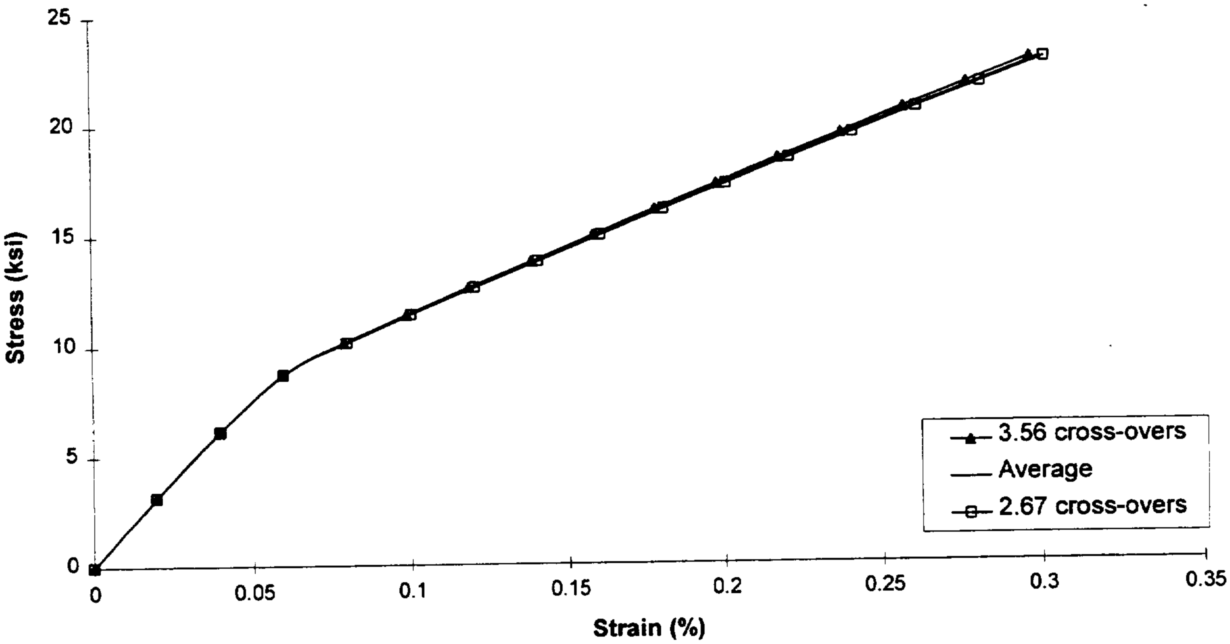

Figure 5.6(a). Effect of 10 mm strain gauge placement on the tensile response of 40% 8-harness satin C/Cu as represented by the TMM geometry.

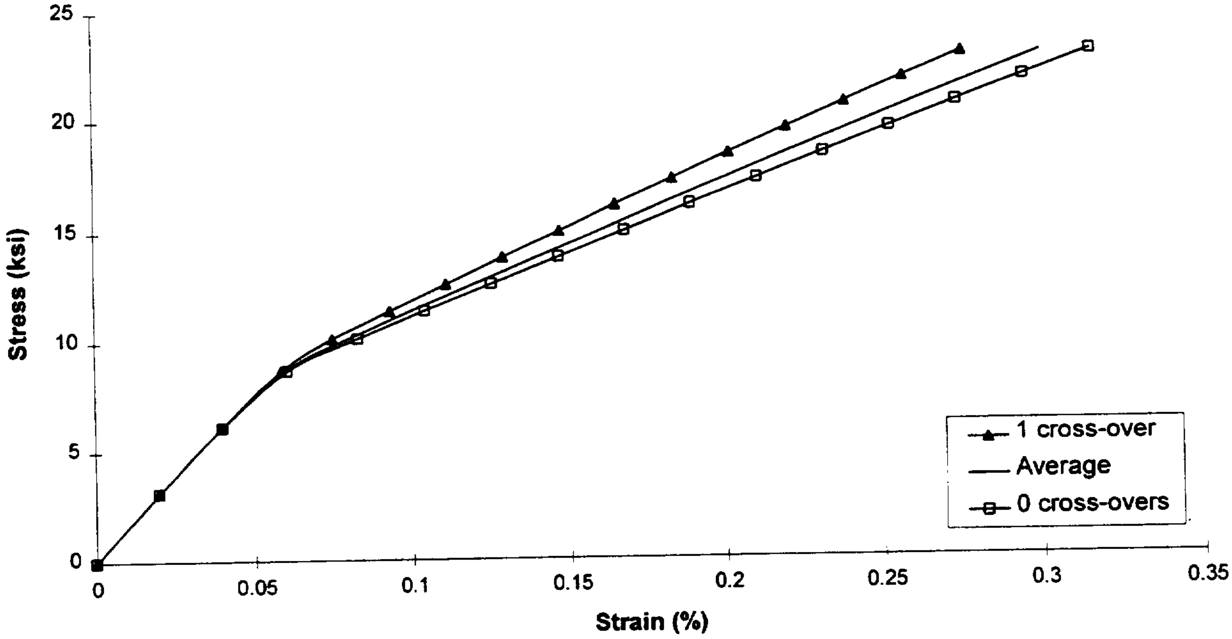

Figure 5.6(b). Effect of 3 mm strain gauge placement on the tensile response of 40% 8-harness satin C/Cu as represented by the TMM geometry.

scatter (see Figure 2.7(b)). For the 3 mm strain gauge, the effect of the gauge placement is small in the elastic region of the predicted tensile response. However, once plastic deformation begins to occur, the effect becomes quite significant. This is expected since the 3 mm gauge covers only a small number of subcells, and thus changing the position from covering one cross-over to zero cross-over points is significant. This effect is also substantiated by the 3 mm strain gauge experimental results which exhibit a large amount of scatter (see Figure 2.7(a)).

The effect of the strain gauge size and placement on the shear response of 8-harness satin C/Cu cannot be examined with GMC-3D because this model lacks shear coupling. This limitation will be discussed in more detail in Chapter 6. Without shear coupling, shear stresses and strains cannot be transmitted across subcell boundaries in the out-of-plane direction unless the subcell materials themselves exhibit coupled elastic behavior (i.e., monoclinic materials). The subcell materials used to construct the TMM unit cell are transversely isotropic and thus exhibit uncoupled elastic behavior. Consequently, when the TMM subcell is subjected to in-plane shear, the shear strain in each layer is constant. Thus, the strain state is identical for each subcell in the pure matrix layer, whether or not it lies above a cross-over point. The lack of shear coupling therefore tends to decrease the effect of the strain gauge placement, even with regard to the tensile response. If shear coupling were included in the model, the effect of the strain gauge placement depicted in Figures 5.6(a) and (b) would likely be greater, closer to the magnitude of the scatter in Figures 2.7(a) and (b).

5.4 Effect of Porosity

5.4.1 Monotonic Tensile Response

As discussed in Section 1.3, the 8-harness satin C/Cu composites fabricated for this investigation exhibited a significant amount of porosity (see Figure 1.10). This porosity was not present in the pure copper matrix regions, but rather within the infiltrated fiber yarns. Microscopic investigation of the composite yarns revealed that this porosity typically occupied approximately 7% to 14% of the volume of the infiltrated fiber yarns.

In order to model the effect of this porosity on the response of the woven composite, the porosity was treated via a reduction in the properties of the copper matrix within the infiltrated fiber yarns. GMC-3D was used to model the tensile response of pure copper with spherical void inclusions. The porous copper was modeled using a total of 343 subcells (7x7x7 cube). The overall volume fraction of the voids was set at 20% and then 40% so that a yarn subcell with a fiber volume fraction of 65% infiltrated with these effective porous copper materials would have effective porosities of 7% and 14%, respectively. Figure 5.7 shows the predicted tensile response of the porous copper. The predicted response of copper with no voids and 10% porosity are plotted for comparison. Clearly, porosity has a major effect on the response of pure copper. Table 5.6 provides a comparison of the effective properties for the porous copper predicted by the model.

The effective properties for the porous copper given in Table 5.6 can be used as input properties for the copper in the infiltrated yarn subcells in the TMM unit cell. Figure 5.8 shows the predicted tensile response of 40% 8-harness satin C/Cu with 7% and 14% porosity in the infiltrated yarn subcells. The predicted response of the fully infiltrated composite is plotted for comparison. Clearly, porosity has a significant effect on the predicted tensile response of the woven composite. The more porous the composite is, the more compliant is the overall tensile stress-strain response. The effect is noticeable even in the elastic region. Table 5.7 provides a numerical comparison of the effective tensile properties of the porous composites as predicted by the model. While the predicted Poisson ratio for the composite changes only slightly as a function of the porosity, the predicted tensile modulus, tensile yield stress, and tensile hardening slope are reduced significantly by increasing fiber yarn porosity.

Table 5.6. Predicted effective properties for porous copper.

void content	E (Msi)	ν	G (Msi)	Y (ksi)	H_{SP} (Msi)
0 %	18.8	0.350	6.96	10.3	1.425
10 %	14.3	0.291	5.55	8.13	1.11
20 %	11.7	0.260	4.62	6.61	0.931
40 %	7.26	0.207	3.01	5.42	0.597

Table 5.7. Predicted effective tensile properties for porous 40% 8-harness satin C/Cu.

yarn porosity	E (Msi)	ν	Y (ksi)	H_{SP} (Msi)
0 %	15.62	0.254	9.83	6.00
7 %	14.44	0.250	8.85	5.26
14 %	13.63	0.250	8.36	4.79

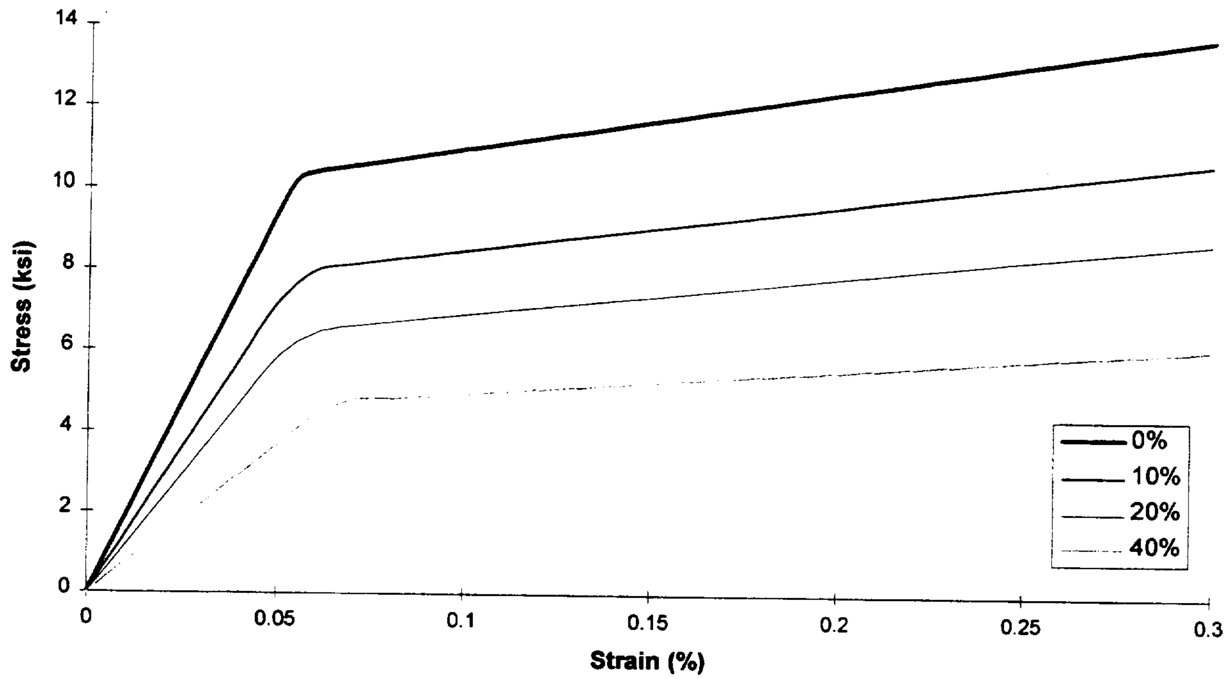

Figure 5.7. Predicted tensile response for porous copper as a function of % porosity.

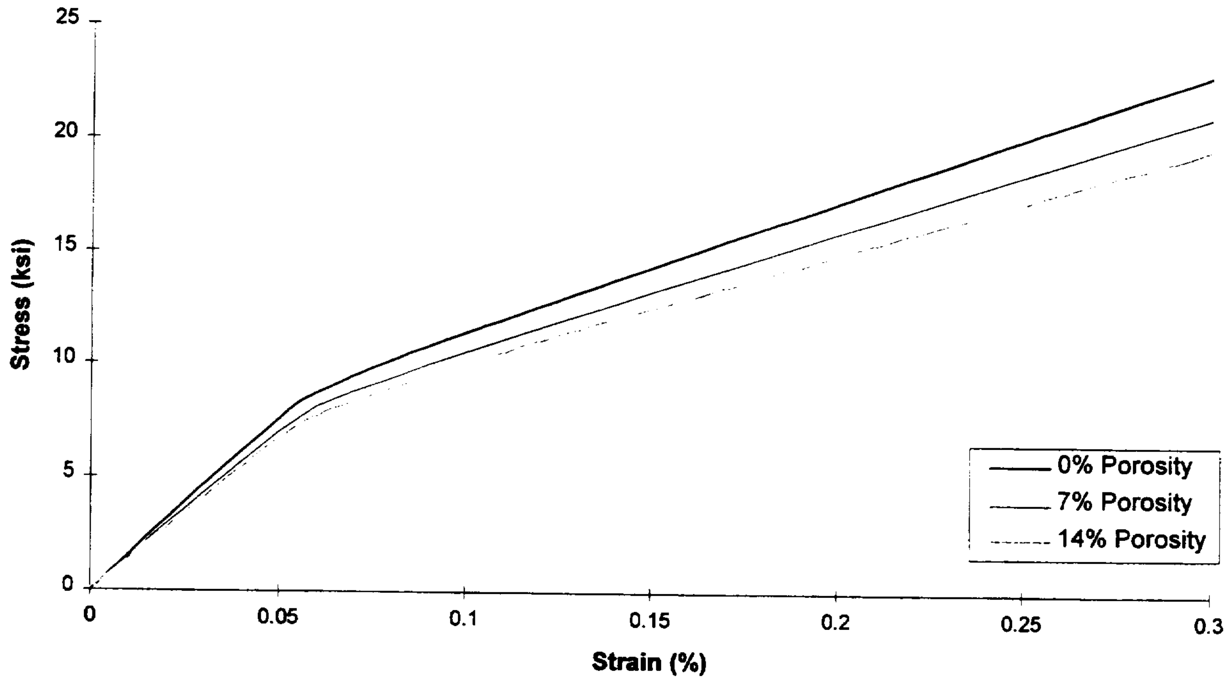

Figure 5.8. Predicted tensile response for porous 8-harness satin C/Cu as a function of yarn subcell % porosity.

5.4.2 Monotonic Shear Response

Figure 5.9 shows the predicted shear response for the porous woven composite. The predicted shear response for the fully infiltrated case is included for comparison. It is clear that porosity has an even greater effect on the shear response of the composite than it did on the tensile response. Table 5.8 provides a numerical comparison of the effective shear properties for the porous composite. The predicted shear modulus, shear yield stress, and shear hardening slope are significantly reduced by increasing fiber yarn porosity.

Table 5.8. Predicted effective shear properties for porous 40% 8-harness satin C/Cu.

yarn porosity	G (Msi)	k (ksi)	H_{SP} (Msi)
0 %	6.73	6.79	1.77
7 %	6.19	5.09	1.46
14 %	5.64	4.23	1.16

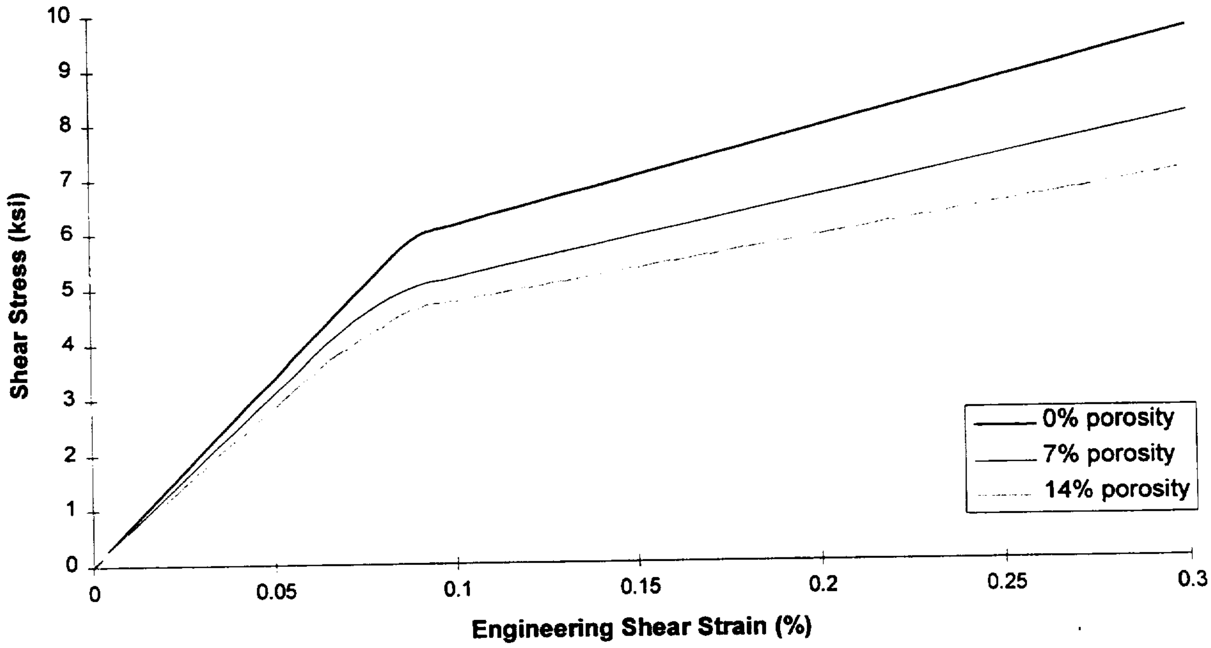

Figure 5.9. Predicted shear response for porous 8-harness satin C/Cu as a function of yarn subcell % porosity.

6. Model-Experiment Correlation

6.1 Monotonic Tensile and Compressive Response

In order to evaluate the effectiveness and accuracy of the analytical model, the predictions of the model were compared with the experimental results for 8-harness satin C/Cu-alloy composites. The model predictions using a fiber volume fraction of 40% were used for this purpose since it represents an approximate average value for the fiber volume fractions of all specimens tested. The model predictions for a composite with fully infiltrated fiber yarns as well as those for fiber yarns with 14% porosity are compared to experimental data. Recall that the specimens tested typically exhibited significant fiber yarn porosity. As mentioned previously, since residual thermal stresses have not been considered, the model predictions are identical for both tension and compression, with opposite signs for the stress and strain values in the case of compression. Thus, the same predicted stress-strain curves are compared to experimental tension stress-strain curves and, with the signs of stresses and strain values reversed, to experimental compression stress-strain curves.

Figures 6.1(a) and (b) compare the model predictions with experimental stress-strain curves in tension and compression, respectively, for 8-harness satin C/Cu-alloy composites. One curve is included in both tension and compression for each matrix alloy type. Curves for both 0° and 90° specimens are included, and not distinguished, since the model predictions are identical for both orientations. The specific curves were chosen based on their average and representative nature.

Since the model is based on perfect bonding between the fiber and the matrix, it is most appropriate to compare the model predictions with C/Cu-Cr experimental results. Comparing these results in Figure 6.1(a) reveals that the model tends to overpredict the stress-strain response of the composite. When porosity in the infiltrated fiber yarns is taken into account, the agreement is improved. However, since additional factors not accounted for by the model, such as residual stresses and fiber-matrix debonding, may act in concert with the porosity, the true extent of improved agreement cannot be reliably judged. It is anticipated that the inclusion of these effects in the model could further improve agreement.

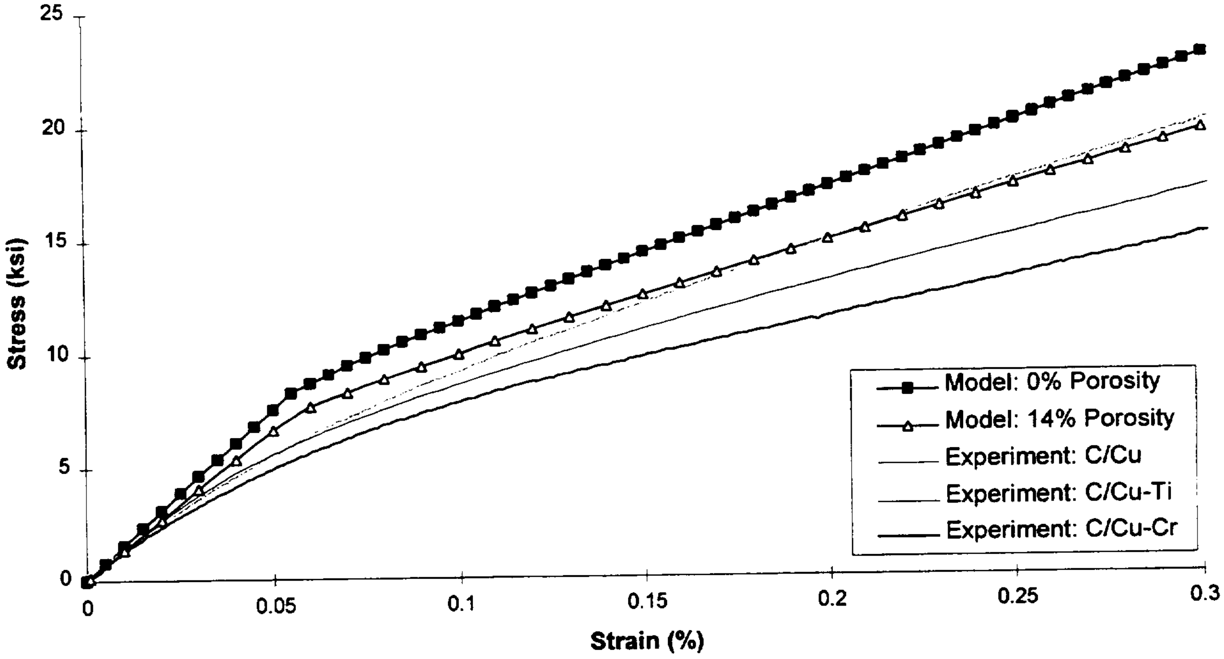

Figure 6.1(a). Comparison of model predictions ($V_f = 40\%$) and experiment for the tensile response of 8-harness satin C/Cu-alloy composites.

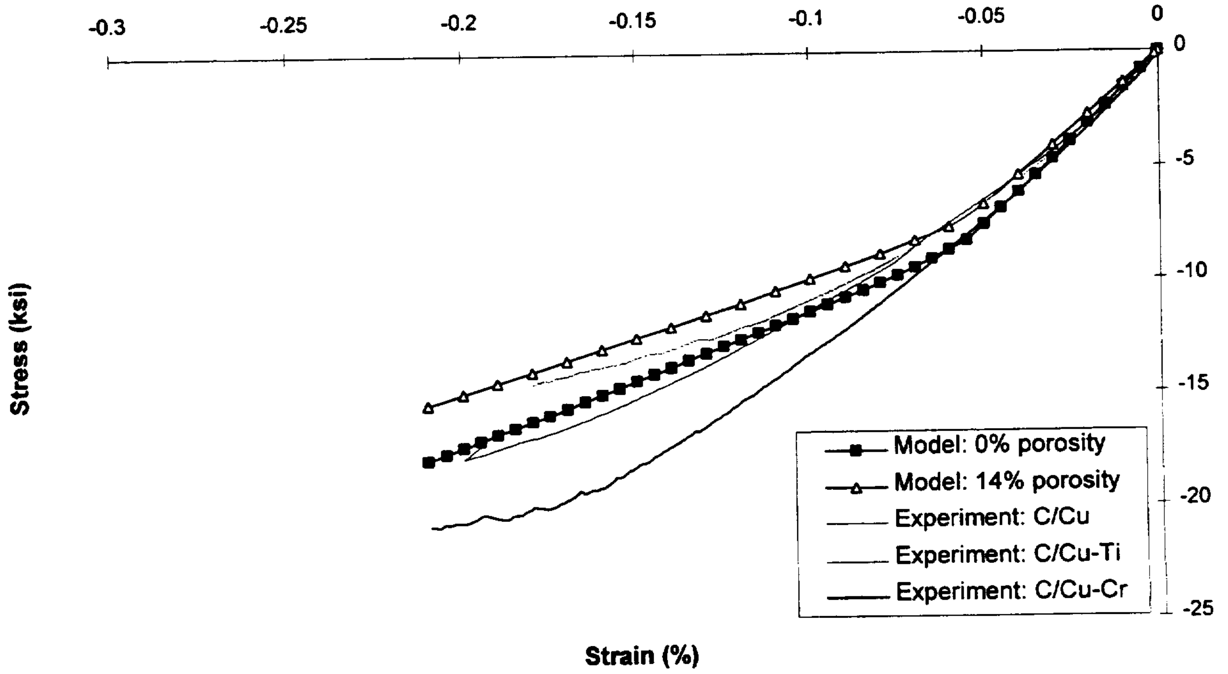

Figure 6.1(b). Comparison of model predictions ($V_f = 40\%$) and experiment for the compressive response of 8-harness satin C/Cu-alloy composites.

Figure 6.1(a) indicates that in the actual tensile tests, yielding initiates at a substantially lower stress than predicted, and the transition to fully plastic behavior is more gradual. This is due in part to the fact that the model is based on the bilinear stress-strain response of the copper matrix. The bilinear nature of the matrix affects the predicted stress-strain response for the composite, causing yielding to be somewhat abrupt. This detracts from the agreement between the model predictions and experiment.

Residual stresses account for a portion of the discrepancy as well. Tensile residual stresses arise in the matrix during fabrication cool-down of C/Cu composites as the low CTE fibers tend to restrict the contraction of the high CTE copper. Thus, the matrix is pre-stressed in tension, and when a tension test is performed, the composite yields at a lower apparent stress. The model cases executed thus far have not included residual stresses and would thus tend to overpredict the tensile yield of the composite as has been observed.

Additional effects which may affect the correlation between the model predictions and experiment in Figure 6.1(a) are microstructural refinement (i.e., using the CMM or DCMM geometries) and lack of shear coupling in the model. Lack of shear coupling in the model might lead to lower predicted matrix stresses in yarn cross-over regions than occur in the actual specimens. The actual specimens would then tend to begin yielding locally at a lower stresses than predicted, as has been observed.

Figure 6.1(b) shows that in compression, the model underpredicts the response of 8-harness satin C/Cu-Cr. The inclusion of porosity lowers the predicted stress-strain curve, and seems to worsen the correlation. However, it is likely that certain factors which are not addressed by the model are interacting to mask the true character of the compressive model-experiment correlation.

First, as was the case in tension, the bilinear nature of the stress-strain response utilized for the copper matrix in the model clearly affects the correlation. The onset of yielding is much more gradual in the experimental stress-strain curve. Second, residual stresses, which are not accounted for in the model predictions, affect the experimental response. During a compressive test, tensile residual stresses would tend to increase (the magnitude of) the apparent yield stress and allow less plastic flow to occur. The model, with no residual stresses would then underpredict the stress-strain curve, as has been observed. Third, the grip constraint effects

Table 6.1. Comparison of model predictions ($V_f = 40\%$) and experiment measurements for the tensile and compressive moduli and yield stresses for 8-harness satin C/Cu-Cr.

		E (Msi)	*Y* (ksi)
Model	0% yarn porosity	15.62	9.83
	14% yarn porosity	13.63	8.36
Experiment (C/Cu-Cr average)	Tension	11.6	4.8
	Compression	16.0	6.9

discussed in Section 3.1.1 tend to increase the apparent overall stiffness of the compressive specimens. The model simulations are for pure uniaxial compression which tends to result in more compliant overall behavior.

The unit cell refinement and lack of shear coupling in the model probably affect the compressive model-experiment correlation as well. Thus, when examining Figure 6.1(b), it is important to understand that many different effects are acting in concert. If all the significant effects were accounted for in the model, both predicted stress-strain curves in Figure 6.1(b) might fall above the experimental curves, with the inclusion of porosity improving the agreement. This is, of course, speculation. To gain the required insight into the true nature of the effects, they must be included in the micromechanical model.

Table 6.1 provides a comparison of the tensile and compressive moduli and yield stresses predicted by the model and the average experimental values for C/Cu-Cr. The differences between the experimental tensile and compressive values underscore the need to include residual stresses and the grip constraint effect in the model. The table indicates that the predicted moduli for the composite are reasonable, falling between the experimental tensile and compressive values. The yield stresses, on the other hand, are significantly overpredicted by the model. Thus, it appears that the predicted yield and post-yield behavior of the composite has the largest room for improvement as additional features are added to the model.

6.2 Monotonic Shear Response

The predictions of the model for the shear response of 8-harness satin C/Cu can be compared to experimental data as well. Figure 6.2 provides this comparison. The experimental

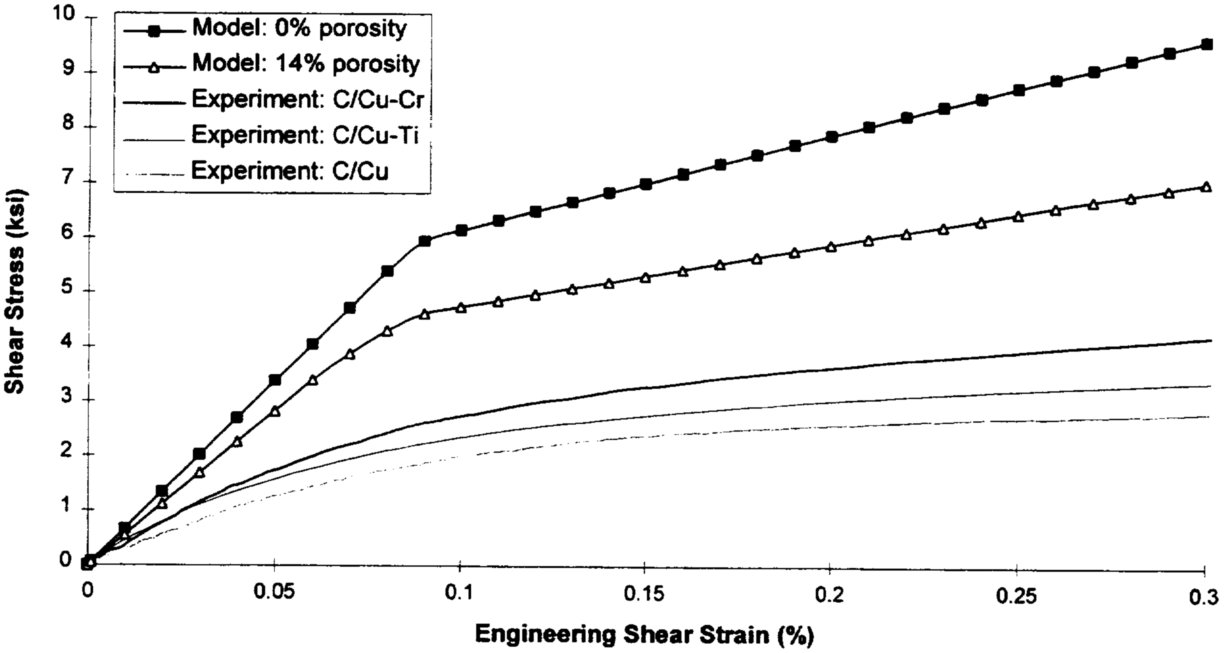

Figure 6.2. Comparison of model predictions ($V_f = 40\%$) and experiment for the shear response of 8-harness satin C/Cu-alloy composites.

shear response of one specimen of each matrix alloy type is included, along with model predictions for the fully infiltrated composite and for the composite with 14% yarn porosity. As in the case of tension and compression, the specimen orientation (0° or 90°) is superfluous. Clearly the model significantly overpredicts the shear stress-strain response of the composite. Including yarn porosity in the model reduces the discrepancy somewhat, but the agreement is still poor. Table 6.2 indicates that the predicted shear moduli and shear yield stress for the composite are higher than the average experimental values for C/Cu-Cr by nearly a factor of two.

The poor agreement between the model predictions and experimental results for the shear response of 8-harness satin C/Cu may be caused by several factors. One such factor is poor bonding. Unlike the experimental tensile response, the experimental shear response follows the expected trend based on the traditional poor bonding argument. Namely, superior fiber-matrix bonding leads to stiffer overall response. Thus, as shown in Figure 6.2, better bonding raises the shear stress-strain curves towards the predicted response. The model predictions are for composites with perfect fiber-matrix bonding, and thus the predicted stress-strain curves would

Table 6.2. Comparison of model predictions ($V_f = 40\%$) and experiment measurements for the shear modulus and yield stress for 8-harness satin C/Cu-alloy composites.

		G (Msi)	*k* (ksi)
Model	0% yarn porosity	6.73	6.79
	14% yarn porosity	5.64	4.23
Experiment	(C/Cu-Cr average)	3.7	2.3

be lowered by including poor bonding in the model. The effect of the fiber-matrix bonding was most pronounced on the shear response of the composite, thus, it is not unreasonable to expect the bonding to have an important effect on the model-experiment correlation.

Another factor that could contribute to the discrepancy between the observed and predicted shear response is the lack of shear coupling in the model. When the composite is subjected to shear loading as opposed to normal loading, the transfer of stresses via shear becomes even more important. Normal stresses in the shear specimens arise only as a result of this transfer of stresses, since the global state of stress is nearly pure shear. GMC-3D lacks the ability to model this transfer of stress via shear, as well as the coupling between normal and shear stresses and strains. Recall that the model predicts that the states of stress and strain in the pure copper layers are identical for each subcell, regardless of the location with respect to yarn cross-over points, when the composite is subjected to shear loading. Clearly, this is unrealistic. Hence, the model lacks the mechanism of stress transfer that probably dominates the shear response of the composite. Stress concentrations from shear coupling that occur in the real shear specimens would be expected to give rise to a more compliant elastic response, yielding at lower stresses, and a more compliant post-yield response than the model predicts. Thus, it is possible that the lack of shear coupling in the model is an important factor contributing to the poor model-experiment correlation in shear.

Other contributions to the discrepancy include the lack of residual stresses in the model, the coarse refinement of the composite microstructure represented by the TMM geometry, local finite deformation associated with large rotations of the weave fiber yarns, and an inhomogeneous state of shear occurring in the test specimens. The two former contributions would be expected to affect the shear response as they do the normal response. The latter two contribution are probably more important for shear. The shear loading to which the Iosipescu specimen is subjected tends to rotate the reinforcement weave. This is not the case for normal loading. At moderate to high strains, this yarn rotation may give rise to finite strains in local regions of the composite which the model cannot predict. This would tend to make the experimental shear response more compliant and add to the discrepancy with the model. As was the case for tension and compression, identified as well as yet unidentified effects contribute to the discrepancy. Taking these effects into account within the model would be expected to improve the agreement as well as allow a better understanding of each effect.

7. Conclusions

The results of an extensive experimental characterization and a preliminary micromechanical modeling effort for 8-harness satin C/Cu composites have been presented. Tension, compression, combined tension-compression, and Iosipescu shear tests were used for the experimental characterization of the material, while the GMC-3D micromechanics model was used to predict the elastoplastic tensile, compressive, and shear responses of the composite. Significant conclusions are grouped into those pertaining to experimental aspects of the investigation and those pertaining to the modeling effort. These are summarized below.

Experimental Findings

1. The tensile response of the composite is typified by the onset of gradual yielding at low stresses (compared to the bulk copper matrix), and stiffening at high strains. The extent of the stiffening depends on the matrix alloy, with the more highly alloyed matrices resulting in more stiffening. It is suspected that this stiffening is associated with the straightening of the fiber yarns of the reinforcement weave. At lower strains, the tendency of the yarns to straighten may give rise to stress concentrations in the regions of yarn cross-over points which bring about the early yielding, and greatly affect the overall tensile response of the composite. Tensile failure occurred abruptly via fracture of the matrix, but the reinforcing fibers were left intact across the failure surface.

2. In compression, the onset of plastic strain in the composite was more gradual compared to tension. No stiffening occurred, and failure occurred at much lower stresses and strains (compared to tension) via a gradual micro-buckling mechanism. While gross buckling of the compression specimens was prevented by the test fixture, micro-buckling, consisting of bowing of the weave and copper layers, was permitted. This bowing mechanism seems to have an effect on the inelastic compressive behavior of the composite and may be partly responsible for the major differences observed between the behavior of the composite in compression and tension. Other factors contributing to the observed differences between tension and compression are

residual stresses due to cool-down from the fabrication temperature of the composite and the constraint effect caused by the test fixture used for the compressive tests.

3. Cyclic normal tests (tension, compression, combined tension-compression) revealed a great deal of hysteretic behavior by the composite. By examining cyclic loading and unloading elastic modulus data, damage was ruled out as a major hysteretic mechanism for the composite. Examining the composite yield surface size and position using the newly developed "bedpin" diagram revealed that the composite experiences a large amount of kinematic hardening and relatively little isotropic hardening during plastic deformation. This indicates that the hysteretic behavior is due in part to kinematic hardening. The largest hysteresis loops were observed for composites with the poorest fiber-matrix bonding. This suggests that frictional effects caused by sliding of debonded fibers may contribute to the hysteretic behavior as well.

4. The shear response of the composite was dominated by the matrix and characterized by large strains. Shear yield stresses were low, shear post-yield slopes were low, and "failure" was accompanied by limited matrix cracking, limited local micro-buckling, and large amounts of fiber yarn rotation in the Iosipescu specimen test section. Failure shear stresses for the composite were achieved, but due to the nature of the specimen and the Iosipescu test fixture, "failure", as in fracture of the specimen, was not achieved. Cyclic shear tests revealed that the composite exhibits much less hysteresis in shear compared to normal loading. This indicates that the composite experiences less kinematic hardening in shear, and thus the kinematic hardening present during normal loading is most likely due to constraint provided by fibers oriented longitudinally to the loading direction.

5. A trend based on matrix alloy type was evident in the tensile, compressive, and shear responses of the composite, as well as in the average elastic moduli, average yield stresses, and average ultimate strengths of the specimens tested. The experimental data obtained from compression and shear tests tend to confirm the previously drawn conclusion (Ellis, 1992; DeVincent, 1995) that the addition of small amounts of Cr and Ti to the copper matrix of 8-harness satin C/Cu improves fiber-matrix bonding. The C/Cu-Cr composite has the best

interfacial bonding, followed by C/Cu-Ti, and finally by C/Cu. In shear, the expected trend was observed, with the C/Cu-Cr composite exhibiting the highest modulus, yield stress, and ultimate strength. In compression, the expected trend was also observed for the yield stress and ultimate strength, but the opposite trend was observed for the modulus. In tension, however, the opposite of the expected trend was observed for modulus, yield stress, and ultimate strength. Future work will attempt to predict the observed trends via more detailed micromechanical modeling.

6. The significant amount of scatter in the experimental results is partly due to the large size of the 8-harness satin weave repeating unit cell. Using a larger strain gauge (10 mm as opposed to 3 mm) decreased the amount of scatter in the measured results significantly. The large amount of scatter associated with small strain gauges, coupled with the inherently small magnitude of transverse strains, made obtaining accurate Poisson ratios (from rosette data) for the composite impossible.

7. The absolute moduli, yield stresses, and ultimate strengths of 8-harness satin C/Cu-alloy composites are inferior to the corresponding quantities for pure copper. However, if the specific properties (properties divided by density) are compared, the values for the composite are competitive. Note that these are in-plane properties. Through-thickness properties of the woven composite (such as blunt impact resistance) are expected to be far superior to those of pure copper.

Modeling Conclusions

1. Three distinct geometrical models were developed representing the true repeating unit cell for an 8-harness satin woven composite. The effect of refining the geometry from its simplest true representation to the next level results in an increase in the number of subcells from 192 (TMM geometry) to 1280 (CMM and DCMM geometries). Elastic results predicted by the model for both levels of refinement are nearly identical for 8-harness satin C/Cu. The refinement is expected to have a significant effect on the predicted plastic response of the composite, but such cases currently cannot be executed for the more complex geometries due to computer limitations.

2. Increasing the overall fiber volume fraction of the composite while keeping the yarn fiber volume fraction constant decreases the predicted tensile, compressive, and shear moduli. This is due to the lower transverse tensile modulus and axial shear modulus of the carbon fiber compared to the copper matrix which allows the pure copper layers of the unit cell to have a greater effect. The predicted tensile, compressive, and shear post-yield hardening slopes, however, increase with increasing overall fiber volume fraction. This is because the copper matrix becomes much more compliant once yielding occurs.

3. The local variations in measured tensile and compressive strain values caused by the size and placement of strain gauges with respect to the reinforcement weave are qualitatively predicted by the model. As was also observed in the experimental data, readings from a 3 mm strain gauge produced greater variations in the stress-strain response than those from a 10 mm strain gauge.

4. Porosity, which is known to exist within the infiltrated fiber yarns of the 8-harness satin C/Cu reinforcement weave, has a significant effect on the predicted tensile, compressive, and shear response of the composite. Porosity of 14% in the infiltrated fiber yarns reduced the composite's predicted in-plane tensile modulus by 13%, yield stress by 15%, and post-yield hardening slope by 20%. Reduction of the composite in-plane shear properties due to the porosity are even more severe.

5. The model overpredicts the tensile response of 8-harness satin C/Cu and underpredicts the compressive response. Most of the disagreement is due to differences in the predicted and experimental yield and post-yield behavior of the composite. Fiber-matrix debonding, residual stresses in the matrix, a biaxial stress state due to grip constraint effects (in compression tests), unit cell microstructural refinement, and the model's lack of shear coupling may affect the model-experiment correlation.

6. The model substantially overpredicts the shear response of 8-harness satin C/Cu. The model's inability to account for poor fiber-matrix bonding and shear coupling may play major roles in this discrepancy. The effect of fiber-matrix bonding was greatest on the shear response of the

composite. Hence, modeling the bond as perfect, as was done, could contribute to the poor correlation. In addition, when the composite is subjected to global shear loading, shear coupling may become important. The model cannot simulate the transfer of shear stresses between layers, and no global normal stresses are present to be transferred. The result is that each layer responds largely independently, and weave induced stress-concentrations, which may influence the experimental shear response, are completely absent in the model. Gross rotation of the fiber yarns, which occurs at moderate to high shear strains, is also neglected by the model, and probably contributes to the discrepancies at the higher strains.

8. Future Work

Although analysis of the experimental data will continue, future work on the characterization of 8-harness satin C/Cu will focus on micromechanical modeling. The current model will be extended to include factors and to simulate phenomena that affect the measured and predicted mechanical response of 8-harness satin C/Cu composites. The first step will be to employ the more refined geometric models (CMM and DCMM) for the composite. Current computational facilities available are not sufficient to execute the model utilizing these complex geometries. An effort is underway to reformulate GMC-3D to reduce the number of unknown variables (equivalent to reducing the size of the **A** and **D** matrices in equation (4.10)) by taking advantage of traction constancy through subcells in certain directions.

The current study has demonstrated that fiber-matrix interfacial bonding has major effects on the mechanical response of C/Cu composites. In order to improve the accuracy of the model predictions, it is necessary to account for the poor interfacial bonding. This will be accomplished by employing a version of the original method of cells which incorporates debonding to represent the behavior of the infiltrated fiber yarns.

Differences between experimental tension and compression results observed in this investigation have been attributed in part to residual stresses in the matrix and a biaxial state of stress in compression caused by grip constraint effects. Both of these factors will be addressed in the modeling effort. Cyclic loading capabilities will be incorporated into the model to allow a simulated cool-down thermal loading cycle prior to imposing the mechanical loading. Cyclic capabilities will also allow simulation of the cyclic tensile, compressive, and shear tests, as well as the combined tests. The grip constraint effects will be modeled by imposing a biaxial loading in the simulation as opposed to uniaxial compressive loading, as has been done thus far. The particular biaxial loading to best simulate the grip constraint effect is to be determined.

Another direction towards which this investigation points is the inclusion of shear coupling in the model. These results have indicated that the transfer of stresses via shear, as well as shear stresses and strains induced by normal stresses and strains, may be important mechanisms governing the local, as well as global, response of 8-harness satin C/Cu. GMC-3D lacks shear coupling, and thus its ability to accurately model response of 8-harness satin C/Cu might be improved by including it.

Recently, a higher order theory based on the same principals as the original method of cells and GMC-3D has been developed by Aboudi *et al.* (1995). In this theory, the displacement field in each subcell (see equation (4.1)) is permitted to vary quadratically with each local coordinate, rather than just linearly (as is the case in GMC-3D). This higher order displacement field allows transfer of shear stresses across subcell interfaces since certain higher order terms in the displacement field are retained when the continuity conditions are enforced, where the first order terms are lost. The higher order theory has been utilized to model functionally graded materials, and thus has been dubbed the higher order theory for functionally graded materials (HOTFGM). Incorporation of the original method of cells into HOTFGM represents one possible method for the inclusion of shear coupling in a model for woven composites.

References

Aboudi, J. (1987) "Closed Form Constitutive Equations for Metal Matrix Composites" International Journal of Engineering Science. Vol. 25, pp. 1229-1240.

Aboudi, J. (1989) "Micromechanical Analysis of Composites by the Method of Cells" Applied Mechanics Reviews. Vol. 42, pp. 193-221.

Aboudi, J. (1994) "Micromechanical Analysis of Thermo-Inelastic Multiphase Short-Fiber Composites" NASA-CR-195290.

Aboudi, J., Pindera, M.-J., and Arnold, S.M. (1995) "Thermo-Inelastic Response of Functionally Graded Composites" International Journal of Solids Structures. Vol. 32, pp. 1675-1710.

Adams, D.F. and Walrath, D.E. (1987) "In-Plane and Interlaminar Iosipescu Shear Properties of Various Graphite Fabric/Epoxy Laminates" Journal of Composites Technology and Research. Vol. 9, No. 3, pp. 88-94.

Arnold, S.M., Pindera, M.-J., and Wilt, T.E. (1995) "Influence of Fiber Architecture on the Elastic and Inelastic Response of Metal Matrix Composites" NASA-TM-106705.

Bednarcyk, B.A. and Pindera, M.-J. (1994) "Micromechanical Modeling of the Thermal Expansion of Graphite/Copper Composites With Nonuniform Microstructure" NASA-CR-195368.

Brayshaw, J.B. (1994) "Consistent Formulation of the Method of Cells Micromechanics Model for Transversely Isotropic Composites" Ph.D. Dissertation, University of Virginia.

Chou, T.-W. and Ishikawa, T. (1989) "Analysis and Modeling of Two-Dimensional Fabric Composites" Textile Structural Composites. T.-W. Chou. and F.K. Ko eds., Elsevier: New York, pp. 209-264.

Chou, T.-W., McCullough, R.L., and Pipes, R.B. (1986) "Composites" Scientific American. October, pp. 193-203.

Dasgupta, A. Agarwal, R.K, and Bhandarkar, S.M. (1996) "Three-Dimensional Modeling of Woven-Fabric Composites for Effective Thermo-Mechanical and Thermal Properties" Composites Science and Technology. Vol. 56, pp. 209-223.

Dasgupta, A. and Bhandarkar, S.M. (1994) "Effective Thermomechanical Behavior of Plain-Weave Fabric-Reinforced Composites Using Homogenization Theory" Journal of Engineering Materials and Technology. Vol. 116, pp. 99-105.

DeVincent, S.M. (1995) "Interfacial Effects on the Thermal and Mechanical Properties of Graphite/Copper Composites" NASA-CR-198370.

Ellis, D.L. (1992) "Properties of Graphite Fiber Reinforced Copper Matrix Composites for Space Power Applications" NASA-CR-191026.

Fleck, N.A., Jelf, P.M., and Curtis, P.T. (1995) "Compressive Failure of Laminated and Woven Composites" Journal of Composites Technology and Research. Vol. 17, No. 3, pp. 212-220.

Fujii, T. and Lin, F. (1995) "Fatigue Behavior of a Plain-Woven Glass Fabric Laminate under Tension/Torsion Biaxial Loading" Journal of Composite Materials. Vol. 29, No. 5, pp. 573-590.

Fujii, T., Shiina, T, and Okubo, K. (1994) "Fatigue Notch Sensitivity of Glass Woven Fabric Composites Having a Circular Hole under Tension/Torsion Biaxial Loading" Journal of Composite Materials. Vol. 28, No. 3, pp. 234-251.

Fujita, A. *et al.* (1993) "Tensile Properties of Carbon Fiber Triaxial Woven Fabric Composites" Journal of Composite. Vol. 27, No. 15, pp. 1428-1442.

Gause, L.W. and Alper, J.M. (1987) "Structural Properties of Braided Graphite/Epoxy Composites" Journal of Composites Technology and Research. Vol. 9, No. 4, pp. 141-150.

Glaessgen, E.H., Pastore, C.M., Griffin, O.H., and Birger, A. (1996) "Geometrical and Finite Element Modelling of Textile Composites" Composites: Part B. Vol. 27B, pp. 43-50.

Goldberg, R.K. and Hopkins, D.A. (1995) "Further Applications of the Boundary Element Method in the Micromechanical Modeling of Woven Composites" Proc. HITEMP Review 1995. Vol. 3.

Gong, J.C. and Sankar, B.V. (1991) "Impact Properties of Three-Dimensional Braided Graphite/Epoxy Composites" Journal of Composite Materials. Vol. 25, pp. 715-731.

Harding, J. (1993) "Effect of Strain Rate and Specimen Geometry on the Compressive Strength of Woven Glass-Reinforced Epoxy Laminates" Composites. Vol. 24, No. 4, pp. 323-332.

Ifju, P.G., Masters, J.E., and Jackson, W.C. (1995) "The Use of Moiré Interferometry as an Aid to Standard Test-Method Development for Textile Composites" Composites Science and Technology. Vol. 53, pp. 155-163.

Jackson, W.C. and Ifju, P.G. (1994) "Through-the-Thickness Tensile Strength of Textile Composites" NASA-TM-109115.

Kabelka, J. (1980) "Thermal Expansion of Composites with Canvas-Type Reinforcement and Polymer Matrix" Proc. 3rd International Conference on Composite Materials. pp. 770-782.

Kabelka, J. (1984) "Prediction of the Thermal Properties of Fibre-Resin Composites" Developments in Reinforced Plastics - 3. G. Pritchard ed., Elsevier: London, pp. 167-202.

Kang, T.J. and Lee, S.H. (1994) "Effect of Stitching on the Mechanical and Impact Properties of Woven Laminate Composites" Journal of Composite Materials. Vol. 28, No. 16, pp. 1574-1587.

Karayaka, M. and Kurath, P. (1994) "Deformation and Failure Behavior of Woven Composite Laminates" Journal of Engineering Materials and Technology. Vol. 116, pp. 222-232.

Kriz, R.D. (1985) "Influence of Damage on Mechanical Properties of Woven Composites at Low Temperatures" Journal of Composites Technology and Research. Vol. 7, No. 2, pp. 55-58.

Lin, M. and Pindera, M.-J. (1988) "Elastoplastic Response of Unidirectional Graphite/Aluminum Under Combined Tension-Compression Cyclic Loading" CCMS-88-01, Virginia Polytechnic Institute and State University.

Mendelson, A. (1983) Plasticity: Theory and Application. Krieger Publishing Co.: Malabar, Florida.

Miyano, Y. *et al.* (1994) "Loading Rate and Temperature Dependence on Flexural Fatigue Behavior of a Satin Woven CFRP Laminate" Journal of Composite Materials. Vol. 28, No. 13, pp. 1250-1260.

Miller, E. (1968) Textiles Properties and Behaviour. B T Batsford Ltd: London.

Naik, N.K. and Ganesh, V.K. (1992) "Prediction of On-Axes Elastic Properties of Plain Weave Fabric Composites" Composites Science and Technology. Vol. 45, pp. 135-152.

Pindera, M.-J. and Herakovich, C.T. (1985) "Shear Characterization of Unidirectional Composites with the Off-Axis Tension Test" Experimental Mechanics. Vol. 26, pp. 103-112.

Pindera, M.-J., Choksi, G., Hidde, J.S., and Herakovich, C.T. (1987) "A Methodology for Accurate Shear Characterization of Unidirectional Composites" Journal of Composite Materials. Vol. 21, pp. 1164-1184.

Reifsnider, K.L. and Mirzadeh, F. (1988) "Compressive Strength and Mode of Failure of 8H Celion 3000/PMR15 Woven Composite Material" Journal of Composites Technology and Research. Vol. 10, No. 4, pp. 156-164.

Rodriguez, J. *et al.* (1996) "High Strain Rate Properties of Aramid and Polyethylene Woven Fabric Composites" Composites: Part B. Vol. 27B, pp. 147-154.

Whitcomb, J, Woo, K., and Gundapaneni, S. (1992) "Macro Finite Element Analysis of Textile Composites" Proc. 6th Japan-U.S. Conference on Composite Materials. pp. 541-550.

Whitcomb, J. and Srirengan, K. (1996) "Effect of Various Approximations on Predicted Progressive Failure in Plain Weave Composites" Composite Structures. Vol. 34, pp. 13-20.

Williams, T.O. (1995) "Inelastic Microstructural Modeling of Metal Matrix Composites" Ph.D. Dissertation, University of Virginia.

Williams, T.O. and Pindera, M.-J. (1994) "Multiple Concentric Cylinder Model (MCCM) User's Guide" NASA-CR-195299.

Wilt, T.E. (1995) "On the Finite Element Implementation of the Generalized Method of Cells Micromechanics Constitutive Model" NASA-CR-195451.

Xiao, J and Bathias, C. (1994) "Fatigue Damage and Fracture Mechanism of Notched Woven Laminates" Journal of Composite Materials. Vol. 28, No. 12, pp. 1127-1139.

Zhou, G. and Davies, G.A.O. (1995) "Characterization of Thick Glass Woven Roving/Polyester Laminates: 1. Tension, Compression and Shear" Composites. Vol. 26, No. 8, pp. 579-586.

Appendix

A.1 Layouts according to which test specimens were cut from plates

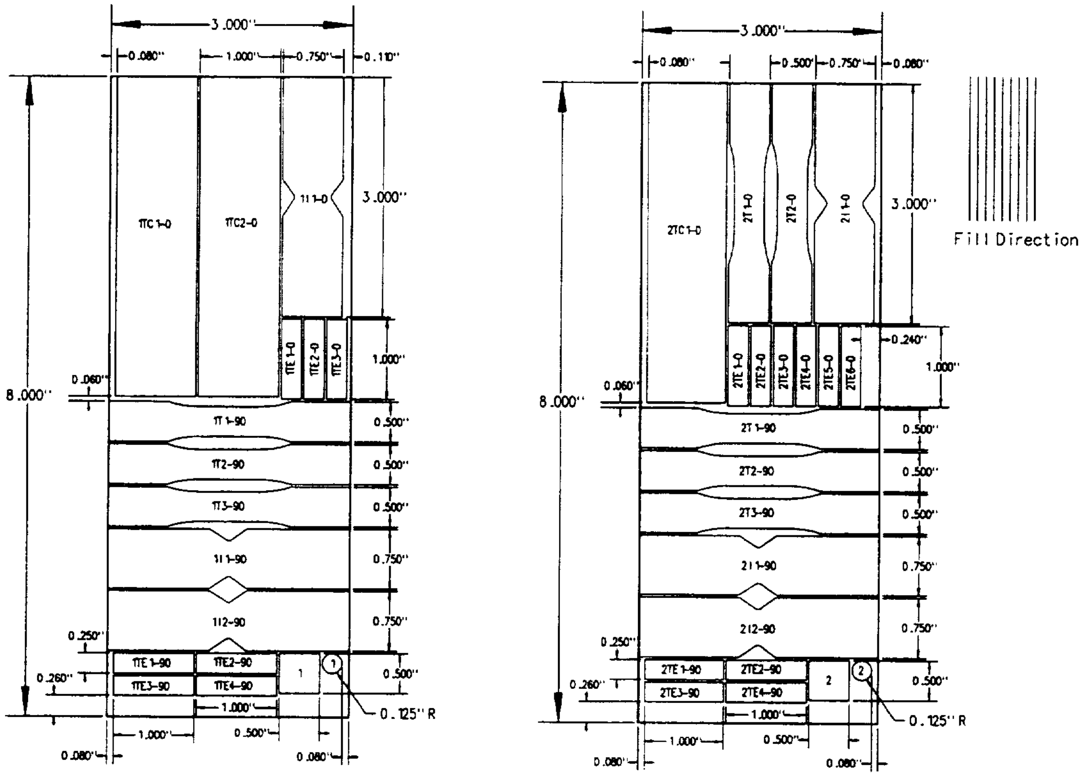

A.2 Poisson plots for 90° C/Cu specimens. Note large amount of scatter.

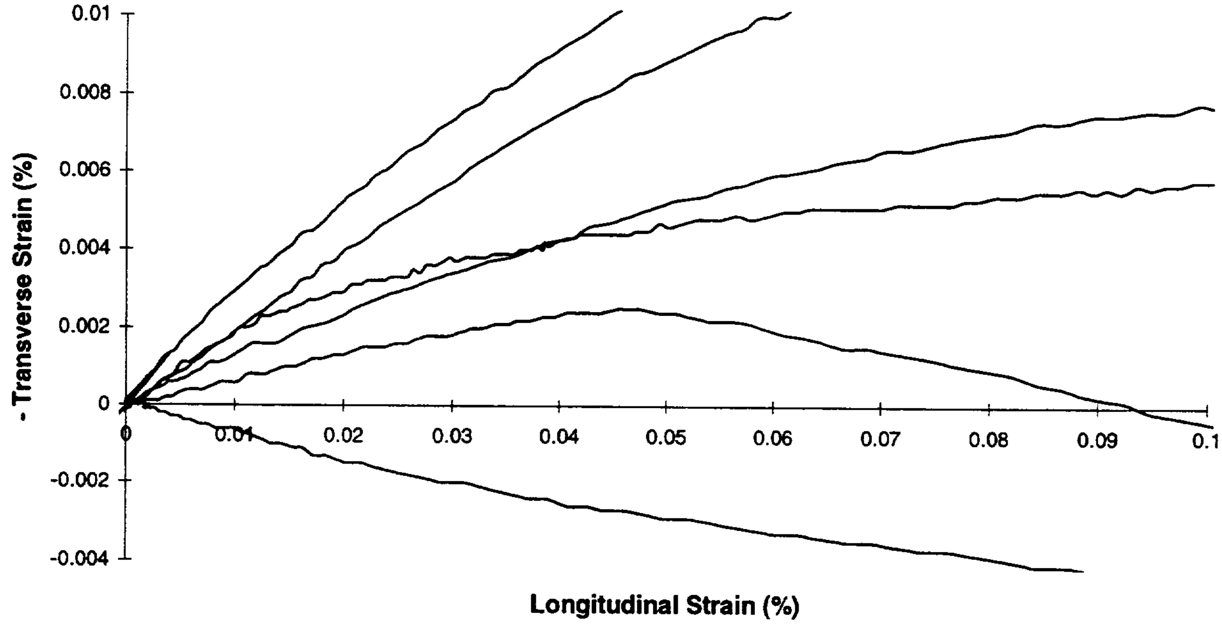

A.3 Method of Cells Equations

$$Vb_{11} = v_{11}C_{11}^{f} + C_{11}^{m}(v_{12} + v_{21} + v_{22}) + \left(C_{12}^{m} - C_{12}^{f}\right)(Q_2 + Q_3)$$

$$Vb_{12} = \frac{h}{h_1}\left(C_{12}^{m}v_{12} + Q_1C_{22}^{m} + Q_3C_{23}^{m}\right) + \frac{h}{h_2}\left(C_{12}^{m}v_{21} + Q_2C_{22}^{m} + Q_4C_{23}^{m}\right)$$

$$Vb_{13} = \frac{l}{l_1}\left(C_{12}^{m}v_{21} + Q_2C_{23}^{m} + Q_4C_{22}^{m}\right) + \frac{l}{l_2}\left(C_{12}^{m}v_{12} + Q_1C_{23}^{m} + Q_3C_{22}^{m}\right)$$

$$Vb_{22} = \frac{h}{h_1}\left[C_{22}^{m}(v_{12} + Q_1') + Q_3'C_{23}^{m}\right] + \frac{h}{h_2}\left[C_{22}^{m}(v_{21} + Q_2') + Q_4'C_{23}^{m}\right]$$

$$Vb_{23} = \frac{l}{l_1}\left[C_{23}^{m}(v_{21} + Q_2') + Q_4'C_{22}^{m}\right] + \frac{l}{l_2}\left[C_{23}^{m}(v_{12} + Q_1') + Q_3'C_{22}^{m}\right]$$

$$Vb_{33} = \frac{l}{l_1}\left[C_{22}^{m}(v_{21} + Q_4'') + Q_2''\,C_{23}^{m}\right] + \frac{l}{l_2}\left[C_{22}^{m}(v_{12} + Q_3'') + Q_1''C_{23}^{m}\right]$$

$$Vb_{44} = \frac{C_{44}^{m}\left\{C_{44}^{f}\left[h(v_{11} + v_{21}) + h_2(v_{12} + v_{22})\right] + C_{44}^{m}\,h_1(v_{12} + v_{22})\right\}}{h_1C_{44}^{m} + h_2C_{44}^{f}}$$

$$Vb_{55} = \frac{C_{55}^{m}\left\{C_{55}^{f}\left[l(v_{11} + v_{12}) + l_2(v_{21} + v_{22})\right] + C_{55}^{m}\,l_1(v_{21} + v_{22})\right\}}{l_1C_{55}^{m} + l_2C_{55}^{f}}$$

$$b_{66} = \frac{C_{66}^{f}\,C_{66}^{m}\,h\,l}{h_1\,l_1\,C_{66}^{m} + (h_1\,l_2 + h_2\,l_1 + h_2\,l_2)C_{66}^{f}}$$

$$\begin{aligned}VH_{11} = {} & Q_1\left(C_{11}^{m} - C_{12}^{m}\right)\left({\varepsilon_{22}^{p}}^{(12)} - {\varepsilon_{22}^{p}}^{(22)}\right) + Q_2\left[\left(C_{11}^{m} - C_{12}^{m}\right){\varepsilon_{22}^{p}}^{(21)} - \left(C_{11}^{f} - C_{12}^{f}\right){\varepsilon_{22}^{p}}^{(11)}\right] \\ & + Q_3\left[\left(C_{11}^{m} - C_{12}^{m}\right){\varepsilon_{33}^{p}}^{(12)} - \left(C_{11}^{f} - C_{12}^{f}\right){\varepsilon_{33}^{p}}^{(11)}\right] + Q_4\left(C_{11}^{m} - C_{12}^{m}\right)\left({\varepsilon_{33}^{p}}^{(21)} - {\varepsilon_{33}^{p}}^{(22)}\right) \\ & + v_{11}\left(C_{11}^{f} - C_{12}^{f}\right){\varepsilon_{11}^{p}}^{(11)} + \left(C_{11}^{m} - C_{12}^{m}\right)\left(v_{12}{\varepsilon_{11}^{p}}^{(12)} + v_{21}{\varepsilon_{11}^{p}}^{(21)} + v_{22}{\varepsilon_{11}^{p}}^{(22)}\right)\end{aligned}$$

$$\begin{aligned}VH_{22} = {} & Q_1'\left(C_{11}^{m} - C_{12}^{m}\right)\left({\varepsilon_{22}^{p}}^{(12)} - {\varepsilon_{22}^{p}}^{(22)}\right) + Q_2'\left[\left(C_{11}^{m} - C_{12}^{m}\right){\varepsilon_{22}^{p}}^{(21)} - \left(C_{11}^{f} - C_{12}^{f}\right){\varepsilon_{22}^{p}}^{(11)}\right] \\ & + Q_3'\left[\left(C_{11}^{m} - C_{12}^{m}\right){\varepsilon_{33}^{p}}^{(12)} - \left(C_{11}^{f} - C_{12}^{f}\right){\varepsilon_{33}^{p}}^{(11)}\right] + Q_4'\left(C_{11}^{m} - C_{12}^{m}\right)\left({\varepsilon_{33}^{p}}^{(21)} - {\varepsilon_{33}^{p}}^{(22)}\right) \\ & + v_{11}\left(C_{11}^{f} - C_{12}^{f}\right){\varepsilon_{22}^{p}}^{(11)} + \left(C_{11}^{m} - C_{12}^{m}\right)\left(v_{12}{\varepsilon_{22}^{p}}^{(12)} + v_{21}{\varepsilon_{22}^{p}}^{(21)} + v_{22}{\varepsilon_{22}^{p}}^{(22)}\right)\end{aligned}$$

$$\begin{aligned}VH_{33} = {} & Q_1''\left(C_{11}^{m} - C_{12}^{m}\right)\left({\varepsilon_{22}^{p}}^{(12)} - {\varepsilon_{22}^{p}}^{(22)}\right) + Q_2''\left[\left(C_{11}^{m} - C_{12}^{m}\right){\varepsilon_{22}^{p}}^{(21)} - \left(C_{11}^{f} - C_{12}^{f}\right){\varepsilon_{22}^{p}}^{(11)}\right] \\ & + Q_3''\left[\left(C_{11}^{m} - C_{12}^{m}\right){\varepsilon_{33}^{p}}^{(12)} - \left(C_{11}^{f} - C_{12}^{f}\right){\varepsilon_{33}^{p}}^{(11)}\right] + Q_4''\left(C_{11}^{m} - C_{12}^{m}\right)\left({\varepsilon_{33}^{p}}^{(21)} - {\varepsilon_{33}^{p}}^{(22)}\right) \\ & + v_{11}\left(C_{11}^{f} - C_{12}^{f}\right){\varepsilon_{33}^{p}}^{(11)} + \left(C_{11}^{m} - C_{12}^{m}\right)\left(v_{12}{\varepsilon_{33}^{p}}^{(12)} + v_{21}{\varepsilon_{33}^{p}}^{(21)} + v_{22}{\varepsilon_{33}^{p}}^{(22)}\right)\end{aligned}$$

$$VH_{12} = 2\left[\nu_{11} C_{44}^{f} \varepsilon_{12}^{p\,(11)} + C_{44}^{m}\left(\nu_{12}\varepsilon_{12}^{p\,(12)} + \nu_{21}\varepsilon_{12}^{p\,(21)} + \nu_{22}\varepsilon_{12}^{p\,(22)} \right)\right] + \frac{2}{h} C_{44}^{m}\left(\nu_{22}h_1 - \nu_{12}h_2\right)\left(\varepsilon_{12}^{p\,(12)} - \varepsilon_{12}^{p\,(22)}\right)$$
$$- \frac{2}{h_1 C_{44}^{m} + h_2 C_{44}^{f}}\left(\nu_{11}h_2 C_{44}^{f} - \nu_{21}h_1 C_{44}^{m}\right)\left(C_{44}^{f}\varepsilon_{12}^{p\,(11)} - C_{44}^{m}\varepsilon_{12}^{p\,(21)}\right)$$

$$VH_{13} = 2\left[\nu_{11} C_{55}^{f} \varepsilon_{13}^{p\,(11)} + C_{55}^{m}\left(\nu_{21}\varepsilon_{13}^{p\,(21)} + \nu_{12}\varepsilon_{13}^{p\,(12)} + \nu_{22}\varepsilon_{13}^{p\,(22)} \right)\right] + \frac{2}{l} C_{55}^{m}\left(\nu_{22}l_1 - \nu_{21}l_2\right)\left(\varepsilon_{13}^{p\,(21)} - \varepsilon_{13}^{p\,(22)}\right)$$
$$- \frac{2}{l_1 C_{55}^{m} + l_2 C_{55}^{f}}\left(\nu_{11}l_2 C_{55}^{f} - \nu_{12}l_1 C_{55}^{m}\right)\left(C_{55}^{f}\varepsilon_{13}^{p\,(11)} - C_{55}^{m}\varepsilon_{13}^{p\,(12)}\right)$$

$$VH_{23} = \frac{2C_{66}^{f}\, C_{66}^{m}\left(\nu_{11}\varepsilon_{23}^{p\,(11)} + \nu_{12}\varepsilon_{23}^{p\,(12)} + \nu_{21}\varepsilon_{23}^{p\,(21)} + \nu_{22}\varepsilon_{23}^{p\,(22)}\right)}{h_1\, l_1\, C_{66}^{m} + \left(h_1\, l_2 + h_2\, l_1 + h_2\, l_2\right) C_{66}^{f}}$$

$$Q_i = \nu_{11} C_{12}^{f}\left(T_i + T_{i+8}\right) - \nu_{12} C_{12}^{m}\left(\frac{h_2}{h_1} T_{i+4} + \frac{l_1}{l_2} T_{i+8}\right) - \nu_{21} C_{12}^{m}\left(\frac{h_1}{h_2} T_i + \frac{l_2}{l_1} T_{i+12}\right)$$
$$+ \nu_{22} C_{12}^{m}\left(T_{i+4} + T_{i+12}\right) \qquad i = 1,2,3,4$$

$$Q_i' = \nu_{11}\left(C_{22}^{f} T_i + C_{23}^{f} T_{i+8}\right) - \nu_{12}\left(C_{22}^{m}\frac{h_2}{h_1} T_{i+4} + C_{23}^{m}\frac{l_1}{l_2} T_{i+8}\right) - \nu_{21}\left(C_{22}^{m}\frac{h_1}{h_2} T_i + C_{23}^{m}\frac{l_2}{l_1} T_{i+12}\right)$$
$$+ \nu_{22}\left(C_{22}^{m} T_{i+4} + C_{23}^{m} T_{i+12}\right) \qquad i = 1,2,3,4$$

$$Q_i'' = \nu_{11}\left(C_{23}^{f} T_i + C_{22}^{f} T_{i+8}\right) - \nu_{12}\left(C_{23}^{m}\frac{h_2}{h_1} T_{i+4} + C_{22}^{m}\frac{l_1}{l_2} T_{i+8}\right) - \nu_{21}\left(C_{23}^{m}\frac{h_1}{h_2} T_i + C_{22}^{m}\frac{l_2}{l_1} T_{i+12}\right)$$
$$+ \nu_{22}\left(C_{23}^{m} T_{i+4} + C_{22}^{m} T_{i+12}\right) \qquad i = 1,2,3,4$$

$$\begin{array}{ll}
DT_1 = -A_5A_8A_{12} - A_6A_9A_{11} & DT_2 = A_2A_8A_{12} + A_3A_9A_{11} - A_1A_9A_{12} \\
DT_3 = A_1A_5A_{12} + A_2A_6A_{11} - A_3A_5A_{11} & DT_4 = A_1A_6A_9 + A_3A_5A_8 - A_2A_6A_8 \\
DT_5 = A_6A_9A_{10} + A_5A_7A_{12} - A_4A_9A_{12} & DT_6 = -A_2A_7A_{12} - A_3A_9A_{10} \\
DT_7 = A_3A_5A_{10} + A_2A_4A_{12} - A_2A_6A_{10} & DT_8 = A_2A_6A_7 + A_3A_4A_9 - A_3A_5A_7 \\
DT_9 = A_4A_8A_{12} + A_6A_7A_{11} - A_6A_8A_{10} & DT_{10} = A_1A_7A_{12} + A_3A_8A_{10} - A_3A_7A_{11} \\
DT_{11} = A_3A_4A_{11} + A_1A_6A_{10} - A_1A_4A_{12} & DT_{12} = -A_1A_6A_7 - A_3A_4A_8 \\
DT_{13} = A_4A_9A_{11} + A_5A_8A_{10} - A_5A_7A_{11} & DT_{14} = A_1A_9A_{10} + A_2A_7A_{11} - A_2A_8A_{10} \\
DT_{15} = -A_1A_5A_{10} - A_2A_4A_{11} & DT_{16} = A_1A_5A_7 - A_1A_4A_9 + A_2A_4A_8
\end{array}$$

$$D = \begin{vmatrix} 0 & A_1 & A_2 & A_3 \\ A_4 & 0 & A_5 & A_6 \\ A_7 & A_8 & A_9 & 0 \\ A_{10} & A_{11} & 0 & A_{12} \end{vmatrix}$$

$$A_1 = C_{22}^m\left(1+\frac{h_2}{h_1}\right) \qquad A_2 = C_{23}^m\frac{l_1}{l_2} \qquad A_3 = C_{23}^m$$

$$A_4 = C_{22}^f + C_{22}^m\frac{h_1}{h_2} \qquad A_5 = C_{23}^f \qquad A_6 = C_{23}^m\frac{l_2}{l_1}$$

$$A_7 = C_{23}^f \qquad A_8 = C_{23}^m\frac{h_2}{h_1} \qquad A_9 = C_{22}^f + C_{22}^m\frac{l_1}{l_2}$$

$$A_{10} = C_{23}^m\frac{h_1}{h_2} \qquad A_{11} = C_{23}^m \qquad A_{12} = C_{22}^m\left(1+\frac{l_2}{l_1}\right)$$

where,

$$l = l_1 + l_2 \qquad h = h_1 + h_2 \qquad v_{\beta\gamma} = l_\beta h_\gamma \qquad V = l h$$

$$\alpha^* = \alpha^m + \left[\alpha^f - \alpha^m\right]\left[S^f - S^m\right]^{-1}\left[S^* - S^m\right]$$

where α^* is the effective CTE vector, α^m is the matrix CTE vector, α^f is the fiber CTE vector, S^* is the effective compliance matrix, S^m is the matrix compliance matrix, and S^f is the fiber compliance matrix.

REPORT DOCUMENTATION PAGE

Form Approved
OMB No. 0704-0188

1. AGENCY USE ONLY *(Leave blank)*

2. REPORT DATE
January 1997

3. REPORT TYPE AND DATES COVERED
Final Contractor Report

4. TITLE AND SUBTITLE
Experimental Characterization and Micromechanical Modeling of Woven Carbon/Copper Composites

5. FUNDING NUMBERS
WU–523–61–23
G–NAG3–1319

6. AUTHOR(S)
Brett A. Bednarcyk, Christopher C. Pauly, and Marek-Jerzy Pindera

7. PERFORMING ORGANIZATION NAME(S) AND ADDRESS(ES)
University of Virginia
Charlottesville, Virginia

8. PERFORMING ORGANIZATION REPORT NUMBER
E–10623

9. SPONSORING/MONITORING AGENCY NAME(S) AND ADDRESS(ES)
National Aeronautics and Space Administration
Lewis Research Center
Cleveland, Ohio 44135–3191

10. SPONSORING/MONITORING AGENCY REPORT NUMBER
NASA CR–202318

11. SUPPLEMENTARY NOTES
Project Manager, M.V. Nathal, Materials Division, NASA Lewis Research Center, organization code 5120, (216) 433–9516.

12a. DISTRIBUTION/AVAILABILITY STATEMENT
Unclassified - Unlimited
Subject Category 26

This publication is available from the NASA Center for AeroSpace Information, (301) 621–0390.

12b. DISTRIBUTION CODE

13. ABSTRACT ***(Maximum 200 words)***

The results of an extensive experimental characterization and a preliminary analytical modeling effort for the elastoplastic mechanical behavior of 8–harness satin weave carbon/copper (C/Cu) composites are presented. Previous experimental and modeling investigations of woven composites are discussed, as is the evolution of, and motivation for, the continuing research on C/Cu composites. Experimental results of monotonic and cyclic tension, compression, and Iosipescu shear tests, and combined tension-compression tests, are presented. With regard to the test results, emphasis is placed on the effect of strain gauge size and placement, the effect of alloying the copper matrix to improve fiber-matrix bonding, yield surface characterization, and failure mechanisms. The analytical methodology used in this investigation consists of an extension of the three-dimensional generalized method of cells (GMC–3D) micromechanics model, developed by Aboudi (1994), to include inhomogeneity and plasticity effects on the subcell level. The extension of the model allows prediction of the elastoplastic mechanical response of woven composites, as represented by a true repeating unit cell for the woven composite. The model is used to examine the effects of refining the representative geometry of the composite, altering the composite overall fiber volume fraction, changing the size and placement of the strain gauge with respect to the composite's reinforcement weave, and including porosity within the infiltrated fiber yarns on the in-plane elastoplastic tensile, compressive, and shear response of 8-harness satin C/Cu. The model predictions are also compared with the appropriate monotonic experimental results.

14. SUBJECT TERMS
Composite materials; Metal matrix composites; Woven fiber composites; Mechanical properties; Micromechanics

15. NUMBER OF PAGES
109

16. PRICE CODE
A06

17. SECURITY CLASSIFICATION OF REPORT
Unclassified

18. SECURITY CLASSIFICATION OF THIS PAGE
Unclassified

19. SECURITY CLASSIFICATION OF ABSTRACT
Unclassified

20. LIMITATION OF ABSTRACT